OPTICAL PROPERTIES OF RARE-EARTH DOPED FLUOROZIRCONATE GLASS-CERAMICS FOR X-RAY DETECTOR APPLICATIONS

A Thesis Submitted to the
College of Graduate Studies and Research
in Partial Fulfillment of the Requirements
for the degree of Master of Science
in the Department of Electrical and Computer Engineering
University of Saskatchewan
Saskatoon

By
Go Okada

Permission to Use

In presenting this thesis in partial fulfillment of the requirements for a Postgraduate degree from the University of Saskatchewan, I agree that the Libraries of this University may make it freely available for inspection. I further agree that permission for copying of this thesis in any manner, in whole or in part, for scholarly purposes may be granted by the professor or professors who supervised my thesis work or, in their absence, by the Head of the Department or the Dean of the College in which my thesis work was done. It is understood that any copying or publication or use of this thesis or parts thereof for financial gain shall not be allowed without my written permission. It is also understood that due recognition shall be given to me and to the University of Saskatchewan in any scholarly use which may be made of any material in my thesis.

Requests for permission to copy or to make other use of material in this thesis in whole or part should be addressed to:

Head of the Department of Electrical and Computer Engineering
University of Saskatchewan
Saskatoon, Saskatchewan
Canada
S7N 5A9

ABSTRACT

For high-resolution X-ray imaging scintillator applications, we have prepared and optically characterized divalent samarium doped fluorochlorozirconate (FCZ:Sm^{2+}) glasses and glass-ceramics. Sm^{2+} doped FCZ glasses were obtained by adding a reducing agent, $NaBH_4$ into the initial melt to convert some of the Sm^{3+} to Sm^{2+}. However, the Sm^{2+} concentration at most was estimated to be only ~ 0.003 %. The as-prepared glass samples were further heat treated to obtain glass-ceramics; the nucleation and growth of $BaCl_2$ nanocrystals were confirmed by powdered X-ray diffraction (XRD) experiments. Depending on the heat treatment conditions (temperature and time), the average nanocrystal size varies from 8 to 170 nm, and the sample contains $BaCl_2$ nanocrystals with the orthorhombic and/or hexagonal structure. The optical absorption spectra for our glass-ceramic samples suggested the substitution of Sm^{2+} ions into the $BaCl_2$ lattice site. The FCZ:Sm^{2+} glass-ceramics samples showed strong fluorescence in the red region of spectrum (~ 8 times that of an as-prepared glass), and the transparency can be very high (transmittance $>$ 80 % for samples with thickness ~ 0.5 mm) and can be equivalent to that of an as-prepared glass . These two results promise potential as a high-resolution X-ray scintillator due to the emission wavelength range and high transparency. Extensive studies of photoluminescence (PL) spectra at low temperatures (12 – 200 K) for FCZ:Sm^{2+} glass-ceramics suggested useful indicators of the crystal structure and average size of embedded $BaCl_2$ nanocrystals. A detailed analysis of the optical spectra has lead to the identification of the origin of the emission peaks and the location of Sm ions at specific crystallographic sites. X-ray induced luminescence (XL) studies have suggested a strong dependence of the fluorescence intensity on the concentration of Sm^{2+} ions. In addition, for more efficient fluorescence, a sample should be heat treated in a hydrogen containing atmosphere (e.g. H_2 + Ar gas), and the heat treatment conditions should be such that the nanocrystals grow in the hexagonal structure.

ACKNOWLEDGEMENTS

I extend my sincerest gratitude to my supervisor, Dr. S. O. Kasap for his leadership, patience, and encouragement throughout the course of this research as well as his invaluable assistance for finalizing this thesis. I would also like to thank: my mentor Dr. K. Koughia for his guidance, support, and assistance throughout the experimental works, Dr. G. Belev for his help in experimental works and discussions, Dr. A. Edgar and Dr. C. Varoy for preparing samples and X-ray diffraction measurements, and the University of Saskatchewan for its financial support. Finally, but not the least, I would like to thank my family, friends, and colleagues for their support, encouragement, and patience.

CONTENTS

List of Tables

List of Figures

LIST OF ABBREVIATIONS

AMA	Active Matrix Array
Ar	Argon
a-Se	Amorphous Selenium
a-Si	Amorphous Silicon
Ba	Barium
$BaBr_2$	Barium Bromide
$BaCl_2$	Barium Chloride
$BaFBr_2$	Barium Fluorobromide
Br	Bromine
CCD	Charge-Coupled Device
Cl	Chlorine
CMOS	Complementary Metal-Oxide Semiconductor
CsI	Caesium Iodide
CT	Computed Tommography
Eu	Europium
F	Fluorine
FBZ	Fluorobromoziroconate
FCZ	Fluorochlorozirconate
FWHM	Full Width at Half Maximum
FZ	Fluorozirconate
Gd_2O_2S, GOS	Gadolinium Oxysulfide
H_2	Hydrogen
Lu_2O_3	Lutetium Oxide
$NaBH_4$	Sodium Borohydride
NaI	Sodium Iodide
NIR	Near Infrared
PL	Photoluminescence
PMT	Photomultiplier Tube
PSL	Photostimulated Luminescence
RA	Reducing Agent
SEM	Scanning Electron Microscope
Sm	Samarium
$SmCl_2$	Samarium Dichloride
SmF_2	Samarium Difluoride
TFT	Thin-Film Transistor
UV	Ultraviolet
XL	X-ray Luminescence
XRD	X-Ray Diffraction
YAG	Yttrium Aluminium Garnet

CHAPTER 1

INTRODUCTION

Since the discovery of X-rays by Wilhelm Conrad Röntgen in 1895, due to its unique properties, the X-rays have found their applications over a wide range of areas including medicine, astronomy, security and industry. Since the use of X-rays always requires their sensing by users, together with these advances of X-ray applications, the detection or measurement technologies have also been intensively studied. Today, X-ray detector technologies have advanced to the point that the image can be acquired in a digital form and the image resolution is sufficiently high to be used in mammography. These advances have not been possible without good understanding of properties of the materials used in the detectors. In addition, the study of detector materials may have application beyond just X-ray detection. Meanwhile, there is no perfect detector meeting all the requirements, and the requirements change with the appearance of new technologies. Therefore, further advances are always needed, and hence we are always searching for new materials.

The objective of this research is the preparation and experimental characterization of the optical properties of divalent samarium doped fluorochlorozirconate (FCZ:Sm^{2+}) glass-ceramics for high-resolution X-ray imaging applications. In such applications, a scintillator converts X-rays to visible light in order that the image can be recorded by conventional imaging sensors such as a CCD, CMOS, and photodiode arrays etc.

Rare-earth doped FCZ glass-ceramics are a new class of transparent glass-ceramics. Transparent X-ray scintillator would have potential to give high spatial resolution.

Earlier studies have shown that upon heat treatment, barium chloride ($BaCl_2$) nanocrystals uniformly grow in FCZ glasses. The crystallographic structure is either the orthorhombic or hexagonal, and the size varies depending on the heat treatment conditions — time and temperature. In other words, the glass-ceramic properties can be controlled by an appropriate selection of the heat treatment conditions.

Doping of FCZ glasses with Sm^{2+} ions is not so straightforward since it requires either $SmCl_2$ or SmF_2, neither of which is commercially available. Therefore, we, first, attempted to dope the glass samples with Sm^{3+} ions and then tried to reduce the valency state to the '2+' by adding a few molar fractions of $NaBH_4$ in the glass melt.

We have chosen divalent samarium (Sm^{2+}) as a photoactivator for two reasons. First, in many materials, Sm^{2+} exhibits a strong luminescence in the red range of spectrum to which today's silicon-based detectors are sensitive. As far as we are aware, no studies for FCZ:Sm^{2+} glass-ceramics have been reported. Second, spectroscopic study of Sm^{2+} would be a useful probe of the local environment such as the $BaCl_2$ crystal structure, nanocrystal size and the ion substitution in the $BaCl_2$ nanocrystals. It is instructive to mention here that since the radii of divalent samarium and barium ions are similar, the Sm^{2+} ions are expected to substitute for the barium ions in $BaCl_2$ crystallites.

X-ray induced fluorescence properties would be of our greatest interest since an efficient, or sensitive, scintillator exhibits strong X-ray luminescence. Therefore, the fluorescence intensity was studied in association with the embedded $BaCl_2$ crystallites structure and size as well as the annealing atmosphere.

The following chapter will review the literature for the state-of-art X-ray radiography detector technologies as well as rare-earth doped fluorozirconate glass-ceramics as promising materials for X-ray imaging scintillator applications.

Chapter 3 provides experimental details carried out in this project. The preparation of glass samples and X-ray crystallographic investigation by powder X-ray diffraction (XRD) analyses have been carried out by our collaborators, Andy Edgar and Chris Varoy at the School of Chemical and Physical Sciences, Victoria University of Wellington, New Zealand, and those are described in Section 3.1 and 3.3, respectively. As-prepared glass samples were further annealed to induce the nucleation of nanocrystals, resulting in glass-ceramics, which is described in Section 3.2. The spectroscopic techniques used, including optical absorption spectroscopy, photoluminescence spectroscopy, and X-ray induced luminescence spectroscopy at room temperature, are explained from Section 3.5 to 3.7. Steady-state photoluminescence experiments using a cryostat system were also carried out to obtain the photoluminescence spectrum as a function of temperature.

Experimental results are described and discussed in Chapter 4. Transparent as-prepared glasses with different fractions of reducing agent added are explained in Section 4.1. The successful valency reduction of the samarium ion is shown by optical absorption arising from Sm^{2+}. In Section 4.2, effects of heat treatment are discussed. Upon heat treatment, divalent samarium ions are activated to exhibit fluorescence, and there is a dramatic improvement in the X-ray luminescence intensity. XRD studies showed the nucleation and growth of $BaCl_2$ nanocrystals in the glass-ceramics. In Section 4.3, extensively studied photoluminescence spectra as a function of temperature suggest new techniques as useful indicators of the crystal structural phase of $BaCl_2$ nanocrystals and their average size. Also, luminescence from Sm^{2+} at specific crystallographic sites is identified. In addition, we examine the dependence of the X-ray induced luminescence intensity on the the fraction of reducing agent added, annealing atmosphere, and average size and crystal structure of the embedded $BaCl_2$ nanocrystals is discussed in Section 4.4.

Last, this thesis is concluded with summaries of the research results, conclusions, and recommendations for possible future works, which are all in Chapter 5.

Chapter 2

Background and Review

Since the discovery of X-rays by Wilhelm Conrad Röntgen in 1895, for which he received the first Nobel Prize in Physics in 1901, these X-rays have been widely used in a number of areas including medicine, astronomy, security and industry, due to their unique properties. Probably, one of the best known applications of X-rays would be in medical imaging or radiography. In the latter process, we are able to visualize the interior of the human body by passing X-rays through it. This technique has been used to diagnose illnesses of human or animals immediately after the discovery of X-rays. Further, this technique is also used for other purposes; for example, inspection of a travel baggage and a cargo container, as well as industrial products.

Since X-rays are invisible to the human eye, its applications often require the detection of X-rays. Especially in X-ray imaging, the X-ray intensity pattern must be detected in two dimensions. Traditionally, photographic films have been used to obtain the X-ray intensity patterns as an image as in normal photography. However, a photographic film itself has a very low sensitivity to X-rays and, therefore, requires a large amount of radiation dose to obtain an image with an acceptable quality in use. In order to improve the sensitivity, photographic screens have been used with a combination of *phosphor* screens, in which the phosphor screen converts X-ray to light to which the photographic screen is sensitive. This type of a phosphor screen is also called an *intensifying screen.* This traditional technique of X-ray imaging with a photographic screen is often referred as an 'analog' method. Today, X-ray images can be digitally obtained, and this digital imaging method (or digital radiography) has been taking over the analog techniques for its distinct advantages. It should be pointed out that phosphor screens play an important role in digital radiography.

This chapter will review digital radiography as a state-of-art radiography technique especially focusing on detection techniques and detectors. Next, literatures of promising phosphor materials, rare-earth doped fluorozirconate glasses and glass-ceramics, will be reviewed.

2.1 Review of Digital Radiography

The creation of an X-ray image may conceptually be divided into three separate stages [1]. The first stage is the interaction of the X-ray with a suitable detection medium to generate a measurable response. The second stage is the storage of this response with a recording device. The third stage is the measurement of this stored response. The development of X-ray detectors has been stimulated by radiography applications since radiography requires high performance for the detector, such as high spatial resolution and sensitivity.

2.1.1 Digital Radiography

One of the most successful applications of X-ray imaging is medical diagnosis. With X-ray radiation, we can image the interiors of objects. X-rays have a unique property that the X-ray absorption strongly depends on media as illustrated in Figure 2.1. X-ray photons are strongly absorbed in dense media such as bones, meanwhile they pass through without or with less attenuation in less dense media such as blood and tissues. Figure 2.2 shows a schematic diagram of an X-ray imaging system. X-ray radiation is generated by an X-ray tube, and X-ray photons are guided towards a target, or patient, through a collimator. Some of the incident X-ray photons are absorbed in dense media of the human body, but some media allow them to pene-

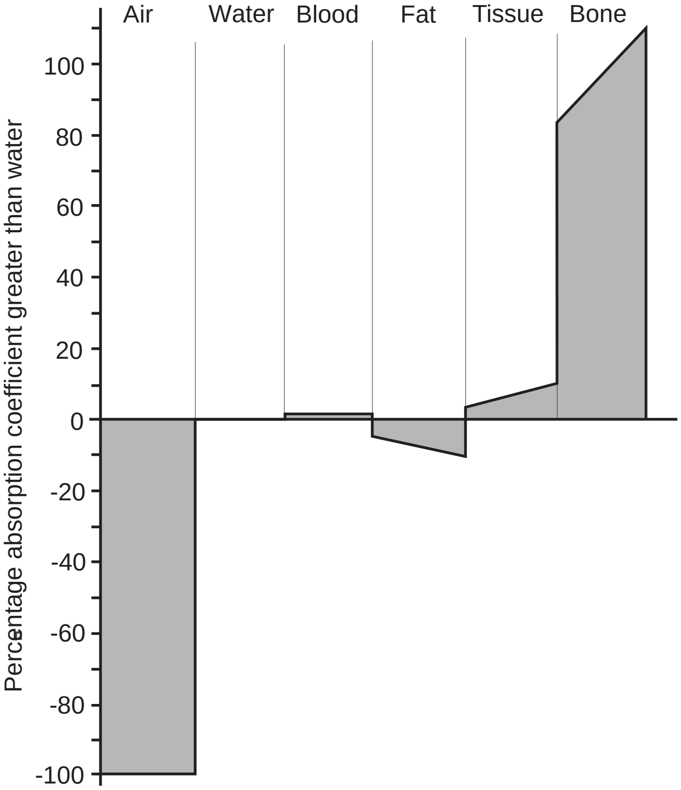

Figure 2.1: Variation of the X-ray absorption coefficient for various components of the human body. The data have been normalized to that of water. Reproduced from [2].

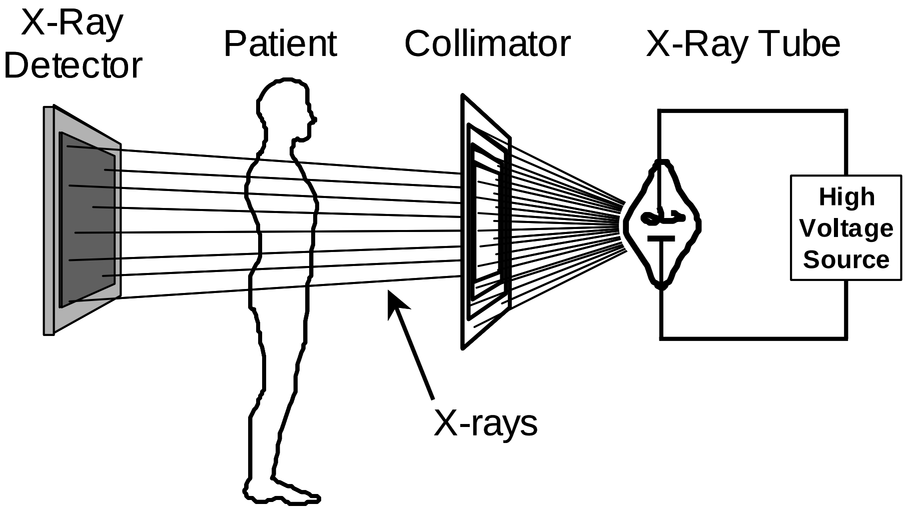

Figure 2.2: A schematic illustration of X-ray imaging setup. From [3].

trate further. As a result, the transmitted X-ray photons create an image pattern of the inner body. The transmitted X-ray photons are collected by an X-ray detector, which will be reviewed in the next section.

Traditionally, immediately after the discovery of X-rays, photographic films had been used to record X-ray images for nearly 100 years. X-ray imaging based on photographic films includes some notable disadvantages, for example a time-consuming chemical development and a requirement of large storage cabinets in a hospital. In recent years, digital X-ray imaging has been introduced to replace the conventional film-based technique due to its distinct advantages. Unlike the photographic film, digital X-ray detectors convert X-ray photons into electrical signals, so this conversion into electrical signals enables us to handle X-ray images electronically. Therefore, together with combinations of other digital technologies, digital radiography has many distinct advantages over traditional analog techniques such as the following [4, 5]:

1. Image enhancement is possible with digital signal processing.
2. Digital X-ray detector is solid state, robust as well as reusable.
3. A large film storage cabinet can be replaced by a digital storage device such as a hard disk drive.
4. Combined with network technologies, instant archiving and access of images can be realized (Picture Archive and Communication Systems; PACS).

Today, the film-based analog X-ray imaging has been displaced by the digital technologies for the convenience and potential of a number of important functionalities.

2.1.2 Digital Radiography Techniques

Digital radiography uses imaging sensors that converts X-ray photons to electrical signals. In general, digital X-ray detectors may be divided into two categories in terms of the method used to convert X-ray photons to an electrical signal: *direct conversion* and *indirect conversion*. For direct conversion detectors, X-ray photons are converted 'directly' into an electrical signal, or more accurately electronic charges; meanwhile, an indirect X-ray detector converts X-ray photons to light, and then the light is converted to an electrical signal by using conventional imaging sensors. This section briefly reviews both the techniques.

Direct conversion X-ray detectors have become available in the late 1990s [6]. Details of a review for this type of X-ray detectors are found elsewhere [6, 7, 8]. Typically, a detector consists of millions of aligned image elements, called pixels, and each pixel is responsible for collecting X-ray intensity information at each local area. Figure 2.3 illustrates a schematic diagram of a part of a direct conversion X-ray detector. An X-ray photoconductor (typically a-Se) is coated over a thin-film transistor active matrix array (TFT-AMA). Incoming X-ray photons are absorbed by the photoconductor layer, and then electronic charges, or electron-hole pairs, are generated upon ionizing interactions of X-rays in the photoconductor. An electrode is deposited on top of the photoconductor, and an applied bias on this electrode creates an electric field across the photoconductor layer, which drifts the charges toward the pixel electrode; eventually, the charges are stored in the storage capacitor at the pixel. The stored charges are then read out as the amount of incident radiation for each pixel. Last, a single image is reconstructed by gathering all the collected information from all the arrays of pixels.

For its simple detector structure and architecture, it is believed that the direct conversion method is the best detector for resolution. With a TFT-AMA, the readout process is fast ($<$ 1 sec). The image detector can be produced in a size equivalent to that of a conventional cassette type film-based detector. It can, therefore, simply replace the cassette-film, and the rest of the X-ray imaging conventional systems (the X-ray tube etc.) remains the same. Moreover, very efficient conversion of X-rays to electrical signals is possible by applying an electric field across the photoconductor

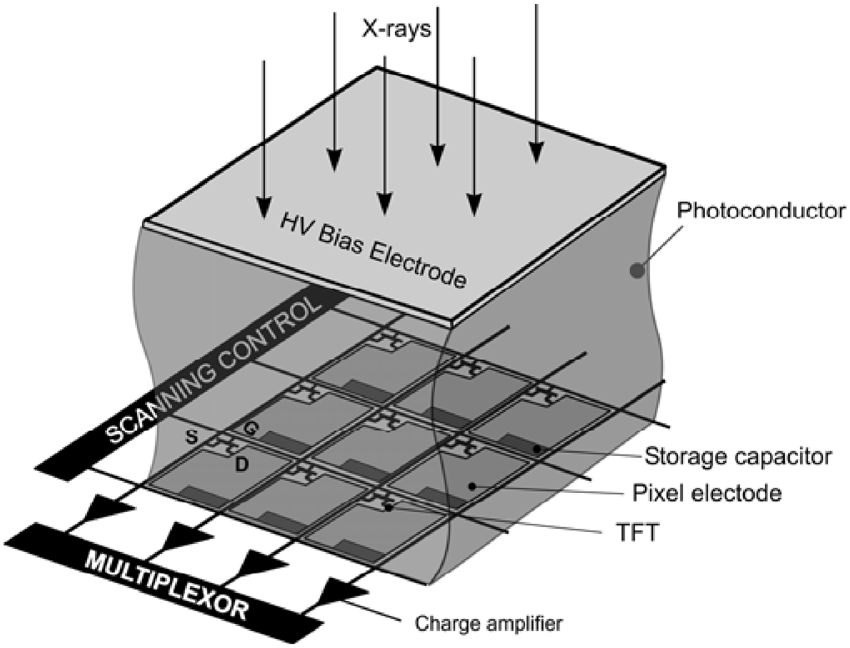

Figure 2.3: A schematic illustration of direct conversion X-ray flat-panel detector. From [9].

layer. This technique ensures essentially 100 % fill factor (a ratio of collected charges to generated charges). However, to ensure this high fill factor, very high voltage must be applied (several kilovolts) [8]. Further, the coverage area of this type of flatpanel detector is strongly dependent on the TFT array fabrication technology. As the detector size is enlarged, the pixel size has to be maintained sufficiently small to ensure a high image resolution.

Meanwhile, indirect conversion techniques include mainly two different technologies. One utilizes a *storage phosphor*, also called an imaging plate, to temporally store the X-ray pattern information. This technology was first established by FUJIFILM [10, 11] and became commercially available in the early 1980s. The latter technology, called computed radiography, is one of the most successful medical imaging methods.

Typical X-ray imaging processes with a storage phosphor are as follows. As incident X-ray photons interact with imaging plate media, a local spot is ionized,

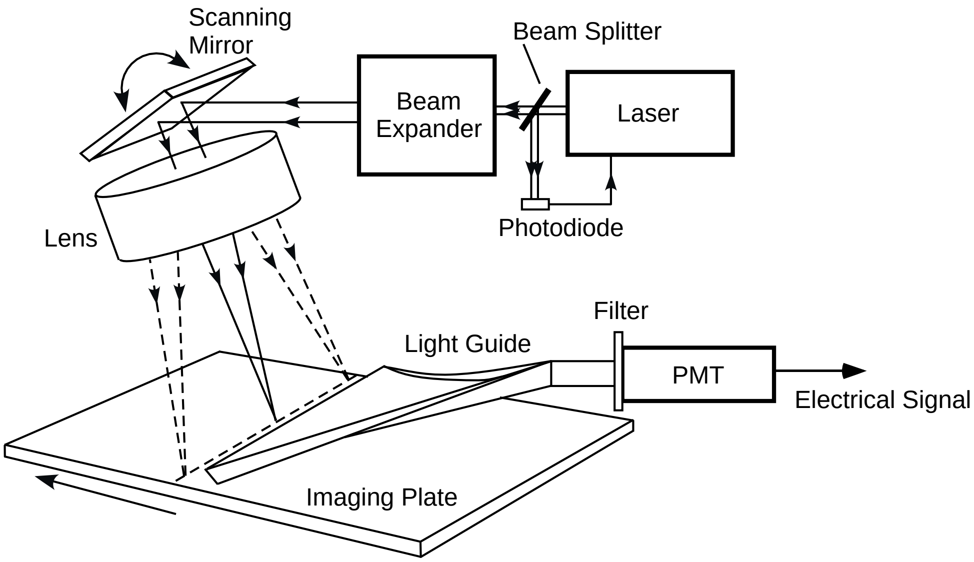

Figure 2.4: A schematic illustration of a flying spot readout scanner. Reproduced from [12].

and electron-hole pairs are generated to a degree depending on the number of incident X-ray photons, or the X-ray intensity. Some electron-hole pairs recombine immediately and emit optical photons, yet some other charges are trapped at local sites, called photoactive centres. Upon photostimulation, the trapped charges are then photoexcited and induced to recombine and, as a result, light is emitted. This process is called photostimulated luminescence (PSL). The details of the PSL mechanism are discussed elsewhere [13, 14]. Figure 2.4 illustrates a schematic diagram of a readout system for an imaging plate. A stimulation light beam by a laser is finely focused, so only an infinitesimal area is stimulated. The resulting PSL at each point is guided toward a photodetector to be measured, typically a photomultiplier tube (PMT), which converts light to an electrical signal. This readout process is done on a point-by-point basis. It should be instructive to mention here that the stimulation light beam and the emission light must have different wavelengths, so they can be distinguished at the detector. All the information is assembled, and then a single image is constructed. The stored information on the imaging plate can be easily erased under room light exposure, and imaging plates are reusable.

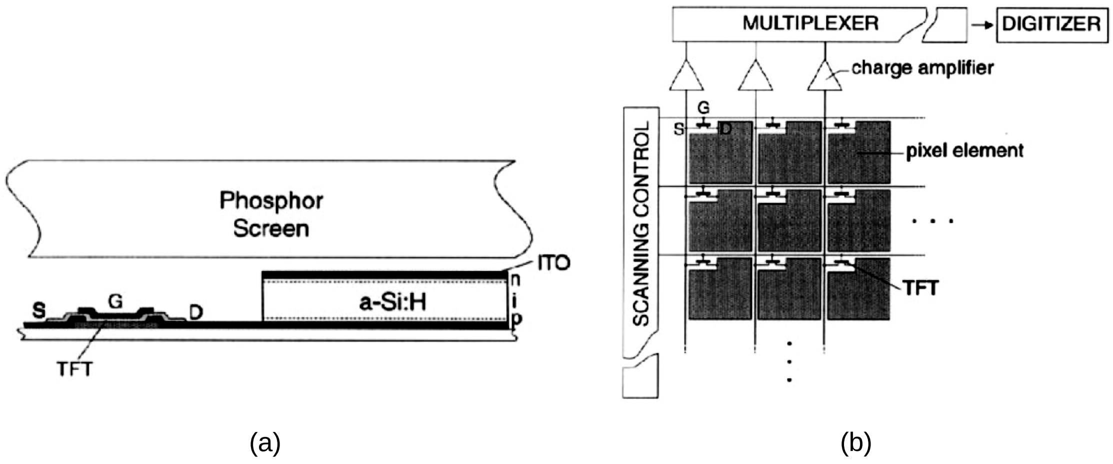

Figure 2.5: A schematic illustration of an indirect X-ray imaging detector. A scintillator screen is placed on top of an array of a-Si photodetectors. (a) A cross-section of a single pixel. (b) A part of an active matrix array (AMA) of thin film transistors (TFTs) for readout processes. From [17].

Since this image acquisition technique enables us to obtain a very high resolution X-ray image, compared with that from traditional film-based methods, it has been a commonly used technique for mammography applications, in which it is desirable to resolve a structural detail of a tumor as small as 50 μm [15]. However, it takes a relatively long time (for example, $\sim$ 30 sec to read out 2000 $\times$ 2000 pixels of an imaging plate with a commercial reader [16]). Also, this whole system requires a large space for operations. In addition, there are causes that reduce the image quality, due to the imaging plate properties, which will be discussed in the next section.

Instead of using a storage phosphor, the other type of indirect X-ray detectors use a phosphor to convert X-rays to light so that an X-ray image can be acquired by a conventional photodetector array, such as an imaging sensor (CCD, CMOS, a-Si photodetector array etc.). For this purpose, the phosphor is often called a *scintillator.* A process of X-ray imaging with a scintillator is much simpler than that of a storage phosphor. Figure 2.5 (a) shows a schematic illustration of a cross-section of an X-ray image detector using a scintillator screen. Incoming X-ray photons interact with a scintillator medium, which is then ionized. The ionized charges (electron-hole pairs) then immediately recombine, and this recombination gives off light photons.

Combined with a conventional imaging sensor, the emitted light is detected at each local position (pixel). Eventually, the collected light intensity pattern information is read out; this process depends on the imaging sensor used.

The above method shares various advantages with the direct conversion detector. In contrast with a point-by-point readout with a storage phosphor, the image data is readout as quickly as the direct conversion method (< 1 s). Since a thin scintillator layer does not essentially affect the detector thickness, a combination with a photodetector array enables us to keep the detector thickness sufficiently thin to be replaceable with the traditional cassette type film-based detector. However, when coupled with a-Si TFT-AMA detector as illustrated in Figure 2.5 (b), the detector size is essentially dependent on the TFT-AMA fabrication as in direct conversion flat-panel detectors. One way to achieve a large-area coverage is to tile together inexpensive CMOS or CCD sensors. When a single imaging sensor is smaller than that of required field coverage size, it is necessary to demagnify an image from a scintillator. This demagnification is often done with a lens or a fibre optic taper, but the demagnification process causes a reduction of the image resolution [12]. There are other possible causes that reduce the resolution due to properties of the scintillator, which will be discussed in the next section.

2.1.3 Common Phosphor Materials for Digital Radiography

As described in the previous section, phosphors play very important roles in digital radiography for both as an imaging plate and scintillator. Therefore, it is not difficult to think of the fact that the quality is strongly dependent on X-ray phosphors. This section reviews commonly used X-ray imaging phosphors.

One of the most successful storage phosphor materials is divalent europium doped barium fluorobromide ($BaFBr_2$:Eu^{2+}) [11]. Excited charges are trapped at Eu^{2+} photoactivator sites and blue emissions are stimulated by red light exposure (for example

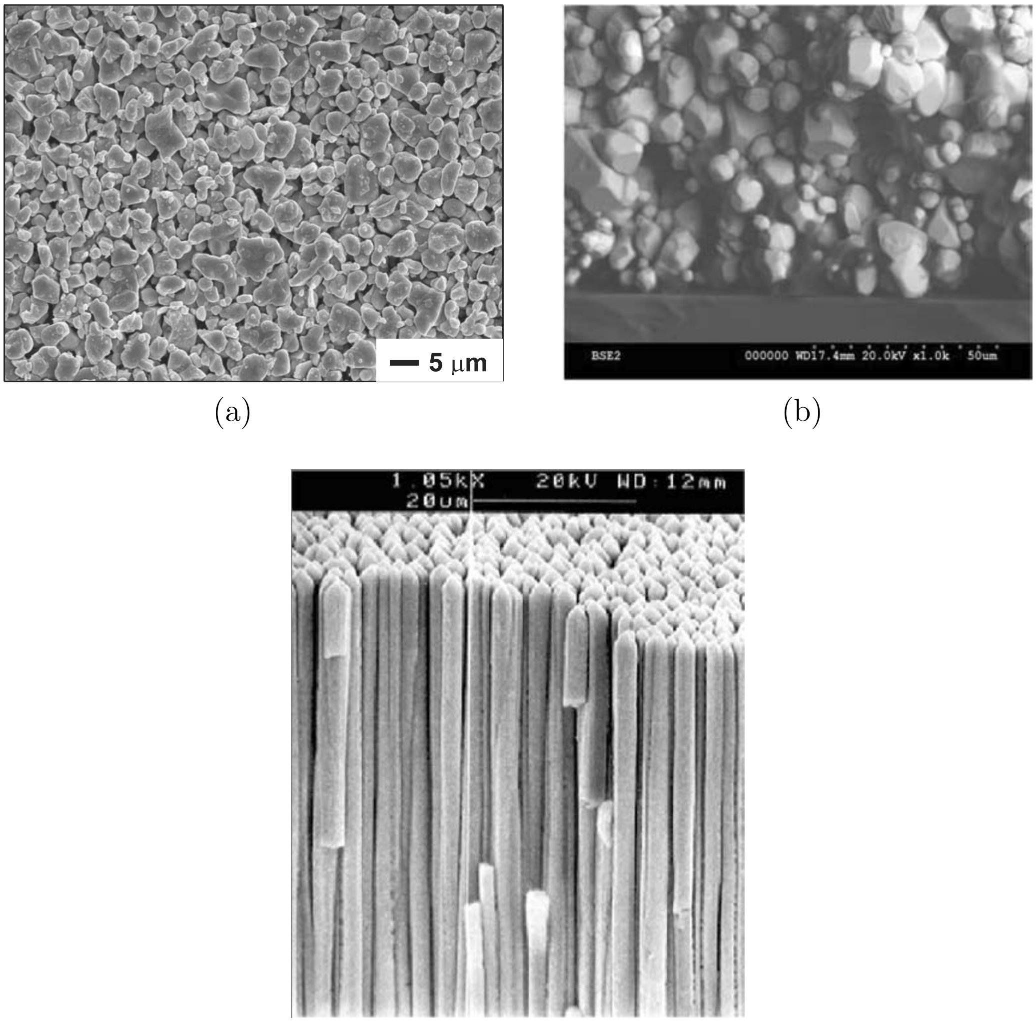

(a) (b)

(c)

Figure 2.6: Cross-sections of commonly used phosphors: (a) BaFBr imaging plate [18], (b) GOS scintillator plate [19], and (c) columnar-structured cesium iodide (CsI:Tl) scintillator plate [20].

a He-Ne laser). Particularly for this type of storage phosphor, 75 % of the original image information still remains even 8 hours after irradiation [21].

$BaFBr_2$:Eu^{2+} is sensitive to X-ray, so it has a good conversion efficiency (energy conversion from incident X-ray to output light). Typically, an imaging plate has a large dynamic range, which allows highly accurate representation of X-ray intensity levels. Also, $BaFBr_2$:Eu^{2+} imaging plates can be fabricated in a large area relatively easily compared to that of direct conversion detectors. Therefore, this method has an important advantage when an imaging target is larger than the coverage area of direct conversion detector.

Computed radiography enables us to obtain excellent image quality over film-based image acquisition in the sense that a single image element is as small as the readout laser focal point, and due to the conversion of information to a digital form. This is true compared to traditional analog methods. However, in practice, there are some causes that reduce the spatial resolution. Figure 2.6 (a) shows a cross section of $BaFBr_2$:Eu^{2+} imaging plate. As seen in the figure, $BaFBr_2$:Eu^{2+} is used in the form of a fine powder. This is because it is very difficult to prepare a $BaFBr_2$ single crystal plate in a large area with a reasonable physical strength and without significant crystalline defects, which causes a loss of image information; as well as, a single crystal growth needs time-consuming processes. However, during the readout process, a finely focused stimulation light beam experiences scattering at the imaging plate due to the polycrystalline nature and opaqueness of the material. As a result, the well-focused light spot will be broadened and the surrounding area will also be stimulated undesirably. Moreover, the stimulated light emission will also be scattered as it travels in the phosphor medium. These undesirable light scattering phenomena cause a significant reduction of the spatial resolution. It is possible to reduce the light scattering by reducing the thickness of the imaging plate. However, it has to be thick enough to absorb X-ray photons efficiently. Further, $BaFBr_2$:Eu^{2+} is hygroscopic (it absorbs moisture from the air), so it has to be placed in an enclosure such that it does not cause a reduction of the image quality.

Gadolinium oxysulfide (Gd_2O_2S; GOS) is a common scintillator material for X-ray imaging applications and also for other ionizing radiation detections such as γ-rays. Figure 2.6 (b) shows a cross section of a GOS scintillator. Since a single crystal GOS is difficult to obtain in a large area, typically it is used in polycrystalline. Since it has a high density and a high average atomic number, the scintillation efficiency is very high. However, as in $BaFBr_2$ phosphor described above, due to its crystalline defects as well as the opaqueness of the material, emitted light experiences significant scattering as it travels in the scintillator layer. As a result, the scattering of light leads to the blurring of an image, and hence reduces the spatial resolution.

In recent years, a structured phosphor has been developed in order to reduce the scattering of emitted light and the resulting light spread [22]. Figure 2.6 (c) shows an example of a cross section of a structured scintillator. This type of scintillator screen is made of a bundle of fine columns (like optical fibres), so that the emitted optical photons travel along them, i.e. the emitted light is guided along the columns. As a result, the spatial resolution is dramatically improved. Although optical separation of the columns is not perfect and crosstalk of the emitted light is not eliminated in practice, in this way the broadening of light emission can be reduced and this allows thicker phosphor layers to be used while maintaining spatial resolution. Commonly, rare-earth doped NaI and CsI are structured this way for both as a storage phosphor and scintillator. However, these phosphors are hygroscopic materials, so encapsulation is required.

2.2 Review of Rare-Earth doped Fluorozirconate Glass-Ceramics for Digital Radiography

Glass-ceramics consist of a glass matrix which contains small crystals called crystallites. The crystallite size ranges from nanometers to microns with a volume fraction of up to several tens of percent. Typically, they are produced by thermal treatment of a glass to induce the crystallites growth, and the crystal size is thermally controlled, for example, by controlling the anneal temperature and time. Glass-ceramics share many properties with both glasses and ceramics. A well-known property is its small volume expansion over a wide range of temperature due to a well controlled balance of thermal expansion coefficients between the crystals and the host glass matrix. Such a notable characteristic finds applications in a wide range of areas, for example, artificial joints, machinable ceramics, fire-doors, cookware, magnetic disk substrate, telescope mirror blanks.

Transparent glass-ceramics, in which the host glass matrix and crystals are transparent, have been of great interest for photonic applications over the past decade. In general, embedded crystallites act as light scattering centres. However, in practice the effect is not large and the transparency is equivalent to that of a pure glass when the crystal size is maintained less than $\sim$ 50 nm [23]. For example, a laser application of a glass-ceramic has achieved a comparable up-conversion intensity to the best achievement in single crystals and as transparent as the precursor glass.

Our objective is to characterize transparent glass-ceramics for X-ray imaging scintillator applications. This section reviews the literatures on rare-earth doped fluorozirocnate glass-ceramics for X-ray phosphor applications.

2.2.1 Rare-Earth doped Fluorozirconate Glass-Ceramics

Fluorozirconate (FZ) glasses are heavy-metal fluoride glasses based on the glass-forming properties of zirconium fluoride. A well-known and promising material for optical communications for its excellent optical transmittance, a ZBLAN glass is a member of this family, which is composed of fluorides of zirconium, barium, lanthanum, aluminum, and sodium [24].

There have been two types of FZ glass-ceramics that have been reported for X-ray imaging applications: fluorobromoziroconate (FBZ) and fluorochlorozirconate (FCZ). The former is produced by replacing F^- ions with Br^- ions. Upon heat treatment, $BaBr_2$ nanocrystals grow in the FBZ glass matrix, resulting in an FBZ glass-ceramic. In 1999, Edgar et al. [25] first observed a notable PSL effect from this glass-ceramic doped with divalent europium (Eu^{2+}). Later, Schweizer et al. [26] found, from FCZ glass-ceramics, a significant PSL conversion efficiency of 80 % that of $BaFBr:Eu^{2+}$, which is the standard material for X-ray imaging plates. FCZ glass-ceramics have been produced by replacing Br^- ions in FBZ glasses with Cl^- ions and then by heat treatment, in which the formation of $BaCl_2$ nanocrystals is induced.

2.2.2 Nanocrystals in Glass-Ceramics as X-ray Phosphors

It had been found that nanocrystals in both FBZ and FCZ glass-ceramics play an important role for X-ray phosphor applications. For example, as-prepared samples, which do not contain nanocrystals, do not show PSL effects. However, a significant PSL effect is observed in FBZ/FCZ glass-ceramics, in which nanocrystals are embedded in the glass matrix and the nanocrystals are induced by heat treatment. This fact suggests that the PSL effect is possible only in the induced nanocrystals. It is instructive to mention here that it has been reported that rare-earth doped $BaBr_2$ and $BaCl_2$ single crystals show a PSL effect [27, 28]. An example SEM (Scanning Electron Microscope) image of an FCZ sample is illustrated in Figure 2.7.

The nanocrystal size depends on the heat treatment conditions (annealing temperature and time). Typically, shorter-time and lower-temperature annealing leads to smaller size nanocrystals, while longer-time and higher-temperature result in larger nanocrystals embedded in the host matrix [29, 30, 31]. For photostimulable luminescence in FBZ and FCZ glass-ceramics, the conversion efficiency increases as the nanocrystal size increases [32, 33, 34]. However, the nanocrystal size should be maintained sufficiently small to maintain the transparency since larger nanocrystals dispersed in the glass matrix act as light scattering centres, which reduce the transparency.

$BaBr_2$ and $BaCl_2$ are highly hygroscopic. Another advantage of this glass-ceramic is that the encapsulation of the nanocrystals is easily achieved by heat treating a glass sample.

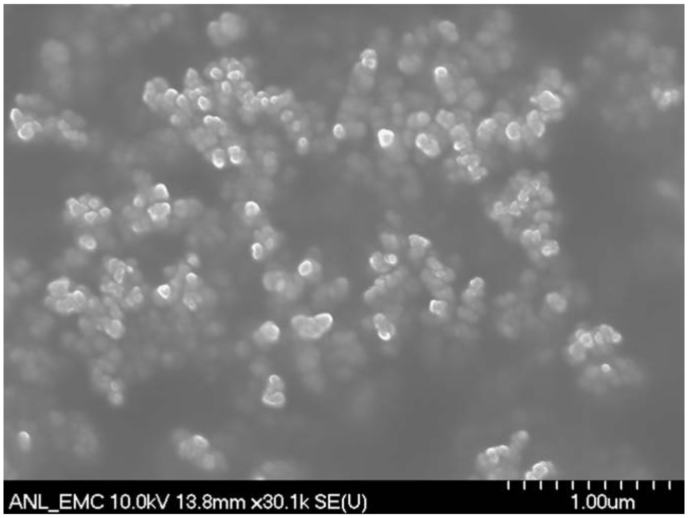

Figure 2.7: A SEM image of annealed europium doped FCZ sample. Average size of the nanocrystals in the picture is approximately 100 nm. From [35].

2.2.3 Transparent Phosphors and Image Resolution

Transparent phosphors have advantages for X-ray imaging applications for several reasons. As described in Section 2.1.3, powdered $BaFBr_2$ has been used as a standard imaging plate; however, the significant optical scattering during the readout process limits further improvement of the spatial resolution. Transparent imaging plates can minimize this scattering, and it has been found that transparent FCZ glass-ceramic imaging plates exhibit much improved spatial resolution, by a factor of 5 compared to the conventional storage phosphor, $BaFBr_2:Eu^{2+}$ [34, 36].

It has been reported that transparent phosphors potentially give a good image resolution for X-ray scintillator applications. This is because transparency to its emission light does not cause light scattering as it travels in the scintillator screen. Touš et al. [37] reported that, with a transparent single crystal YAG:Ce scintillator screen, 4 times better resolution has been achieved compared to that of a common GOS scintillator. Nagarkar et al. [38] have achieved an enhanced spatial resolution while maintaining a high light yield from a pixelated transparent scintillator which was made by cutting narrow deep grooves on a transparent $Lu_2O_3:Eu$ scintillator. For transparent FZ glass-ceramics, Chen et al. [39] have obtained X-ray images with a good image quality (though objective evaluation was not presented) by placing a divalent europium doped FCZ ($FCZ:Eu^{2+}$) glass-ceramic onto a CCD camera. The images are illustrated in Figure 2.8. To date, unlike imaging plate applications, FBZ and/or FCZ glass-ceramics have not been extensively studied for X-ray scintillator applications.

In order to obtain transparent glass-ceramics, growth of nanocrystals in the glass matrices has to be well controlled. In general, as the nanocrystal size increases, the transparency decreases. Also, higher-temperature and longer-time heat treatment result in larger nanocrystals to grow. Tick [40] has suggested that it is possible to produce ultratransparent glass-ceramics, which has an equivalent transparency to

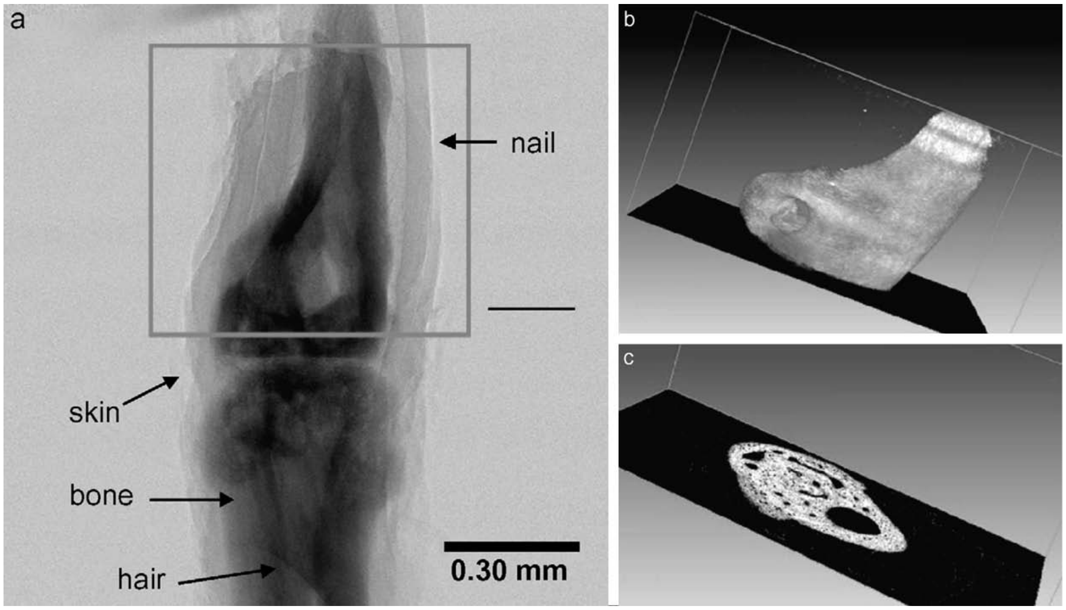

Figure 2.8: An example X-ray images of a mouse joint taken with a 2%Eu-doped FCZ glass cramic scintillator plate. (a) A projection X-ray image, (b) a computed tommograph, and (c) a cross section from the CT. From [39].

that of pure glasses, under appropriate conditions of nanocrystal size and crystallite volume fraction. Thermal properties of rare-earth doped (Sm and Eu) FCZ glass-ceramics have been extensively studied [34, 41, 42], and it has been suggested that the nanocrystal formation temperature lies around 220 to 250 °C, and that crystallization of the glass matrix takes place around 280 to 300 °C. Tonchev et al. [41] reported that these temperatures depend on the Cl^- content with respect to that of F^- ions (Cl/(Cl+F)%) and increase with the fraction of Cl^-. Therefore, heat treatment in a temperature range from the onset of nanocrystal formation to the crystalliztion of glass matrix would enable us to create a transparent glass-ceramic phosphor containing nanocrystals.

2.2.4 Luminescence

Luminescence spectrum from a phosphor strongly depends on the activator – very often rare-earth ions are embedded and act as the activator. FBZ/FCZ glass-ceramics are not exceptions and have been doped with some rare-earths ions in trivalent and/or divalent electronic states for various phosphor applications.

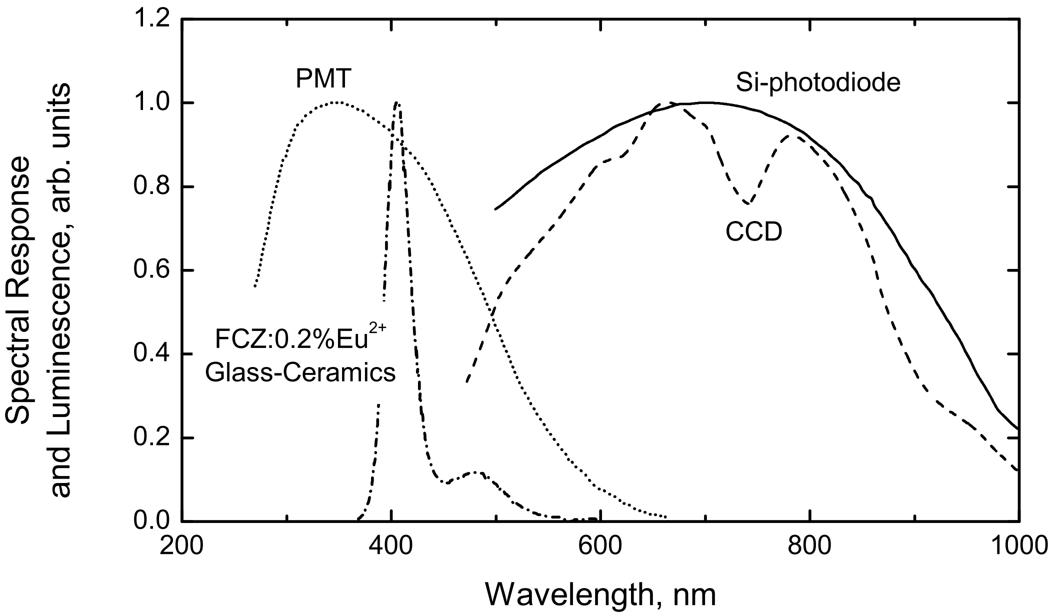

Figure 2.9: Normalized spectral responses of photodetectors — PMT (Hamamatsu, R7600U) [43], Si-photodiode (Hamamatsu, S1226) [44], and CCD (Hamamatsu, S9979) [45] and a luminescence spectrum of FCZ:Eu^{2+} glass-ceramic [46].

Divalent europium (Eu^{2+}) doped FBZ and FCZ glass-ceramics have been most extensively studied for digital radiography applications. Upon X-ray excitation, both fluorescence and photostimulated luminescence are expected in the UV-blue region ($\sim$ 380 – 500 nm) associated with the allowed $4f^6 5d^1 \rightarrow 4f^7$ transitions [47]. Figure 2.9 shows a luminescence spectrum of FCZ:Eu^{2+} glass-ceramic [46] and typical spectral responses of photodetectors corresponding to a photomultiplier tube (PMT) [43], Si-photodiode [44], and CCD [45]). As seen in the figure, the UV-blue emission is in a good agreement with spectral response of the PMT. Therefore, during the readout process, the photostimulated light can be detected by a PMT.

Soundararajan [48] and Henke et al. [49, 50] have studied trivalent erbium doped FCZ (FCZ:Er^{3+}) glasses and glass-ceramics. Its long lifetime at 1550 nm corresponding to the $^4I_{13/2} \rightarrow ^4I_{15/2}$ transition, which is commonly used telecommunications, suggests it to be an excellent candidate material for photonic devices such as an optical amplifier. Moreover, the strong up-converted emission in the green region suggests a large potential for use as an up-converter layer for new generation solar cells, which plays an important role in increasing efficiency by matching the spectral response to that of the sun light.

For scintillator applications (direct readout), a UV-blue light emission from Eu^{2+} doped fluorozirconate glass-ceramics is not preferred because conventional silicon-based image sensors, for example a CCD, CMOS, and a-Si TFT arrays, are more sensitive in the red region [51, 52]. This spectral mismatching can also be confirmed in Figure 2.9. In contrast, divalent samarium (Sm^{2+}) ions embedded as luminescence activators show, in many materials, strong red emissions associated with the 5d-4f and 4f-4f transitions. This emission range ($\sim$ 650 nm) is better matched to the spectral sensitivity of today's silicon detectors as seen in Figure 2.9.

The spectroscopic study of, especially, sharp 4f-4f emissions is also of interest for other reasons. The 4f-4f fluorescence can be an effective probe for understanding the unique properties of fluorozirconate glass-ceramics discussed in the previous sections:

1. *Nanocrystal size* : Spectral broadening of a sharp emission peak would be used as a probe for the nanocrystal size. Generally speaking, the size of nanocrystals can be estimated by XRD studies, which takes into account the broadening of the X-ray diffraction peak. However, a further line broadening can be caused by other factors, for example crystalline strains. For luminescence in crystals, a spectral emission broadening can be observed due to crystalline defects which have higher density near the surface. Defect density is minimum for a single bulk crystal for its low surface to volume ratio, meanwhile as the crystal size

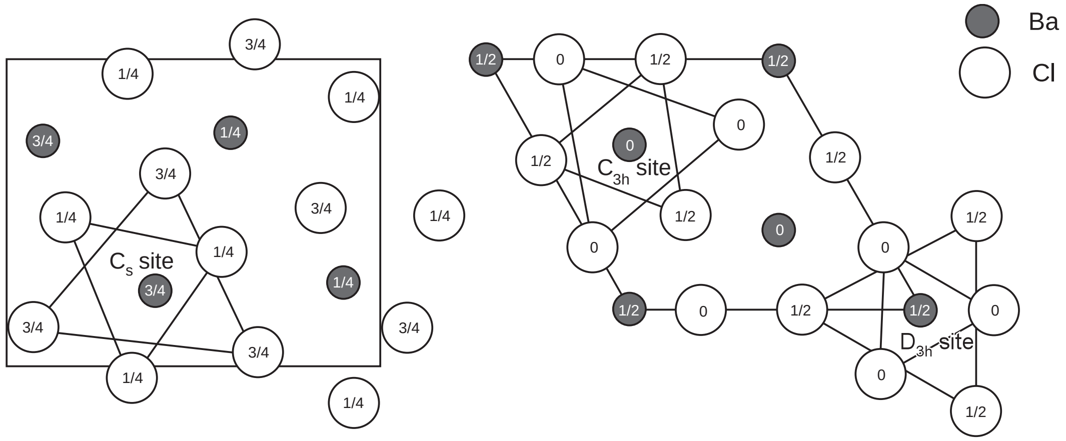

(a) Orthorhombic $BaCl_2$

(b) Hexagonal $BaCl_2$

Figure 2.10: A schematic diagram of projected (a) the orthorhombic structure and (b) hexagonal structure of $BaCl_2$. Numbers indicated at each atom represent the atomic planes. The sketches are based on [29, 54].

decreases, greater spectral broadening would be expected. 4f-5d transitions, as seen in FBZ/FCZ doped with Eu^{2+}, are too broad for this type of broadening effect to be observed. However, the sharp 4f-4f transitions can be used to estimate the nanocrystal size as shown in this work.

2. *Substitution of rare-earth ion into the nanocrystals* : Some rare-earth doped FBZ/FCZ glass-ceramics have shown that the rare-earth ions are embedded in the nanocrystals during the nucleation and growth, but some others remain in the glass matrix. Spectroscopic studies of a $BaCl_2$:Sm^{2+} single crystal have been done by Lauer and Fong [53]. Comparing our data with their data will enable us to confirm whether or not the luminescent Sm ions is embedded in the $BaCl_2$ nanocrystal.

3. *Crystal structure* : Earlier studies from powder X-ray diffraction analyses have suggested that the $BaBr_2$ and $BaCl_2$ nanocrystals appear either in the orthorhombic or hexagonal crystal structures in the FBZ and FCZ glass matrices, respectively. Also, the size of nanocrystals depends on the heat treatment conditions. Single crystal studies [53] have shown a 3-line splitting for the $^5D_0$ to $^7F_1$ transition for the C_s point group symmetry in the orthorhombic $BaCl_2$

> as in Figure 2.10 (a). In contrast, the hexagonal barium chloride has two crystallographically distinct Ba sites (C_{3h} and D_{3h} point group symmetries) as illustrated in Figure 2.10 (b). The luminescence activators substituting Ba ions at both the sites should experience different crystal fields, and as a result these activators may show different peak splitting in the spectra. The investigation of these sharp transitions would give us new knowledge to distinguish the two crystal structures. Further analysis may unveil the position of photoactivator ions in the nanocrystal and the local crystal structures. It is worth pointing out that the hexagonal phase is metastable at room temperature.

It is instructive to mention that these effects have appeared only in a few literatures, and that Eu^{2+} doped FBZ/FCZ have shown mainly broadband emission corresponding to the 4f-5d energy transition and the forbidden 4f-4f transitions are too weak to study.

2.2.5 Valency Conversion

The preparation of divalent samarium doped FCZ glasses is a challenge. In order to dope the glass with divalent samarium while maintaining the FCZ glass composition, SmF_2 or $SmCl_2$ is required; however, these are not commercially available today. In the case of some oxide glasses, researchers have attempted to initially dope the material with Sm^{3+} ions and then to reduce the valency state to the “2+” by irradiating with X-rays [55], γ-rays [56], or a femtosecond laser [57], or by annealing samples in a hydrogen atmosphere [58].

Figure 2.11 shows photoluminescence spectra of a Sm-doped Al_2O_3–SiO_2 glass before and after X-ray irradiation for 14 hours at room temperature, which was reported by Nogami et al. [59]. The sample before the irradiation shows luminescence from Sm^{3+}. While after the irradiation, it has been observed that Sm^{2+} divalent ions contribute to additional luminescence at higher wavelengths. Such a spectral

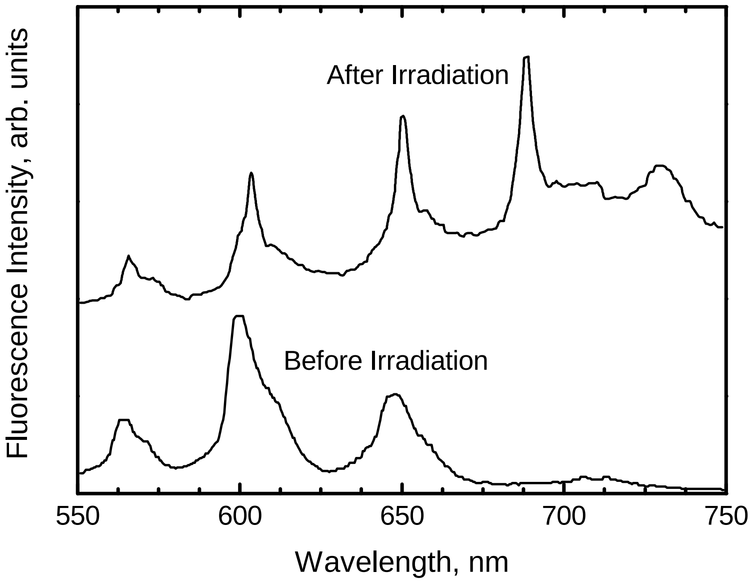

Figure 2.11: Photoluminescence spectra of a sample (Al_2O_3–SiO_2 glass) doped with Sm ions before and after X-ray irradiation. Before the irradiation, a spectrum only from Sm^{3+} is only seen. While both the spectra from Sm^{3+} and Sm^{2+} were observed after the X-ray irradiation. Reproduced from [59].

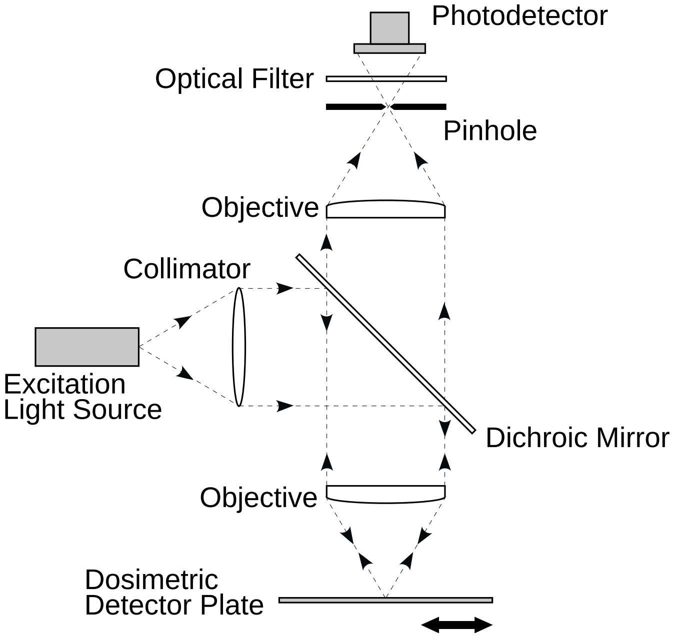

Figure 2.12: A schematic diagram of a confocal microscope used to obtain a dose profile in microbeam radiation therapy applications.

change due to the valency conversion by X-ray irradiation is of great interest in high resolution, high dose dosimetry. In applications requiring high resolution, a confocal microscope readout can be used as shown in Figure 2.12. When confocal microscopy is combined with a Sm-doped plate, which exhibits a valency conversion of rare-earth ions upon interaction with X-rays, the system would enable us to obtain a very high resolution image of the X-ray intensity pattern. This technique is currently being studied to obtain a dose profile for microbeam radiation therapy at the Canadian Light Source.

In the case of fluorozirconate glasses, MacFarlane et al. [60] have been able to convert Eu^{3+} ions to the divalent state in FCZ glasses by adding alkali hydrides (for example LiH, NaH, $LiBH_4$, or $ZrH_{1.9}$) into the glass melt. A valency reduction of Sm ions in fluorozirconate glasses has not been reported; we have attempted Sm^{3+} to Sm^{2+} reduction by the addition of an alkali hydride in this work.

Chapter 3

Experimental

This chapter discusses general experimental setups and procedures involved in the research. The following section explains the preparation method of a divalent samarium doped Fluorochlorozirconate (FCZ:Sm^{2+}) glass. The as-prepared sample was further heat treated to induce nucleation and growth of crystallites, which is described in Section 3.2. We have carried out powdered X-ray diffraction (XRD) analysis, explained in Section 3.3, to examine the existence of crystallites, the average size, and crystal structure. We obtained the absorption coefficients of our samples from the optical transmittance spectra, whose experimental details are provided in Section 3.5, and we used them to examine the valency reduction and substitution of samarium ions as a photoactivator into the crystallites.

3.1 Sample Preparation

Our objective was to prepare divalent samarium doped fluorochlorozirconate (FCZ:Sm^{2+}) glasses. This section briefly provides important information involved in the preparation of these glasses.

The composition of the FCZ glass was 53%ZrF_4, 20%NaF, 3%AlF_3, 3%LaF_3, 1%SmF_3, 1%BaF_2, 19%$BaCl_2$ by molar percentage. This composition was derived from a well-known ZBLAN glass [61]. All the samples were prepared by Andy Edgar and Chris Varoy from a collaborating research group at the School of Chemical and Physical Sciences, Victoria University of Wellington, New Zealand. At first, all the anhydrous constituents were mixed in a glove box in a dry nitrogen atmosphere.

This mixture was loaded into a glassy carbon crucible, and then placed in an RF induction furnance attached to the dry box. Since samarium ions are not commercially available in divalent form, MacFarlane et al. [60] previously showed that trivalent europium ions doped in fluorozirconate glasses had been effectively reduced to divalent state by adding a few percent of alkali hydrides or borohydrides to the melt. Therefore, a common reducing agent of $NaBH_4$ (0.25, 0.1, 0.25, 0.35, and 1 molar %) was added in our glass melt. The melt was heated to 825 °C in an argon atmosphere with occasional stirring. 30 min later, the melt was splat quenched between two brass blocks heat at 190 °C.

3.2 Heat Treatment

FCZ glass-ceramics are known to have $BaCl_2$ nanocrystals inside the glass matrix upon heat treatment [29, 30, 31]. Depending on the temperature and time, the crystal size and its crystal structure may vary. We, therefore, annealed as-prepared glass samples for different times at different temperatures in a mixture of hydrogen and argon or nitrogen atmospheres.

Our setup for heat treatment is illustrated in Figure 3.1. Samples were placed in a sample holder, which had two thermocouples (K type) attached to it to measure the temperature on the inside and outside of the sample holder. The holder was made of brass, which has an excellent thermal conductivity. The thermocouple temperatures were read by an Omega Microprocessor Thermometer HH2. The sample holder was loaded into the quartz tube, which was heated in the furnace (typically $\sim 250 - 300$ °C depending on the heating condition). The furnace temperature was controlled by the temperature controller (S-03C, VEZAS Ltd.). The quartz tube with the sample holder was sealed such that only the annealing gas filled up in the tube. The annealing gas was supplied from a cylinder to the quartz tube through a flow meter (TA Instruments, PN 270134.003) to monitor and maintain the gas flow. The heat treatment procedure was as follows:

1. Inside of the furnace was kept at a desired temperature.
2. The annealing gas (nitrogen or a mixture of 5 % hydrogen and 95 % argon) was supplied into the quartz tube at a desired flow rate (typically $\sim$ 1.0 L/minute).
3. The sample was placed inside the sample holder and loaded at the entrance of the quartz tube in which the temperature was approximately 50 °C. This temperature does not cause a glass transition since the glass transition temperature from DSC (Differential Scanning Calorimetry) is known to be higher than $\sim$ 220 °C [41].

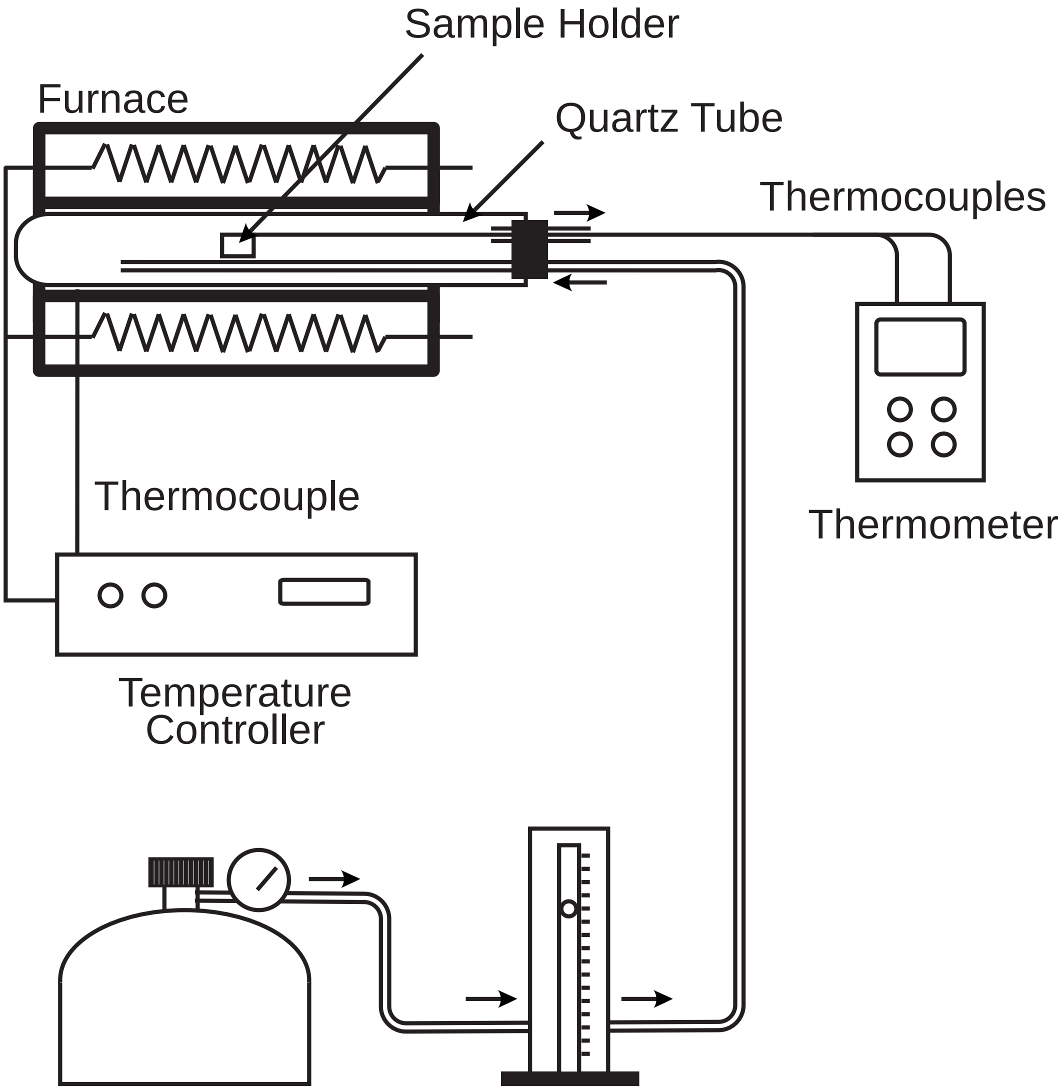

Figure 3.1: An illustration of heat treatment experimental setup.

4. The quartz tube was sealed and held until the tube was filled up with the required gas. Typically, this process would take ~ 5 min.

5. The sample holder was loaded further into the quartz tube to heat the sample at the desired temperature. It typically took approximately 5 minutes to reach the desired temperature.

6. Once the sample temperature reached to the desired temperature, the sample was held at the same position at a constant temperature for a desired time period. This period is defined as the annealing time.

7. The sample holder was brought back to the entrance of the quartz tube to slowly cool down to the ambient temperature. This process typically took approximately 5 minutes.

8. Finally, the tube was unsealed and the sample was taken out of the tube.

Figure 3.2: The work station of annealing experiment.

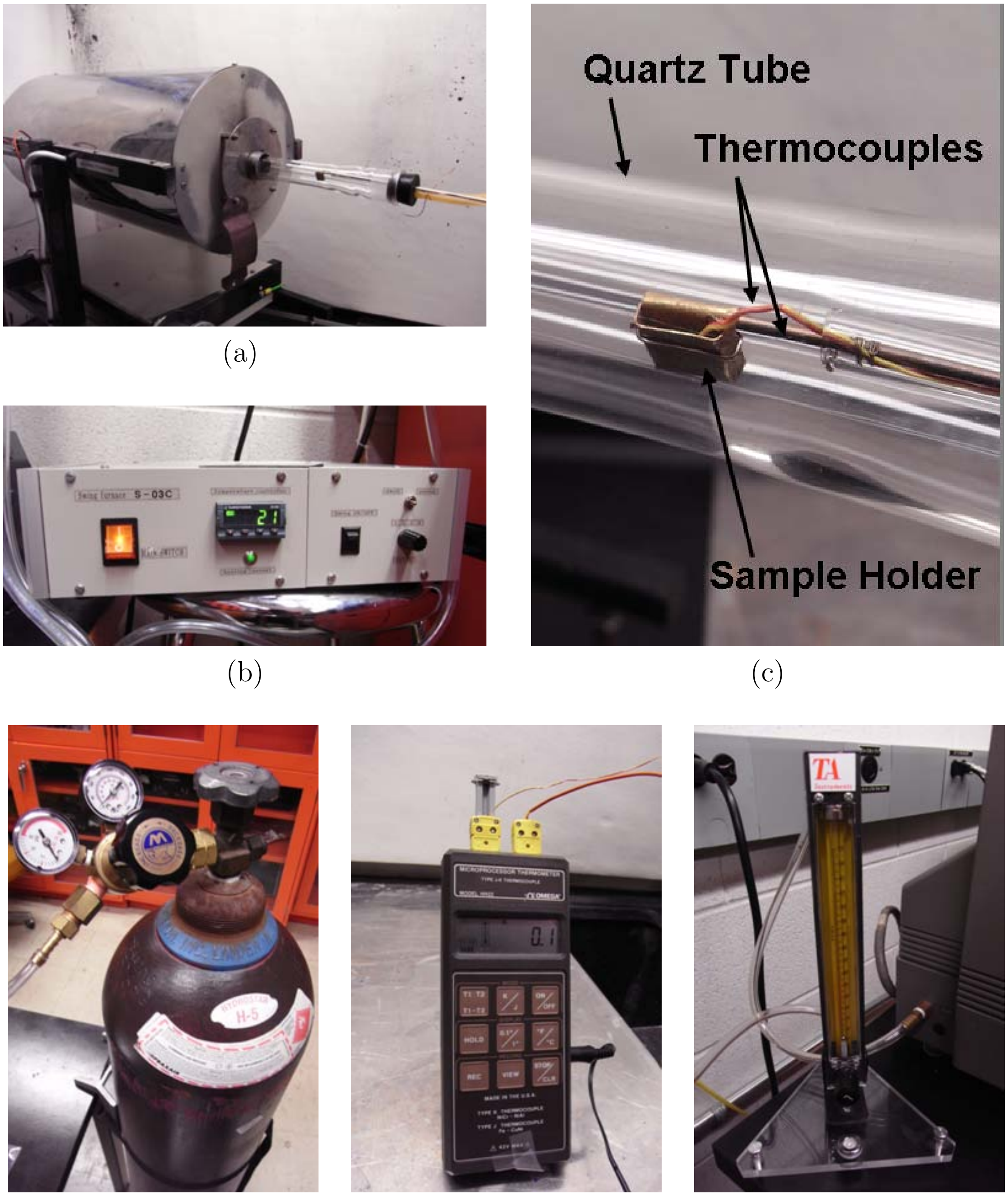

(a)

(b)

(c)

(d)

(e)

(f)

Figure 3.3: Equipments used for annealing experiments: (a) furnace and quartz tube with a sample holder, (b) temperature controller, (c) sample holder with thermocouples in a quartz tube, (d) gas tank, (e) thermometer, and (f) flow metre.

3.3 X-ray Diffraction

Powder X-ray diffraction (XRD) experiments were carried out in order to study nucleation and growth of expected crystallites in the glass matrix upon heat treatment. A standard powder diffractometer and a cobalt tube were used. The spectra were recorded at room temperature. All the XRD experiments were carried out by a collaborating research group at the School of Chemical and Physical Sciences, Victoria University of Wellington, New Zealand.

3.4 Differential Scanning Calorimetry

We have studied the thermal properties of our glass and glass-ceramic samples using a differential scanning calorimeter (DSC) (Q100, TA Instruments) equipped with a fast air cooling system. Figure 3.4 shows the photograph of the DSC instrument used. A small piece of the sample (less than 10 mg) was first weighted, placed in an aluminum pan, and then hermetically sealed. An empty pan was used as the reference. Typically a heating rate of 10 K/min was used, and the DSC scan was taken up to a temperature of 530 °C.

Figure 3.4: A differential scanning calorimeter (Q100, TA Instruments).

3.5 Optical Absorption

Optical absorption characterizes the absorption of photons as light propagates along a certain direction in a medium. It is the fractional change in the intensity of light per unit distance along the propagation direction [62]. It is experimentally obtained by the following relationship

$$\alpha(\lambda) = -\frac{1}{L}\ln(T(\lambda)) \tag{3.1}$$

where $\alpha(\lambda)$ is the optical absorption coefficient, L is sample thickness, and $T(\lambda)$ is transmittance as a function of wavelength, which is the fraction of transmitted light intensity over the incident light intensity. Thus, upon obtaining the sample thickness and transmission spectra, the absorption coefficient is obtained. Before the optical measurements, all the samples were polished. Next, sample thicknesses and transmission spectra were measured. This section explains the general procedure involved in the acquisition of optical transmission and absorption spectra.

3.5.1 Grinding and Polishing

Before any transmittance measurement is carried out, samples must be ground and then polished. Grinding is done to obtain parallel surfaces on both sides of the sample. Polishing removes roughness and imperfections on the surface. Those treatments minimize reduction of light transmission of the sample due to random scattering and imperfection of sample geometry. Also, all the samples must have practically the same conditions on their surfaces in order to ensure that the differences in the transmittance spectra are not due to differences in the surface roughness.

The procedure involved in grinding is as follows [48]:

1. Grinding was performed on a glass plate shown in Figure 3.5. 600 micron silicon carbide powder and 100 % ethanol were placed on the plate and then mixed.

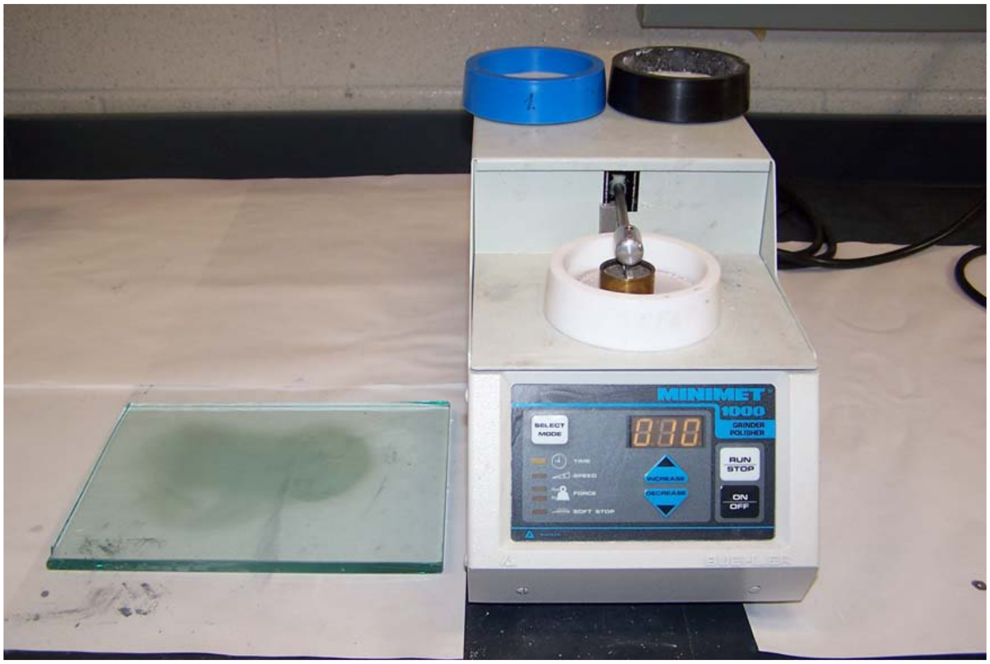

Figure 3.5: A Buehler Minimet 1000 Polisher. The image was extracted from [48].

2. A sample was placed on top of the mixture and then ground by slowly making circular motions with hand. During the process the powder and ethanol were added as needed. This process ensures that we have a flat surface on one side of the sample.

3. The sample is then glued on a sample holder. The sample holder was first heated on a Thermolyne HP2305B heater to approximately 80 °C, to melt bee's wax. A small amount of bee's wax was then placed on top of the holder. Next, the sample was placed on the melt with the flat surface down. Last, the sample holder was taken out from the heater to cool down in order to solidify the bee wax, thereby holding the sample firmly in place.

4. The sample was again ground as described before, but with the sample holder this time. Since the sample holder has an adjustable gap between the edge and the center (see Figure 3.6), parallel surfaces on both sides are maintained.

Once the sample was ground and parallel and flat surfaces were obtained at both

Figure 3.6: From left to right: Bee's wax, a heater (Thermolyne HP2305B), and a sample holder. The image was extracted from [48].

Figure 3.7: Materials used for polishing. From left to right: 100 % ethanol, silicon carbide powder, 3 micron alumina powder, 0.05 micron alumina powder and an ethanol + glycol mixture. The image was extracted from [48].

sides of the sample, the sample was then fine polished with a Buehler Minimet 1000 Polisher which is shown in Figure 3.5. Polishing was performed inside a bowl which has a glass plate at the bottom to which a polishing cloth is glued. The bowl was placed in position under the arm of polisher. Inside of the bowl, the sample holder, with the sample firmly attached by the bee's wax, was securely held in position by the polisher arm with the sample side down. The sample was then polished by having the polisher arm move in circular motions. Polishing powder and a few drops of ethanol + glycol to act as a lubricant were added as needed. The polisher controls the speed of the arm motion from 0 to 50 rpm, the force of the arm from 0 to 10 lb, and polishing duration 30 seconds to 99 hours. The fine polishing process involves three stages as follows:

1. The first polishing was performed on a rough polishing cloth with a few drops of a mixture of ethanol and glycol without polishing powder. At the end of this stage, the sample should look a little glazed compared to the dull look after grinding. This process typically required 1.5 hours with 15 rpm of the arm speed and 1 lb of arm force for an approximately 1×1 cm^2 of sample size.

2. The second stage is to obtain clear glass-like surface. The sample was polished on a smooth polishing cloth attached to the glass plate. 3 micron alumina powder was evenly dispersed on the cloth and a few drops of ethanol + glycol are added as needed. This stage typically required 1 hour with 30 rpm of polisher arm speed and 1 lb of arm force.

3. The last stage ensures the sample is highly polished. The polishing was performed on a smooth polishing cloth glued on a glass plate. For further enhancement, 0.05 micron alumina powder was used as in the previous stage, and also a few drops of ethanol + glycol mixture are occasionally added as a lubricant agent. This stage typically took 1 hour with 40 rpm of arm speed and without arm pressure.

After the third stage, the sample was removed off the sample holder by heating and melting the bee wax on the heater. The sample was then flipped and glued on the sample holder as described above. The entire polishing procedure was repeated for the other side of the sample. 100 % ethanol and dietyl ether were used to clean the sample and/or the equipment as needed. The variation of thickness is ± 15 μm.

3.5.2 Transmission Spectrum Measurement

Transmittance spectra were measured using a Perkin Elmer Lambda 900 spectrometer. Schematic diagram of the experiment is illustrated in Figure 3.8. Also, a photograph of the work station is shown in Figure 3.9.

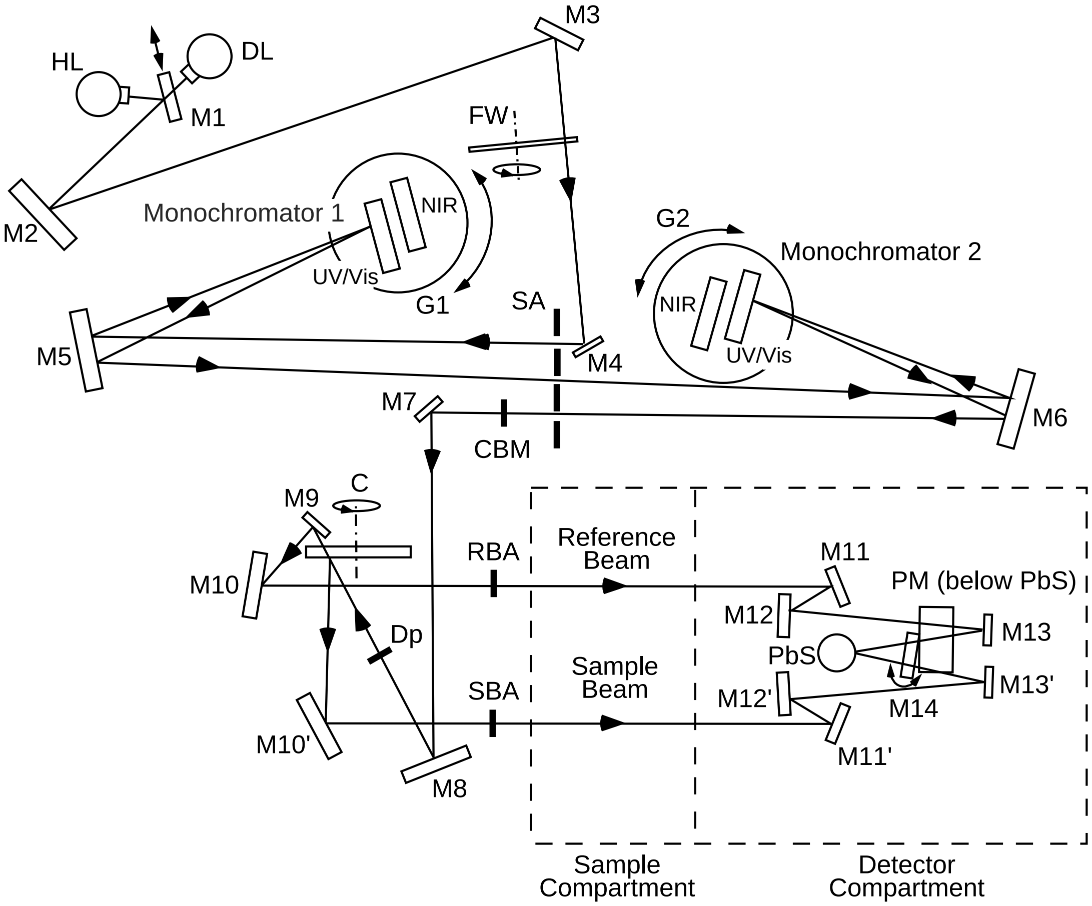

Figure 3.8: An illustration of schematic diagram of a spectrophotometer (Perkin Elmer Lambda 900). The diagram was reproduced from the manual.

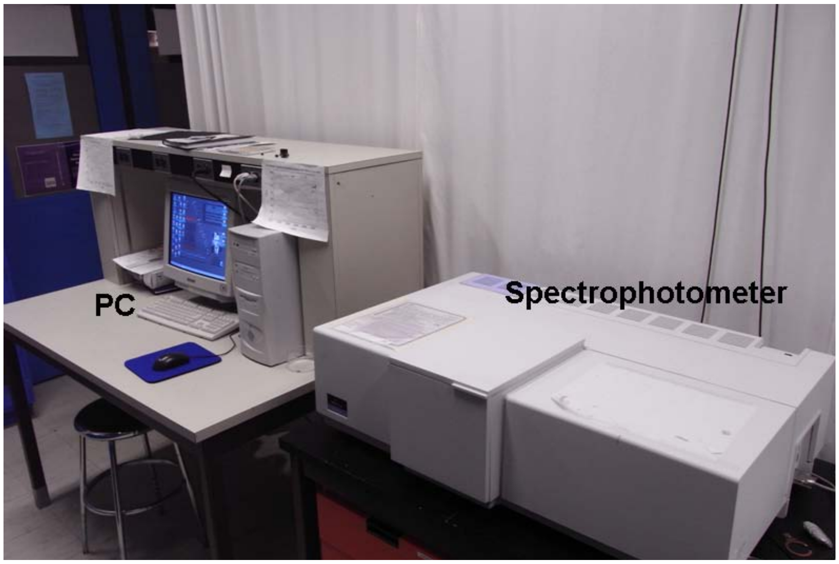

Figure 3.9: The work station for optical transmission measurements.

As a radiation source, a deuterium lamp (DL) was used to cover the ultraviolet range, and a halogen lamp (HL) was used for the near infrared and visible ranges. The radiation source was switched by the mirror M1. This spectrophotometer uses two monochromators (G1 and G2), and each monochromator has two diffraction gratings for the UV-visible (UV/Vis) range and the near infrared (NIR) range. The beam from the radiation source was guided towards the monochromators through mirrors (M1 – M6), a slit assembly (SA), and an optical filter on the filter wheel assembly (FW). The FW was synchronized with the monochromators, and an appropriate optical filter was switched depending on the wavelength to be produced. The light beam with the selected wavelength was guided towards a chopper assembly (C) through the SA, a common beam mask (CBM), and mirrors (M6 – M8). When the chopper was not actuated, the beam was guided to the sample compartment through mirrors (M9 and M10) to create the reference beam, which was then measured ether by a photomultiplier (PM) or a Peltier-cooled lead sulfide detector (PbS). The PM was used to measure the UV/Vis light beam, while the PbS was used for NIR light beam. The mirror M14 was rotated to select the desired detector. When the chopper was switched, the beam was guided to the sample through (M10'). The transmitted light beam through the sample medium was then measured by one of the detectors in the same manner as for the reference beam described above. The reference and transmitted beams were measured at each wavelength alternatingly, so the transmittance spectra over the range of interest were obtained. The CBM was mounted between the SA and M7 in order to control the height of both the reference and sample beams. The light intensities of the reference and sample beams were controlled with the attenuators RBA and SBA, respectively.

All the measurements were carried out at room temperature (23 ± 1 °C). Specifications of the spectrophotometer are listed in Table 3.1.

Table 3.1: Specifications of Lambda 900.

<table>
<tr><td>Beam cross-section</td><td><table><tr><td>Slit</td><td>Width (approx.)</td><td></td><td>Height (approx.)</td></tr><tr><td>0.05 nm</td><td>0.04 mm</td><td>×</td><td>11.7 mm</td></tr><tr><td>0.1 nm</td><td>0.09 mm</td><td>×</td><td>11.7 mm</td></tr><tr><td>0.5 nm</td><td>0.45 mm</td><td>×</td><td>11.7 mm</td></tr><tr><td>1 nm</td><td>0.89 mm</td><td>×</td><td>11.7 mm</td></tr><tr><td>2 nm</td><td>1.00 mm</td><td>×</td><td>11.7 mm</td></tr><tr><td>5 nm</td><td>4.44 mm</td><td>×</td><td>11.7 mm</td></tr></table>measured at the focal point of the sample beam and the reference beam in the sample compartment at a wavelength of 500 nm.</td></tr>
<tr><td>Grating (Monochromator)</td><td>Holographic gratings with 1440 lines/mm UV/Vis
360 lines/mm NIR</td></tr>
<tr><td>Radiation sources</td><td>Pre-aligned deuterium and halogen lamps</td></tr>
<tr><td>Detector</td><td>A photomultiplier for the UV/Vis range and
a Peltier-cooled PbS for the NIR range</td></tr>
<tr><td>Wavelength accuracy</td><td>0.8 nm UV/Vis and 0.32 nm NIR</td></tr>
<tr><td>Integration time</td><td>0.04 s to 10 s in 0.04 s increments</td></tr>
<tr><td>Digital port</td><td>One RS232C interface (serial), for connecting a PC</td></tr>
</table>

3.5.3 Sample Thickness

Sample thickness was measured using a Fowler Sylvac 50 thickness measurement unit which is shown in Figure 3.10. The unit mainly consists of four components: a thickness sensor, stage, handle, and a gauge amplifier. The thickness sensor was vertically placed on the stage in contact, and the handle controls the vertical position of the sensor. Then, the data of the position is read and displayed by the gauge amplifier. Therefore, the sample thickness can be measured by placing a sample between the sensor and stage. The accuracy is ~ 0.5 μm.

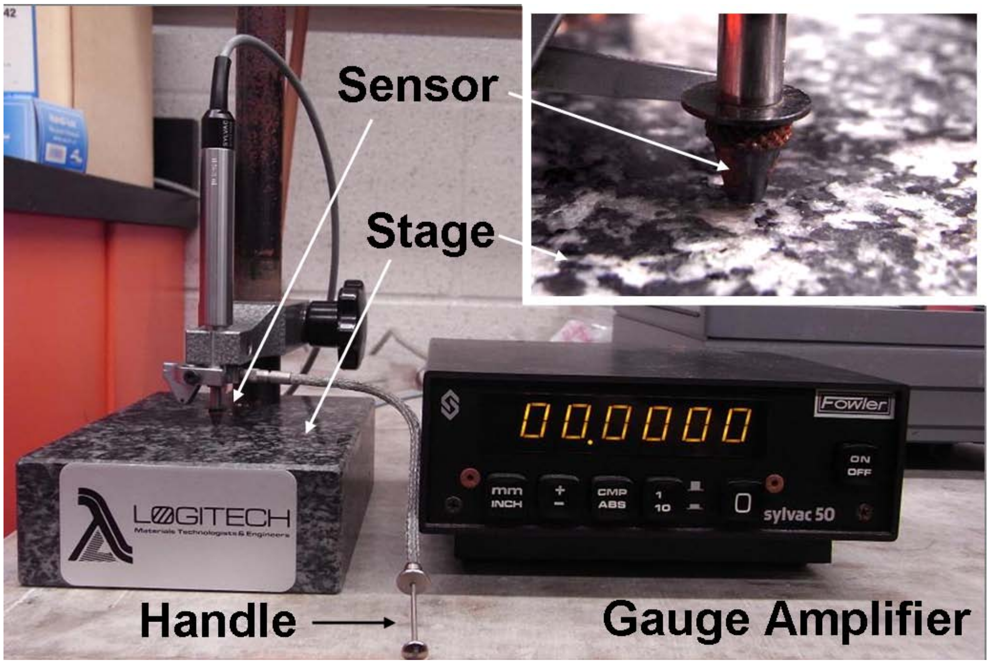

Figure 3.10: A thickness measurement unit (Fowler Sylvac 50).

3.6 Photoluminescence

In this work, steady-state photoluminescence experiments were carried out at room temperature and also at low temperatures. In this section, the experimental setup and brief procedure to perform the measurements are discussed.

The schematic diagram of a steady-state photoluminescence setup is illustrated in Figure 3.11. It consists of three parts: optics, data acquisition, and temperature control. For measurement at room temperature, the temperature control part was not used.

The optics part plays an important role for the optical measurement. A sample was excited by a UV light beam and spectrum of fluorescent light emission from the sample was measured. As the excitation light source, a halogen-xenon lamp (Spectra-Physics model 66902) was used, which covers from the UV to infrared range. A lamp power source in Figure 3.13 (b) (Spectra-Physics 69907) ensures constant power supply to the lamp, hence constant intensity of excitation light. The visible and infrared light from the radiation source was filtered by a sequence of optical filters, including a UG1 filter. As a result, UV light approximately at 360 nm, was obtained for excitation. It was then optically guided onto the sample, which was held on a sample holder as shown in Figure 3.13 (a). Upon UV excitation, emitted luminescent light was collected by an optical lens and directed toward a monochromator (Oriel Cornerstone$^{\text{TM}}$ 130 Monochromator). The incoming light was dispersed by a diffraction grating, and a desired wavelength component was selected by computer control. The selected light was then detected by a cooled InGaAs detector (Oriel InGaAs Detector Head 70347), which covers visible and near infrared regions. Figure 3.14 (d) shows the monochromator and the photodetector unit (right) mounted on the right hand side of the monochromator. The photodetector unit has the InGaAs photodetector, signal amplifier, and thermo electric cooler, which was controlled by a temperature controller (Oriel 77055) shown in Figure 3.13 (b). Cooling the pho-

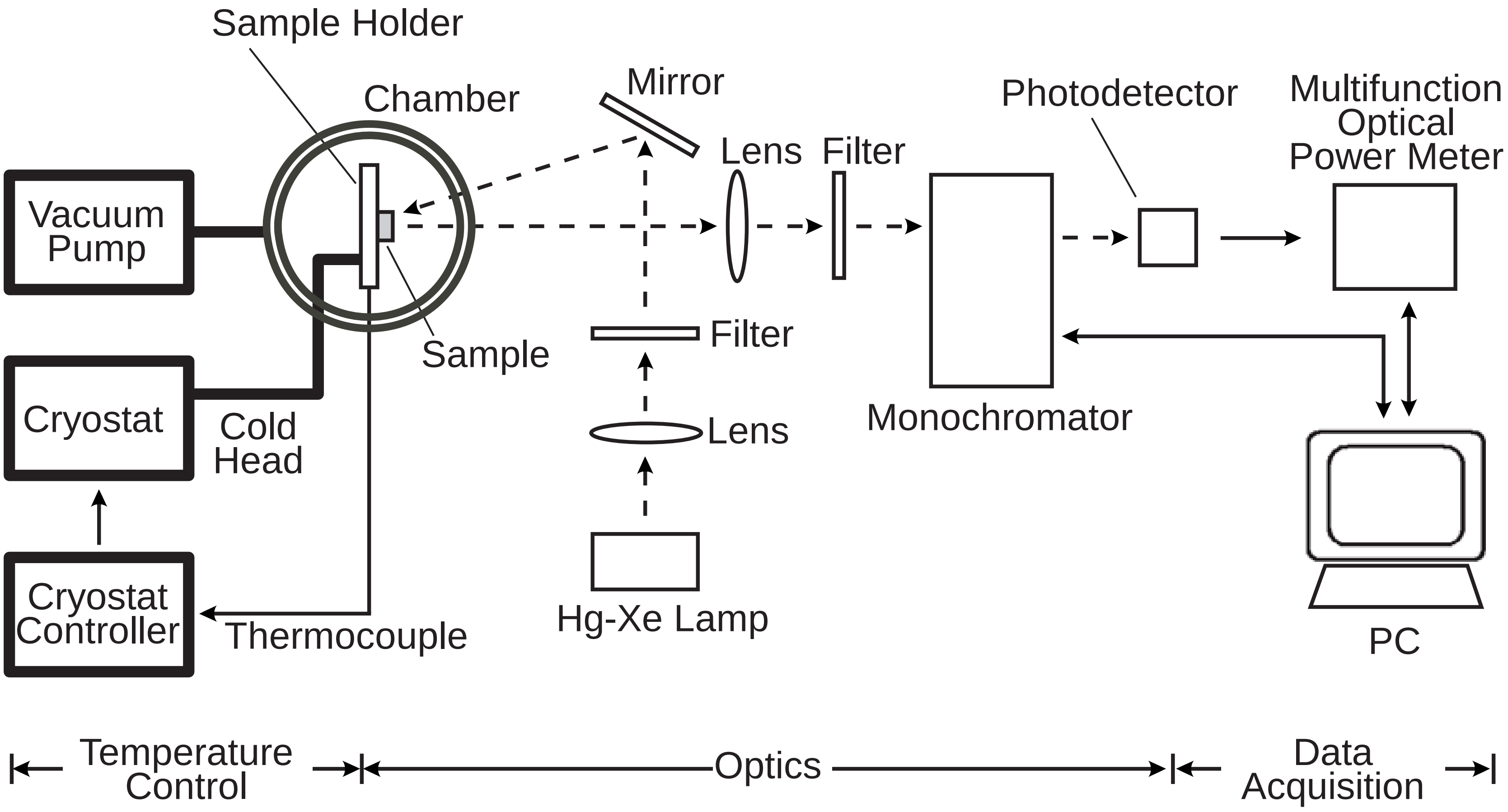

Figure 3.11: A schematic diagram of a photoluminescence experiment setup.

todetector improves the signal-to-noise ratio. It should be noted that another optical filter was placed in front of the monochromator. This is to remove reflected UV light from the sample and sample holder, so only the light emission from the sample enters in the monochromator (otherwise higher orders of dispersed UV light may overlap an optical region of our interest).

The light signal of each wavelength component was acquired and then stored on the computer. Light at a desired wavelength was converted to an electric signal by the photodetector. Then, the electric signal was read out by a multifunction optical power meter (Spectra-Physics model 70310), and the data are stored on the computer. By rotating the diffraction grating, the emission spectrum from the sample was acquired in the range of interest. All the controls required for the data acquisition and diffraction grating control were done using Laboratory Virtual Instrumentation Engineering Workbench (LabVIEW).

The sample was cooled and the temperature was controlled by the temperature control part for photoluminescence measurement as a function of temperature. The cooling was done by a closed cycle He cryostat system. The system mainly consists of a closed cycle He RMC cryostat (22C CRYODYNE CRYOCOOLER), a compressor, and a cryostat controller. As shown in Figure 3.13 (a), the sample was firmly held by the sample holder, which is in contact with the cold head of the cryostat through sapphire bars. Before cooling, the sample was kept in a sealed chamber shown in Figure 3.14 (e), and then the chamber was evacuated by using a mechanical pump (BOC EDWARDS, E2M0.7 Rotary Vacuum Pump) 0.1 torr. The temperature was monitored by a Omega CYD211 temperature monitor shown in Figure 3.13 (b). This system enables us to cool the sample down to 12 K. With this temperature control, the photoluminescence spectra were recorded in the same way as at room temperature.

Figure 3.12: The work station for photoluminescence experiments.

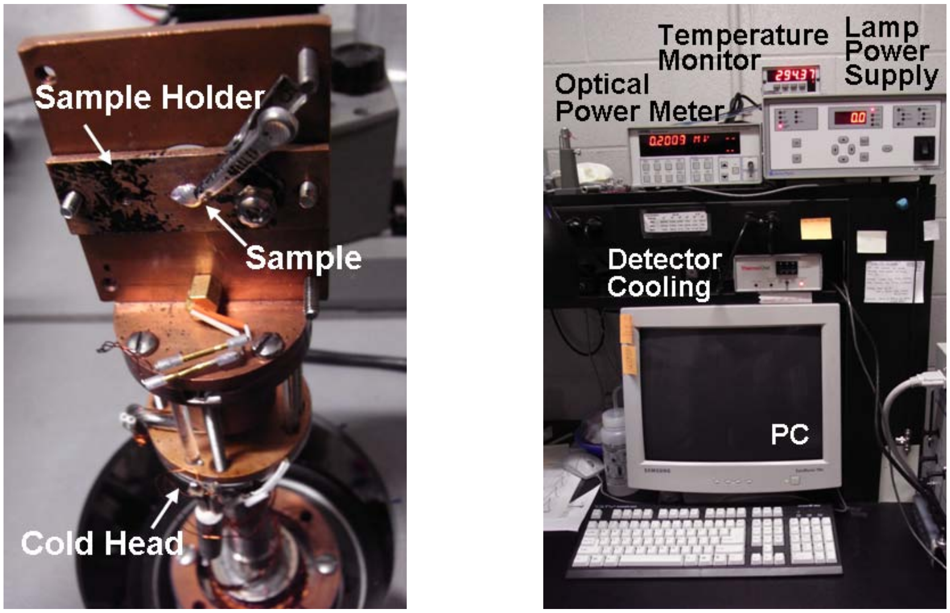

(a) (b)

Figure 3.13: Equipment used for the photoluminescence experiments: (a) shows a sample, sample holder, and cold head of a cryostat, and (b) shows temperature monitor, lamp power supply, multifunction optical power meter, photo detector cooling unit, and data acquisition PC.

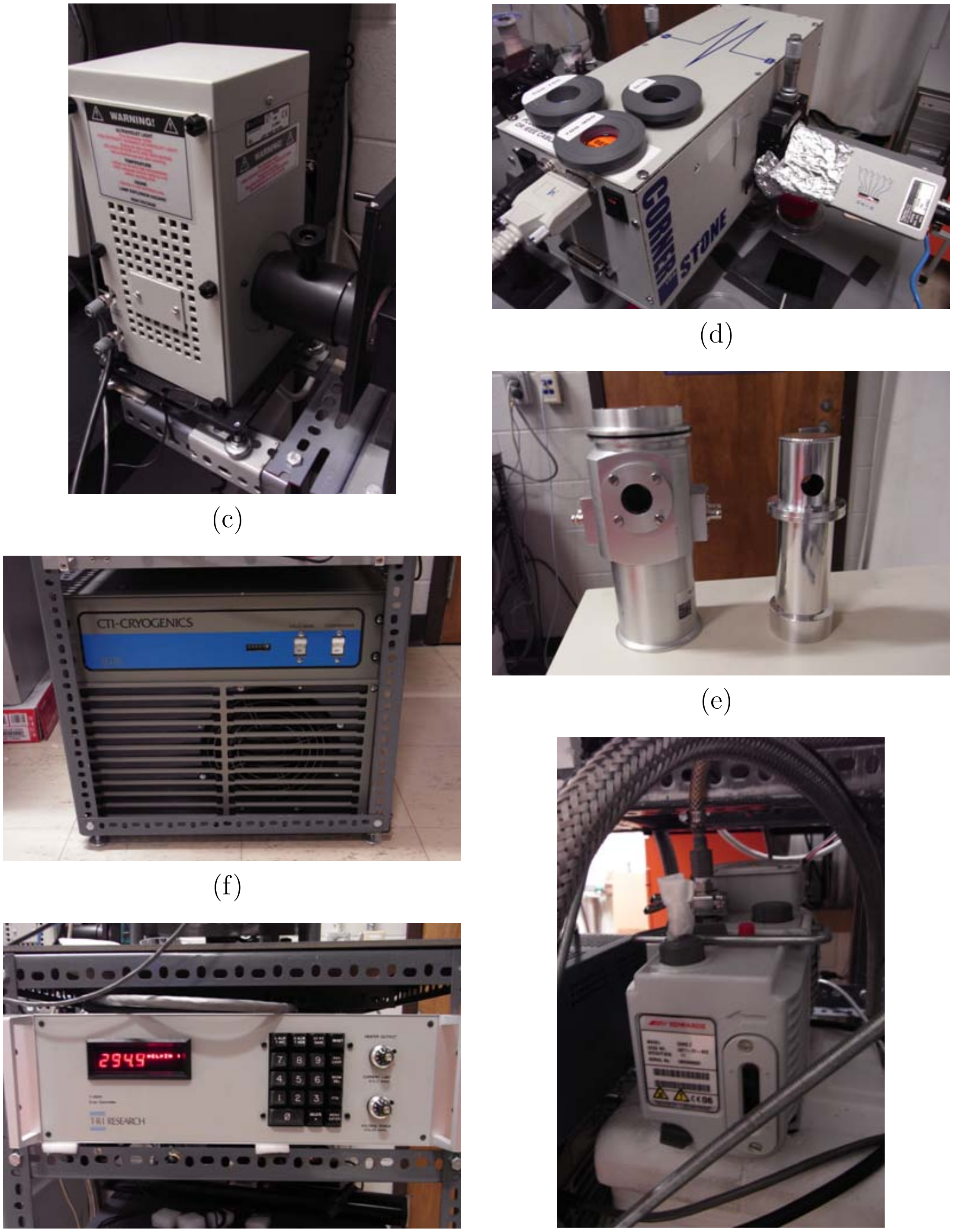

(c) (d) (e) (f) (g) (h)

Figure 3.14: Equipment used for the photoluminescence experiments (Continued): (c) Hg-Xe lamp unit, (d) monochromator (left), photodetector unit (right), and optical filters on top of the monochromator, (e) chamber (left) and inner shell (right), (f) compressor, (g) cryostat controller, and (h) vacuum pump.

3.7 X-ray Irradiation

Rare-earth doped ZBLAN based glass-ceramics are of great interest for X-ray imaging scintillator applications. Therefore, X-ray scintillation of our samples was tested in this work. This section discusses the experimental setup for such measurements.

The experimental setup as illustrated in Figure 3.15 was used to examine X-ray scintillation properties of our samples. Photographs in Fiugre 3.17 and Figure 3.18 show the equipment used in the experiment.

A standard GENDEX GX-1000 dental unit was used as an X-ray source. The X-ray tube was operated in the pulse regime at 90 kV by an X-ray controller. The X-ray tube has a tungsten anode, and the sample was irradiated through a 2.7 mm aluminum filter. The resulting spectrum of X-ray irradiation is shown in Figure 3.16. The mean energy was 45.8 keV, and the spectrum was simulated at SIEMENS's website [63] based on the algorithms described in [64, 65, 66]. The X-ray radiation was kept inside lead shielding as shown in Figure 3.17 and 3.18. The optical fibre (silica Solarization Resistant fibre, 190 – 2200 nm, StellerNet. Inc.) was placed at the bottom of the sample to collect the scintillation light from the sample and to guide it to the spectrometer (EPP2000CXR, StellarNet. Inc.). The spectrometer uses a concave holographic grating as a dispersion element, and the dispersed light is detected by a cooled linear image sensor (ILX511, SONY). The collected signal was read out to the computer.

The X-ray irradiation and spectrometer are synchronized by a computer control. Also, the exposure time of both the X-ray irradiation and the photodetector was controlled by the computer. As seen in Figure 3.17, a lamp mounted on the shielding indicates that the X-ray system is activated. This measurement system covers the wavelength range approximately from 300 nm to 1000 nm with a spectral resolution of approximately 0.5 nm.

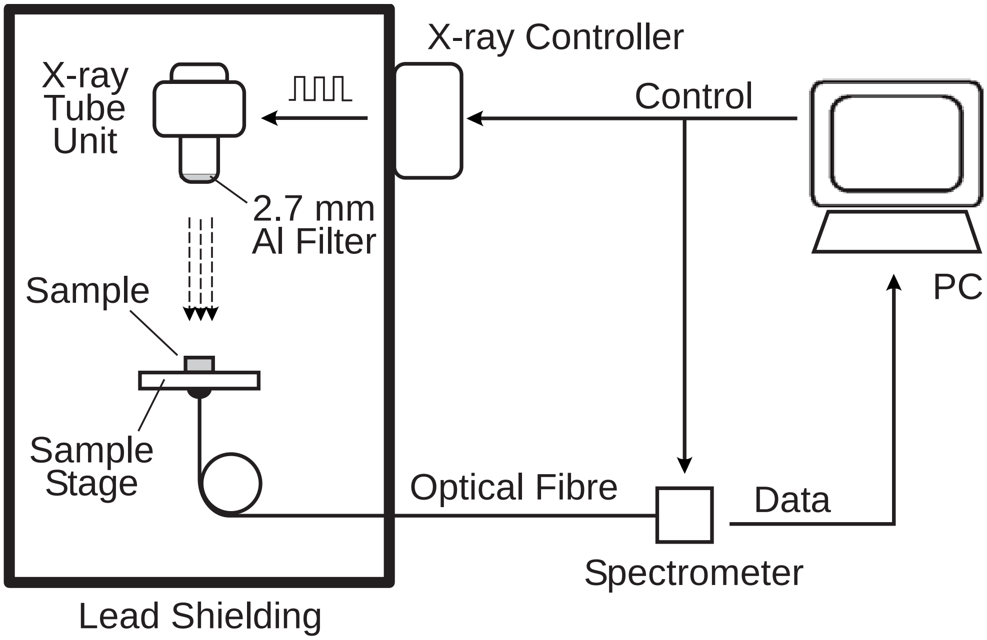

Figure 3.15: A schematic diagram of X-ray luminescence experiment setup.

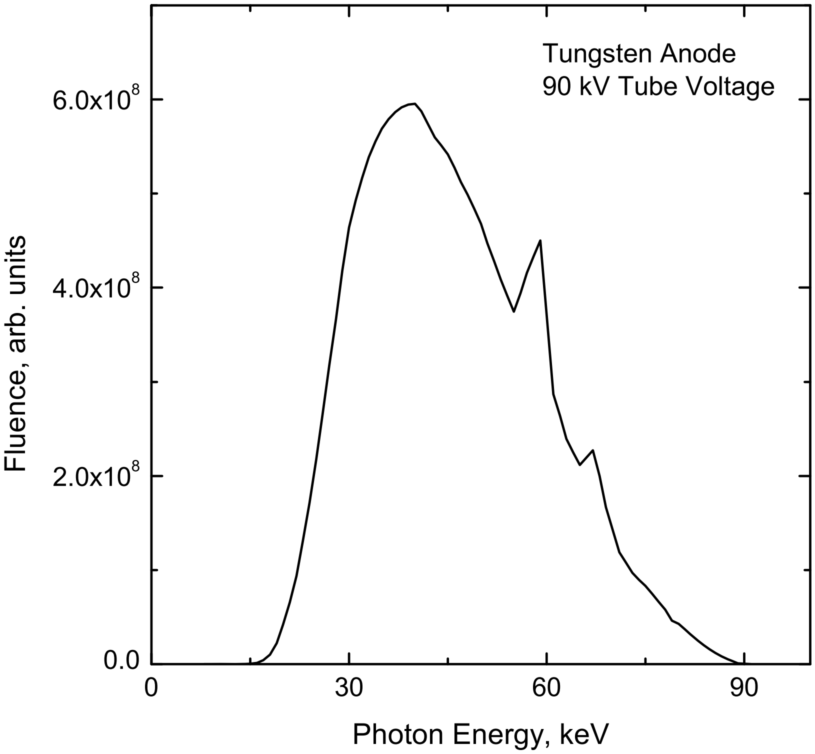

Figure 3.16: Irradiation spectrum of the X-ray tube with 90 kV, tungsten anode, and 2.7 mm Al filtration. The data were calculated with [63, 64, 65, 66].

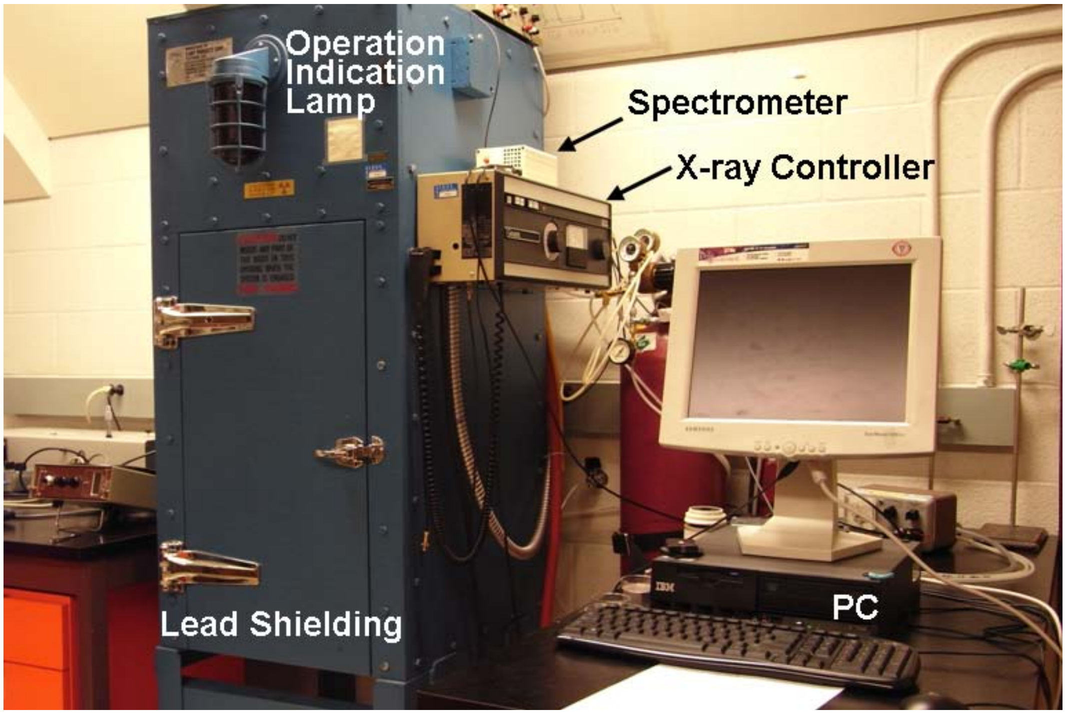

Figure 3.17: The work station for X-ray luminescence measurements.

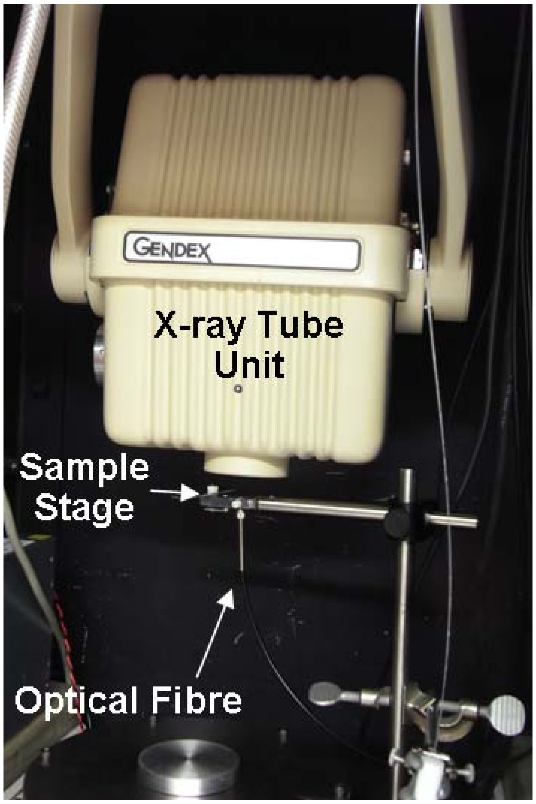

Figure 3.18: Inside of the lead shielding.

Chapter 4

Results and Discussion

Fluorochlorozirconate (FCZ) glasses doped with 1 % Sm have been prepared with diffrent concentrations of reducing agent (0.05, 0.1, 0.25, 0.35, and 1 molar %). The samples were further annealed under different conditions in terms of the temperature, time, and atmosphere to obtain glass-ceramics, glasses containing nanocrystals. This chapter reports and discusses valency conversion in Sm-doped FCZ glass-ceramics, annealing effects, photoluminescence characterization, and X-ray induced luminescence.

4.1 As-Prepared Glass Samples

This section will discuss glass samples which were prepared as explained in Section 3.1 (as-prepared glass samples). First, the visual appearance and transparency of the samples with different concentrations of reducing agent will be mentioned. Next, we will discuss valency reduction of the samarium ions in FCZ glasses.

4.1.1 Visual Appearance and Optical Transparency

Fluorochlorozirconate (FCZ) glass samples had been prepared as described in Section 3.1. A photograph of as-prepared glass samples is shown in Figure 4.1. The thicknesses of samples are comparable (0.3 – 0.5 mm). They are tinted red to a degree depending on the quantity of reducing agent added. This is typical for samples doped with divalent samarium ion due to its strong absorption in the UV-blue region.

Also, dark spots were observed in the glasses with higher concentrations of added reducing agent. This is attributed to localized reduction of Zr^{4+} to lower valence states, which is known to darken fluorozirconate glasses [67, 68]. All the samples are relatively transparent to the eye but with increasing red tint in samples with higher reducing agent.

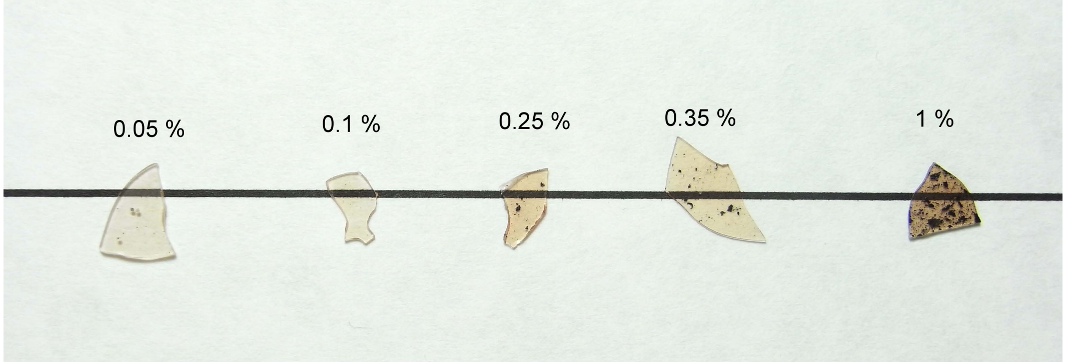

Figure 4.1: As-prepared glass samples with different amounts of reducing agent added. The indicated percentages are in molar %.

Figure 4.2 shows an optical transmission spectrum of an as-prepared glass sample which contains 1% of Sm ions and 0.1 % of reducing agent and that of a pure FCZ glass sample. The sample thicknesses are 0.5 mm. The spectra were recorded as described in Section 3.5.2 at room temperature. The pure FCZ glass showed excellent transparency in both the UV to NIR region of spectrum; while, the FCZ glass with Sm ions and reducing agent showed a lack of transparency in the UV-blue region (300 – 500 nm) and in the infrared region (1100 – 1600 nm) due to optical absorption by Sm^{2+} and Sm^{3+} ions, respectively (the optical absorption is discussed in more detail in Sections 4.1.2 and 4.2.4). However, high optical transmission (> 80 %) was overall observed in the region around 650 – 700 nm, in which the fluorescence is expected from our samples. It is very important for scintillator applications to have a high transparency to the emission light as described earlier (see Section 2.2.3).

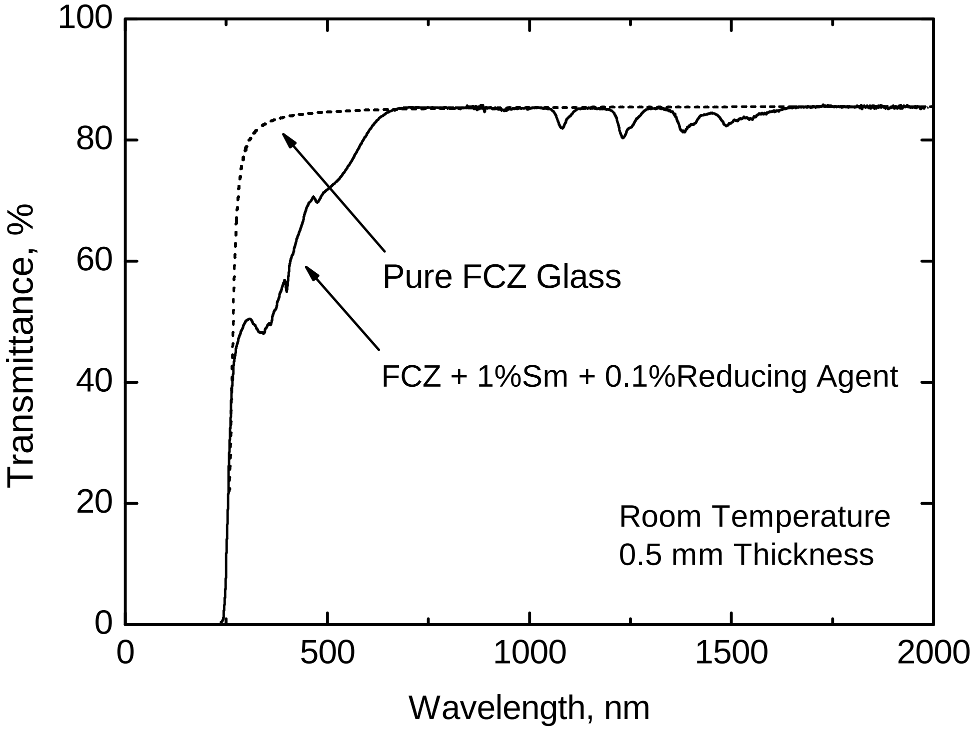

Figure 4.2: Optical transmission spectrum samples. The solid curve is for an as-prepared FCZ glass sample with 0.1 % of reducing agent added; while, the dashed curve is for a pure FCZ glass sample which does not contain luminescent ions and reducing agent. The thicknesses of samples are 0.5 mm, and the data were recorded at room temperature.

4.1.2 Valency Reduction

Doping divalent samarium is not straightforward since the divalent chloride and fluoride are not commercially available, which would be needed to maintain the FCZ composition. We, therefore, initially doped the FCZ glass with trivalent samarium and then added a common reducing agent, $NaBH_4$, to reduce the trivalent to divalent state. In this work, optical absorption experiments were carried out to investigate the valency reduction since optical absorption by the Sm^{3+} and Sm^{2+} ions is well known to be typically located in the infrared and UV-blue regions, respectively.

Figure 4.3 shows the absorption coefficients of as-prepared glasses with the same concentration of samarium (1 %) but different quantities of reducing agent that was added (0.05, 0.1, 0.25, 0.35, and 1 %). The spectra were recorded at room temperature ($\sim$ 23 °C). The spectra mainly consist of two parts; a single broad band with small peaks centering around 360 nm and a set of four peaks in the infrared region. The former is attributed to optical absorption by the Sm^{2+} and the latter by the Sm^{3+}. The observation of absorption by Sm^{2+} means that Sm^{2+} ions must exist in our sample, hence we have successfully reduced trivalent samarium to the divalent state by adding $NaBH_4$ as a reducing agent.

Figure 4.4 shows a correlation between the integrated optical absorption by the divalent ions and the fraction of added reducing agent. Increasing the fraction of the reducing agent increased the absorption intensity due to the divalent samarium ions. In other words, we had more Sm^{2+} ions as we add more reducing agent. However, this was only true when the reducing agent concentration was less than approximately 0.35 %. The reduction process was not effective for futher additions of the reducing agent.

Despite our observation of valency reduction and an increase in divalent samarium with the quantity of added reducing agent, the optical absorption by the trivalent

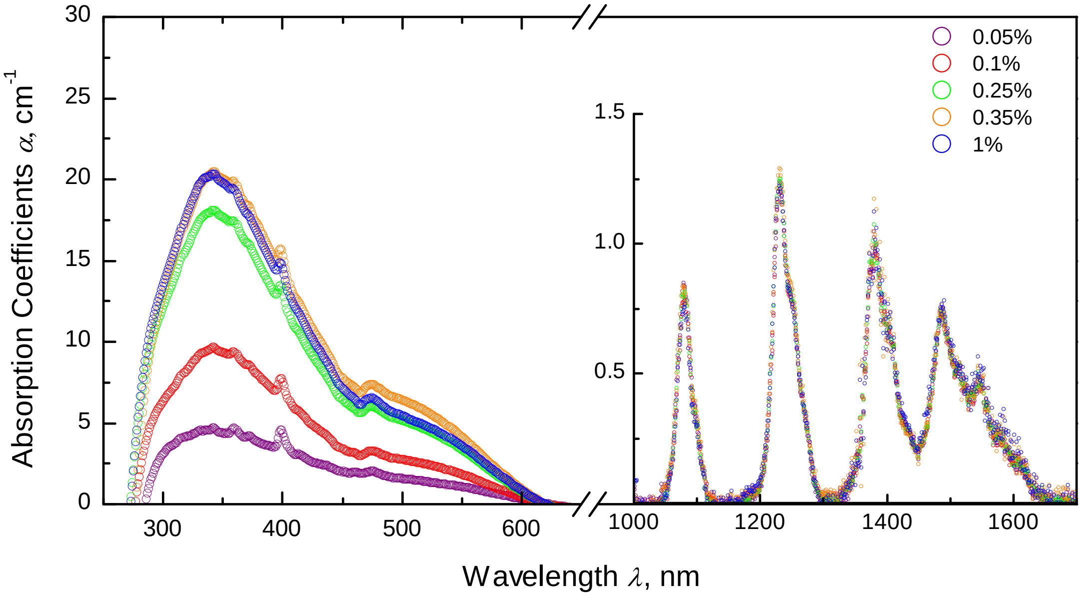

Figure 4.3: Absorption coefficient spectra of as-prepared glass samples with different quantities of reducing agent added (see also [67]).

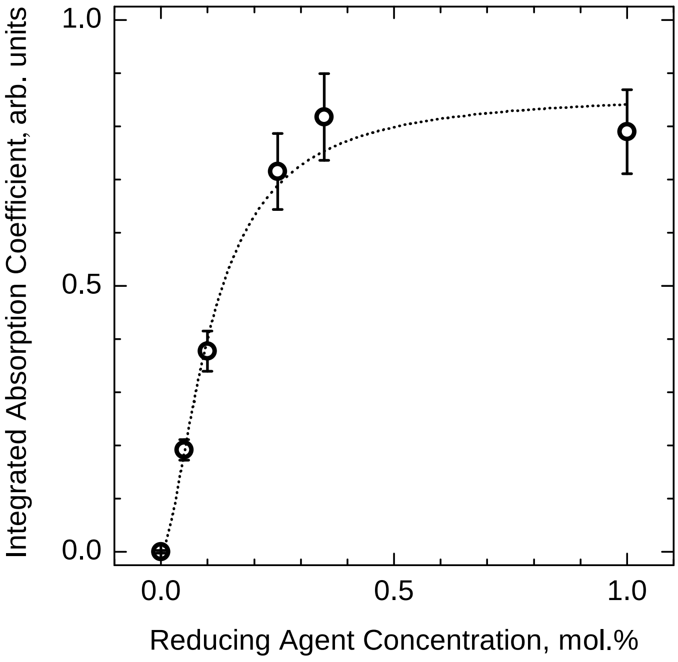

Figure 4.4: A correlation between the integrated optical absorptions by the divalent ions and the fraction of added reducing agent. The line is drawn to guide the eye (see also [67]).

samarium essentially remained the same regardless of the amount of the reducing agent added as seen in Figure 4.4. This explains that only a small fraction of trivalent ions have been reduced into the divalent state. The efficiency of the reduction process has been estimated from the following relationship called the Smakula's formula:

$$\int k(E)dE = N_i \left(\frac{e^2 h}{4\varepsilon_o nmc}\right)\left(\frac{n^2+2}{3}\right)^2 f_{ij} \tag{4.1}$$

where $k(E)$ is the absorption coefficient, n is refractive index, N_i is ion density, f_{ij} is oscillator strength, and the other symbols have their usual meaning. A value of 0.04 was used for the oscillator strength, which was calculated by Biémont et al. [69]. The calculation suggested that only 0.3 % of the trivalent ions at most had been converted to the divalent state.

4.2 Glass-Ceramics — Effects of Heat Treatment

It has been observed that a FCZ glass-ceramic contains $BaCl_2$ nanocrystals. Earlier studies [29, 30, 31] showed the fact that in FCZ glass-ceramics, the crystal structure, either the hexagonal or the orthorhombic phases, and size of embedded nanocrystals vary depending upon the heat treatment conditions. Effects of heat treatment have been investigated on our samples throughout this work by numerous experiments including differential scanning calorimetry, X-ray diffraction, optical absorption, photoluminescence, and X-ray induced luminescence. This section presents results of the experiments and discusses effects of heat treatments on our samples.

4.2.1 Differential Scanning Calorimetry (DSC)

Figure 4.5 compares DSC thermograms recorded for an as-prepared glass sample and glass-ceramic sample annealed at 250 °C for 5 min in a N_2 gas. Both the samples contain 0.25 % of reducing agent.

For the as-prepared sample, we found that the glass transition tempere was approximately 210 °C, which is followed by the first exothermic crystallization peak around 240 °C. We attribute this to the nucleation and growth of hexagonal phase barium cloride ($BaCl_2$) crystals (the determination of crystal structure was supported by X-ray diffraction studies, which is shown in Section 4.2.3). At higher temperatures, there are three very close exothermic peaks, located around 295, 310, and 320 °C. These exothermic peaks correspond to the crystallization of the host glass.

These DSC scans suggest that annealing a sample in the temperature range (225 – 270 °C) enables us to obtain $BaCl_2$ nanocrystals while the FCZ glass structure is maintained as a host matrix. As expected, the DSC data for the annealed sample (Figure 4.5) showed that the first crystallization peak was removed while the other crystallization peaks appeared as seen for the glass sample. Based on these results, we have chosen annealing conditions that correspond to heat treatments in the temperature range 225 – 270 °C.

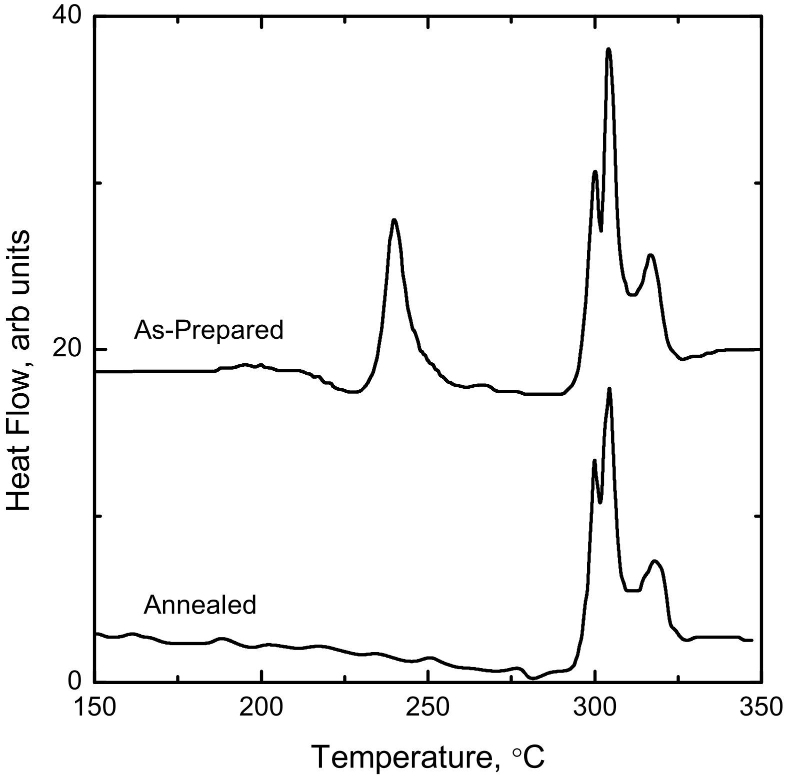

Figure 4.5: DSC data recorded for as-prepared and annealed FCZ samples containing 1 % Sm^{3+} ions and 0.25 % of $NaBH_4$ as a reducing agent. The heating rate was 10 K/min. The annealing conditions were: 250 °C, 5 min, N_2. (See also [67].)

4.2.2 Appearance

Figure 4.6 compares two glass-ceramic samples annealed under different conditions; (left) 245 °C for 5 min and (right) 270 °C for 30 min in a nitrogen atmosphere. Both samples contain 0.25 % of reducing agent. The left sample has an excellent transparency. While the other sample is still transparent but slightly milky, which is due to the crystallization of the FCZ glass matrix.

Figure 4.7 illustrates optical transmission spectra recorded on a sample before and after heat treatment at 238 °C for 5 min in a nitrogen atmosphere. The sample contains 0.35 % of reducing agent and the thickness is 0.3 mm. The spectra were recorded as described in Section 3.5.2 at room temperature. As seen in the graph, even after the annealing, the excellent transparency over the range of interest ($>\sim$ 600 nm) was maintained. This explains that our glass-ceramic samples can be maintained as transparent as the as-prepared glasses under appropriate heat treatment conditions (though further studies are required for the optimization of heat treatment, which is not our present interest).

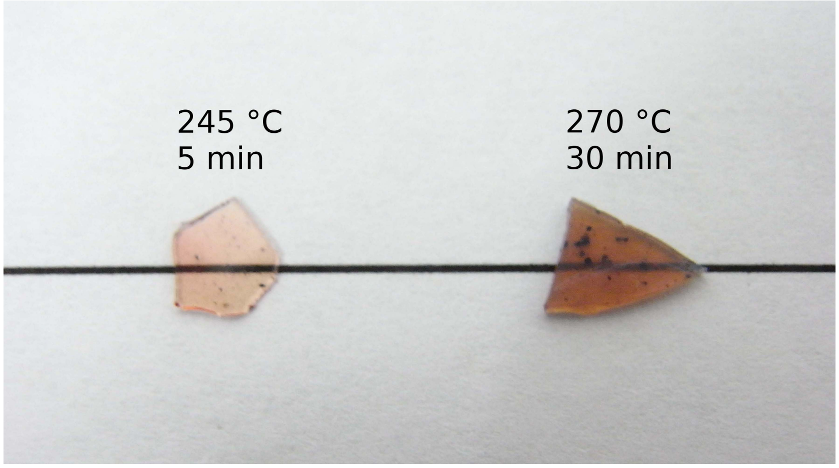

Figure 4.6: An example of annealed samples. The annealing conditions were: (left) 245 °C for 5 min and (right) 270 °C for 30 min in a nitrogen atmosphere.

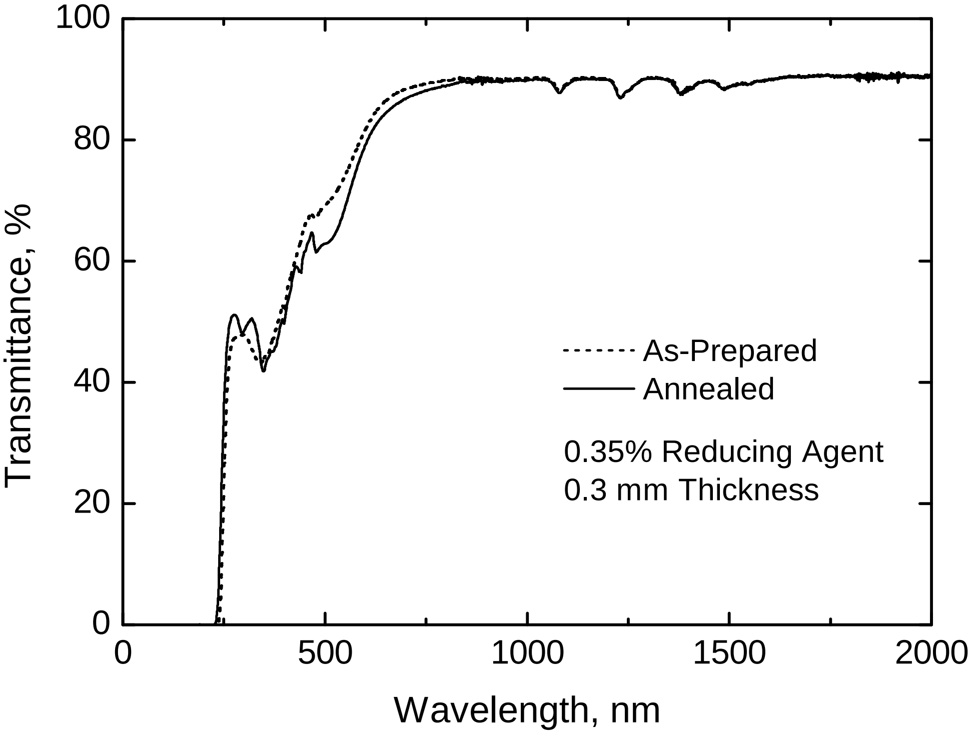

Figure 4.7: Optical transmission spectra of as-prepared glass (before annealing) and glass-ceramic (after annealing) samples. The annealing conditions are: 238 °C for 5 min in a nitrogen atmosphere. The samples contains 0.35 % of reducing agent and the data was recorded at room temperature.

4.2.3 Crystallographic Analysis

Earlier works [29, 30, 31] reported the formation and characteristics of $BaCl_2$ nanocrystals in rare-earth doped FCZ glass-ceramics. In this work, powder X-ray diffraction (XRD) was carried out on our as-prepared samples and also annealed samples under different conditions in order to study the heat treatment effects on the crystal structure and size of expected $BaCl_2$ nanocrystals.

Figure 4.8 shows examples of X-ray diffraction data recorded on: (a) an as-prepared sample, and samples (b) annealed at 238 °C for 5 min in a N_2 atmosphere, (c) annealed at 270 min for 30 °C in N_2. XRD patterns of the orthorhombic and hexagonal phases of $BaCl_2$ crystal are also illustrated as references. The patterns have been compared from PDF 24-0094 and PDF 45-1313 powder pattern standards, respectively.

The X-ray diffraction data of the as-prepared sample in Figure 4.8 (a) shows only broad peaks. This pattern is typical for a noncrystalline material [70]. Upon annealing, additional sharp peaks appear. They are attributed to (b) the hexagonal and (c) the orthorhombic phases of barium chloride by comparing the experimental XRD data with the reference X-ray diffraction patterns [67]. Since the sample remained transparent, seen in Figure 4.6 (left), it is suggested that small size $BaCl_2$ crystals have grown upon annealing, while the glass matrix has not crystallized. The crystal sizes were estimated by using the well-known Sherrer formula [70]:

$$< L >= \frac{K\lambda}{\beta \cos\theta} \tag{4.2}$$

where $< L >$ is the average crystallite size, K is a shape factor, λ is the X-ray wavelength, β is the line broadening (FWHM) in radians, and θ is the Bragg angle. For our calculations, the constant K was taken as unity, and the formula was applied to the $< 021 >$ and $< 211 >$ reflections for the hexagonal and orthorhombic nanocrystallites, respectively. We assumed the peaks to have either Gaussian or

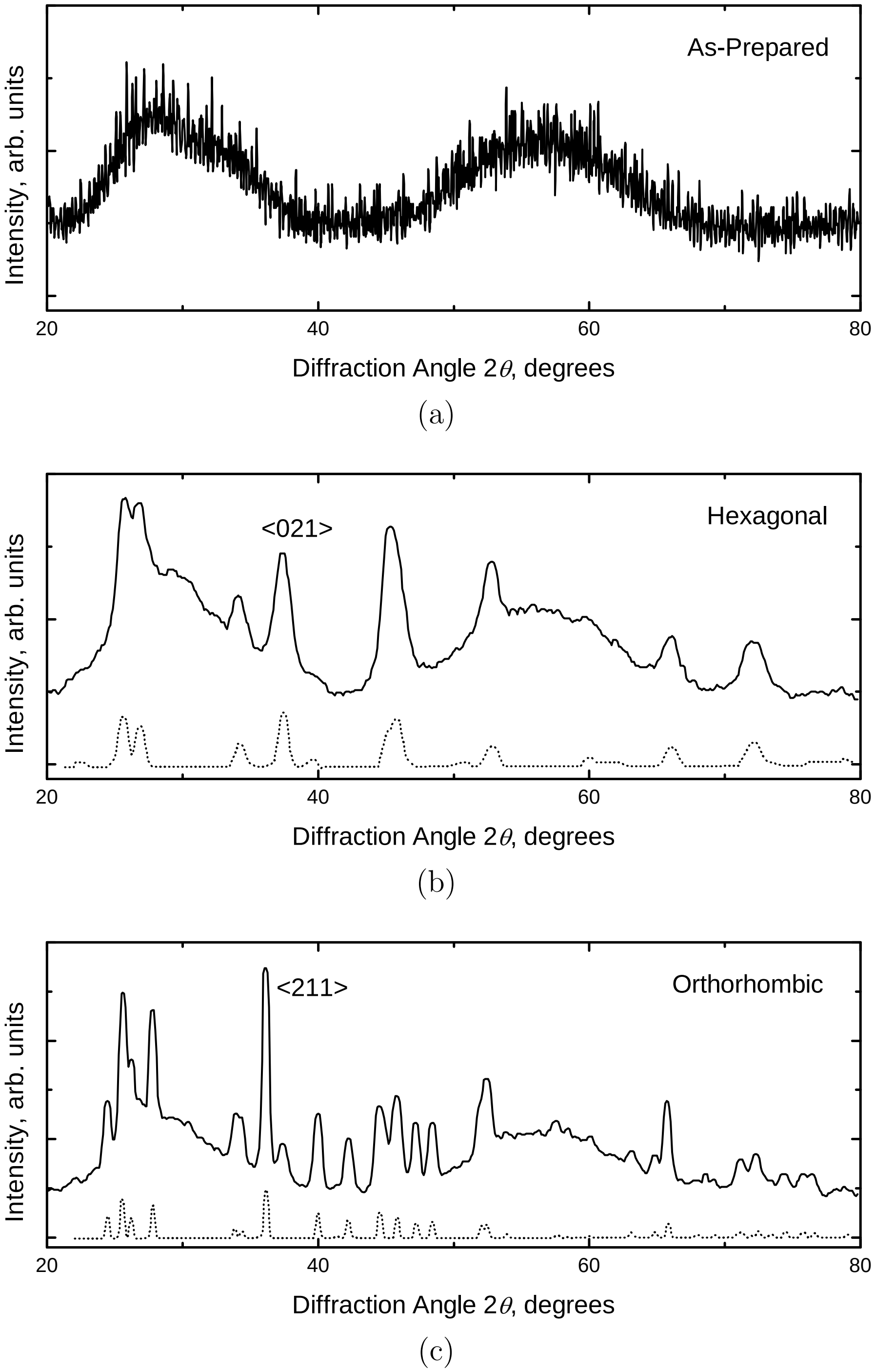

(a)

(b)

(c)

Figure 4.8: X-ray diffraction patterns of (a) an as-prepared sample and annealed samples (b) at 238 °C for 5 min and (c) at 270 °C for 30 min in a nitrogen gas. The dotted patterns in the bottom of (b) and (c) correspond to the hexagonal and the orthorhombic $BaCl_2$ based on PDF 24-0094 and PDF45-1313, respectively. (See also [67].)

Lorentzian line shapes and then obtained two broadening parameters β that were averaged. The average β was used in Equation 4.2 to calculate $< L >$. As a result, the averaged crystal sizes were estimated to be 19 and 54 nm for the samples (b) and (c), respectively.

Just like other types of FCZ glass-ceramics with different rare-earth ions reported earlier, our samples also showed the same tendency of nanocrystal growth. From our observations from 15 samples with different annealing histories, typically shorter time at lower temperature annealing tends to give the hexagonal phase, while longer time at higher temperature annealing tends to result in the orthorhombic phase.

4.2.4 Optical Absorption

We have measured optical absorption spectra for our samples before (as-prepared glass) and after (glass-ceramic) heat treatment. Figure 4.9 compares optical densities (fractional transmittance of light,$-\ln(I/I_o)$) of a sample before and after annealing with 0.25 % of reducing agent added and also divalent samarium doped $BaCl_2$ single crystal. The sample was annealed at 238 °C for 5 min in a nitrogen atmosphere. The data for $BaCl_2$ single crystal were extracted from the work of Lauer and Fong [53]. Compared to the spectrum of the as-prepared sample, the annealed samples showed additonal distinct peaks. The peaks clearly agree with the absorption spectra of Sm^{2+} in $BaCl_2$ single crystals. This similarity suggests that the reduced Sm^{2+} ions have been embedded in the $BaCl_2$ nanocrystals. It is instructive to mention that the radii of Ba and Sm^{2+} ions are very close (1.30 and 1.32 Å, respectively). So, there is very high probability that Sm^{2+} ions can substitute for Ba ions.

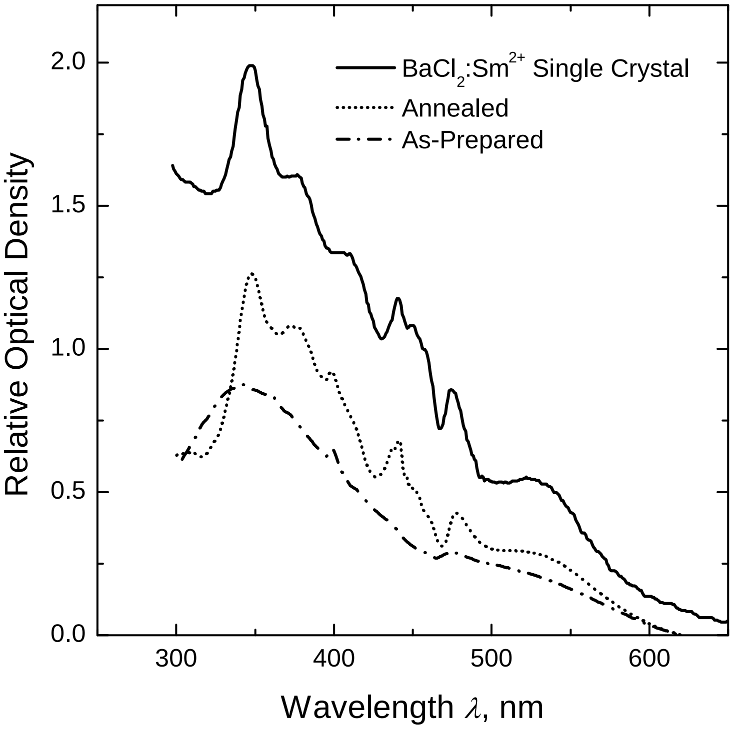

Figure 4.9: Relative optical densities of a Sm doped FCZ glass and glass-ceramic with 0.25 % reducing agent added and of a single crystal (orthorhombic phase) $BaCl_2$ doped with Sm^{2+} (see also [67]).

4.2.5 Fluorescence

In this work, as-prepared glass samples and annealed samples were excited by ultraviolet light and also by X-rays, and the resulting fluorescence were measured and studied. The experimental details are described in Sections 3.6 and 3.7. It is expected that samarium ions in the divalent state (Sm^{2+}) would show a strong red emission due to the allowed 5d-4f transitions.

The photoluminescence experiment was carried out on as-prepared and annealed samples with 0.25 % of reducing agent. The annealing conditions are at 270 °C for 30 min in a nitrogen gas. Figure 4.10 shows an example of samples illuminated under ultraviolet excitation. Although we have confirmed the existence of samarium ions in both the divalent and trivalent states, no photoluminescence from divalent samarium ions was seen from as-prepared samples. However, the heat treated samples showed a bright red fluorescence emission. This appearance of fluorescence upon annealing was observed in samples with different quantities of reducing agent added and with different heat treatment histories.

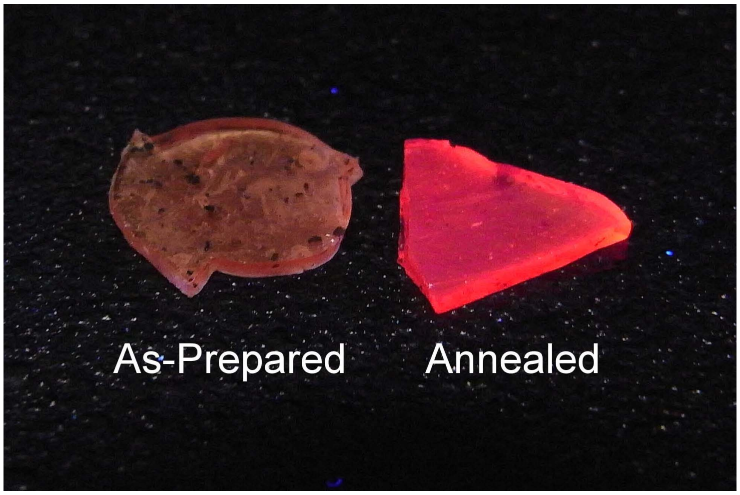

Figure 4.10: An example of as-prepared and annealed samples under ultraviolet excitation. The annealing conditions were 270°C for 30 min in a nitrogen atmosphere.

Figure 4.11 compares photoluminescence spectra of samples before and after annealing. Both samples contain 0.25 % of reducing agent, and one of the samples was annealed at 270 °C for 30 min in a nitrogen gas. The spectra were recorded at room tempeature. Although it was not visually observed, the data showed very weak emission from the as-prepared sample. From the spectrographic positions of the peaks, we attribute the origin of the emission to Sm^{3+}, which remained unreduced during the preparation process. This is interesting because we know, from the optical absorption spectra, that Sm^{2+} ions exist in the sample. Upon heat treatment, the sample shows much stronger fluorescence as also seen in Figure 4.10. The spectrum consists of a number of sharp peaks and two broad bands around 700 nm and 900 nm. This spectral structure is typical for samples activated with divalent samarium ions. (The expected Sm^{2+} lines are indicated at the top of Figure 4.11). We, therefore, attribute the sharp peaks to the 4f-4f transitions and the broad band $\sim$ 700 nm to the 5d-4f transition of the reduced Sm^{2+} ions. It is worth pointing out that the PL spectrum of the annealed sample also contains fluorescence by Sm^{3+} ions. Despite the fact that the concentration of Sm^{2+} is much lower than that of Sm^{3+}, the fluorescence intensity by Sm^{2+} is much stronger than that of Sm^{3+}.

Similar effects have been observed in X-ray induced luminescence (XL) spectra shown in Figure 4.12. The dotted curve refers to an XL spectrum of an as-prepared sample, while an XL spectrum corresponding to an annealed sample is shown as a solid curve. The sample was annealed at 270 °C for 30 min in a gas mixture of 5 % H_2 and 95 % Ar. The both samples contain 0.25 % of reducing agent. As in the case of photoluminescence above, the as-prepared sample showed only weak X-ray fluorescence by Sm^{3+}, and in addition much stronger fluorescence by Sm^{2+} was observerd from the annealed sample. The sharp peaks and the broad band are attributed to 4f-4f and 5d-4f transitions, respectively. Despite the much lower fraction of Sm^{2+} with respect to that of Sm^{3+} (0.3 %), much stronger fluorescence have been observed in both photoluminescence and X-ray induced luminescence (approximately 8 times stronger for XL).

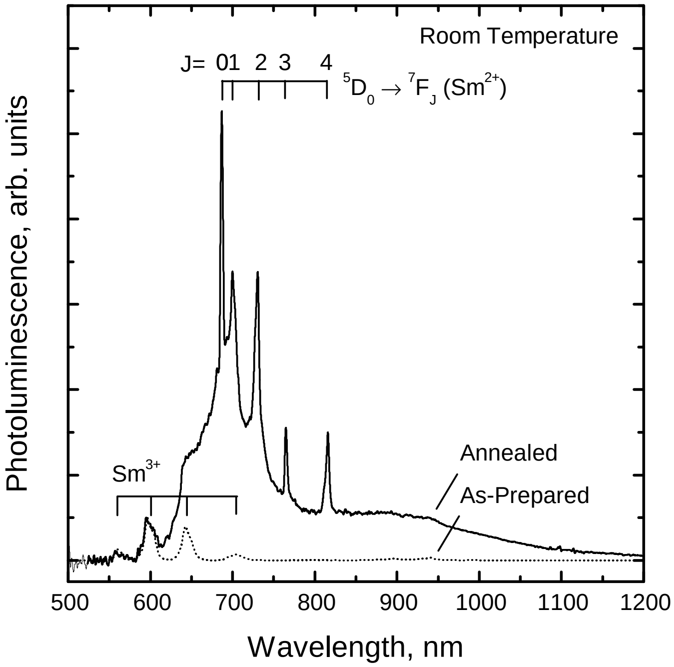

Figure 4.11: Photoluminescence spectra recorded at room temperature for samples with 0.25 % of added reducing agent $NaBH_4$ before and after annealing at 270 °C for 30 min in a nitrogen gas.

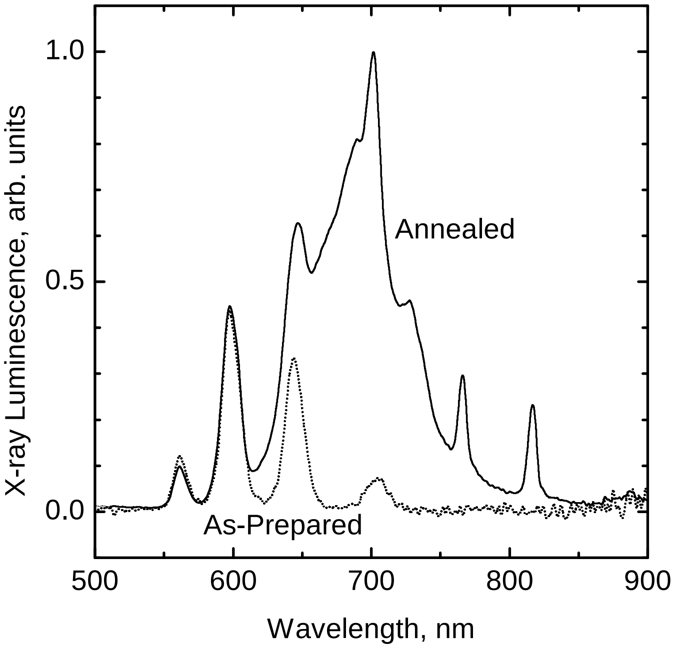

Figure 4.12: X-ray luminescence spectra before and after annealing sample with 0.1 % of reducing agent added. The spectra were recorded at room temperature. Annealing conditions were: 270 °C for 30 min in a mixture of hydrogen and argon gases.

4.2.6 Summary

Effects of heat treatment have been investigated comparing experimental results of samples before and after annealing.

As-prepared samples are glasses (from XRD) and appear to be highly transparent to the eye. The transparency depends on the heat treatment, that is, annealing temperature and time. X-ray diffraction measurements showed that suitable annealing would induce the nucleation and growth of $BaCl_2$ nanocrystals. The crystal structure is either hexagonal or orthorhombic depending on the heat treatment conditions. The size of nanocrystals varies depending on the heat treatment conditions as well. Typically higher annealing temperature and longer annealing times would result in larger nanocrystals to grow.

Optical absorption of as-prepared samples showed mainly a broad band. Upon annealing, additional peaks appeared in the absorption spectrum, which is in good agreement with that of a single crystal $BaCl_2$:Sm^{2+}. This similarity suggests that the reduced Sm^{2+} ions have been embedded in the $BaCl_2$ nanocrystals.

Luminescence from Sm^{2+} when induced by ultraviolet and X-ray was completely absent in as-prepared samples, and only fluorescence from Sm^{3+} ions was observed. However, annealed samples showed emissions from both the Sm^{3+} and Sm^{2+}, and the Sm^{2+} showed very strong fluorescence (~ 8 times that of Sm^{3+}) despite the fact that only a small fraction of the total Sm^{3+} ions had been converted (0.3 %).

From these results, it is suggested that as $BaCl_2$ nanocrystals grow upon heat treatment, and the reduced Sm^{2+} substitute for the barium ions in the $BaCl_2$ crystals. Fluorescence by Sm^{2+} is active only when embedded in the $BaCl_2$ nanocrystals. However, the fluorescence emission from Sm^{2+} is very efficient, and its intensity is much stronger than that of Sm^{3+}.

4.3 Photoluminescence Characterization

Photoemission by Sm^{2+} is highly efficient when embedded in the $BaCl_2$ nanocrystals. The crystal structure of the nanocrystals is either orthorhombic or hexagonal. It is worth to study the hexagonal $BaCl_2$ since it is metastable under common conditions and there is hardly any data on that. Moreover, the investigation of luminescence from the Sm^{2+} would be of a great interest because it would be a probe of the local environment of the ions. Photoluminescence (PL) experiments as a function of temperature were carried out on a number of samples with different annealing histories. The experimental details are described in Section 3.6.

4.3.1 Optical Transitions of FCZ:Sm^{2+}

PL spectra as a function of temperature have been investigated for three types of samples: FCZ glass-ceramics with (a) orthorhombic $BaCl_2$ nanocrystals, (b) hexagonal $BaCl_2$ nanocrystals, and (c) a mixture of orthorhombic and hexagonal $BaCl_2$ nanocrystals.

Figure 4.13 shows examples of photoluminescence spectra recorded at 12, 50, 100, 150, and 200 K for the three types of samples. The crystal structures were identified by using X-ray diffraction analysis as explained previously (Section 4.2.3). The sample that predominantly contains the orthorhombic $BaCl_2$ nanocrystals showed a very strong temperature dependence of photoluminescence. The transitions were from the excited $^5D_0$ state to the ^7F_J ($J = 0, 1, 2, \ldots$) multiplet ground levels above 100 K. For temperatures below 100 K, the dominant transitions were mainly from the $^5D_1$ level, and the intensities increased as the temperature dropped. While, the samples with hexagonal $BaCl_2$ nanocrystals showed consistent optical transitions over the whole temperature range; however, the intensity increased as the temperature decreased.

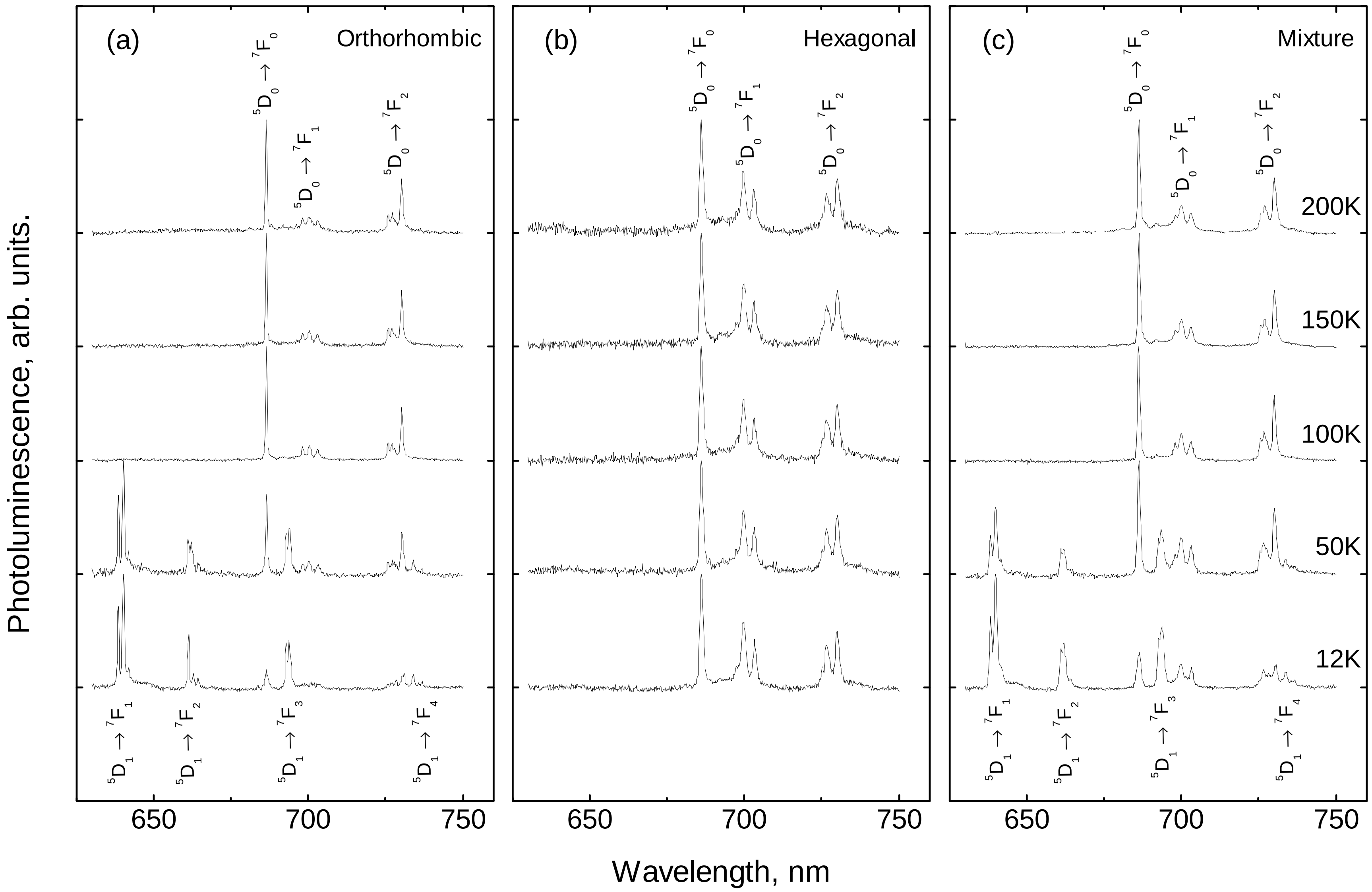

Figure 4.13: Photoluminescence spectra of three samples of FCZ glass doped with samarium as a function of temperature. The three spectra are characteristics of samples containing (a) predominantly the orthorhombic phase, (b) the hexagonal phase, and (c) a sample containing a mixture of the two phases (see also [67]).

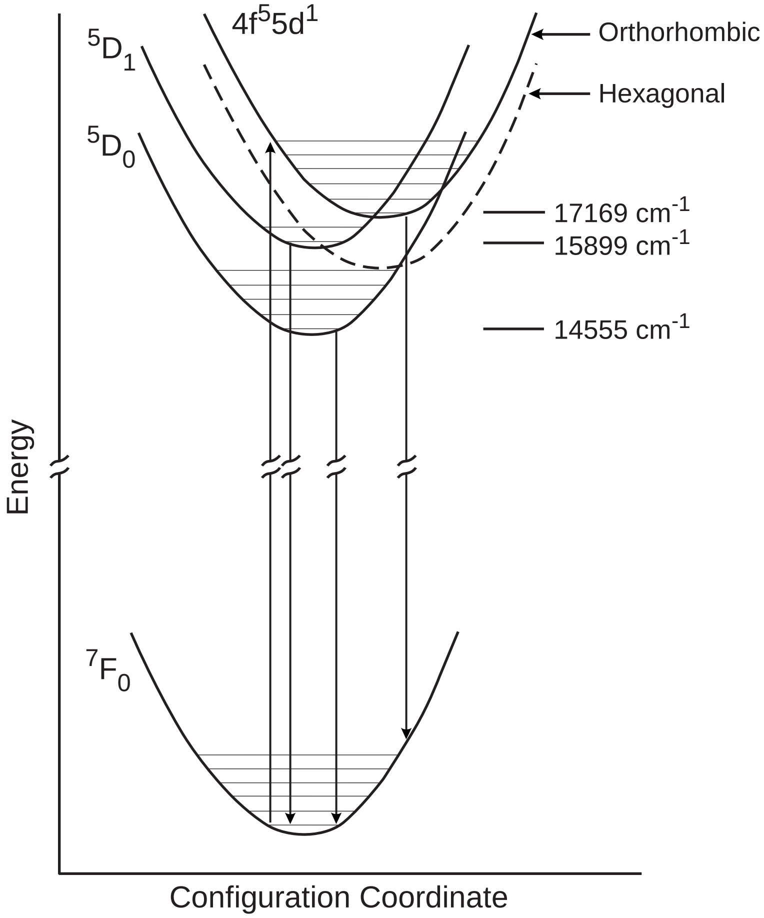

Figure 4.14: A schematic diagram of energy as configuration coordinate for a Sm^{2+} in the orthorhombic barium chloride structure, drawn approximately to scale based on the parameters deduced by Lauer and Fong [53] and by He et al.[71]. The dashed line shows the suggested relative position of the $4f^5 5d^1$ level for Sm^{2+} ions in hexagonal barium chloride (see also [67]).

This strong temperature dependence can be explained with the configuration-coordinate energy level diagram for a single crystal $BaCl_2$:Sm^{2+} (orthorhombic) as illustrated in Figure 4.14. The diagram was drawn to an approximate scale based on the works by Lauer and Fong [53], and by He et al. [71]. The $4f^5 5d^1$ level is typical for a divalent rare-earth ion. At low temperatures, excitation into the upper 5d states is followed by relaxation into the lowest 5d state. This level has a short life time, and hence a rapid non-radiative transition occurs into the lowest $^5D_1$ level. This results in the $^5D_1$ to ^7F_J transitions, observed in the lower part of Figure 4.13

(a). For the orthorhombic phase, the $4f^55d^1$ level lies about 1270 cm^{-1} above the $^5D_1$ level. At higher temperature, de-excitation into the $^5D_0$ level becomes possible through the $4f^55d^1$ level. This allows a non-radiative transition from $^5D_1$ to $^5D_0$ followed by $^5D_0$ to ^7F_J transitions. A transition from $4f^55d^1$ state into ^7F_J level is also possible, and this results in a broad band radiative emission evident in Figure 4.11. The very different temperature dependence for hexagonal barium chloride would be explained if the lowest $4f^55d^1$ level lies below the $^5D_1$ level as drawn with a dashed line in Figure 4.14. If it is the case, radiative transitions from the $^5D_0$ and $4f^55d^1$ states would be expected even at low temperatures as in our consistent observations. The $^5D_1$ to ^7F_J transitions would be either very weak or absent. For samples containing a mixture of the two phases, simply the characteristics of each phase is seen; at low temperatures, both transitions from $^5D_1$ and $^5D_0$ to ^7F_J are seen; while, only the $^5D_0$ to ^7F_J transitions appear at higher temperatures.

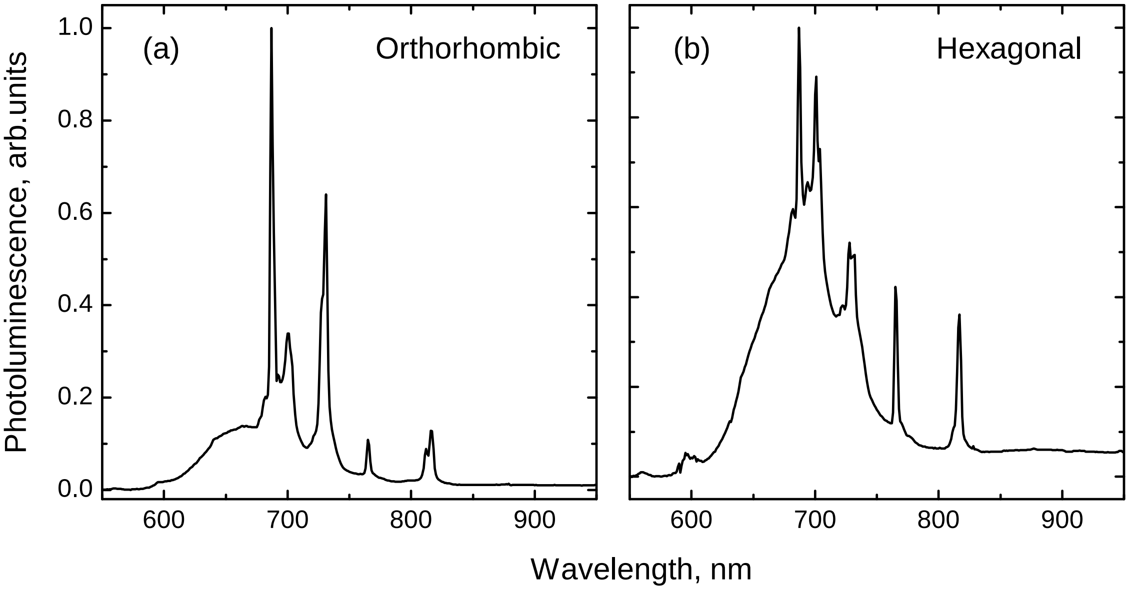

Figure 4.15: Photoluminescence spectra of samarium doped FCZ glass-ceramic samples predominately containing (a) the orthorhombic and (b) the hexagonal $BaCl_2$ phases. The spectra were recorded at room temperature and normalized to the peak emission intensities.

Figure 4.15 compares photoluminescence spectra of Sm^{2+} doped FCZ glass-ceramic samples: predominantly containing (a) the orthorhombic and (b) hexagonal $BaCl_2$ nanocrystals. The spectra were recorded in the visible and near infrared ranges at room temperature and then normalized to the peak emission intensity. As we can clearly see, the sharp 4f-4f transitions dominate in the orthorhombic $BaCl_2$, while the divalent samarium ions in the hexagonal $BaCl_2$ show mainly a broad and strong 5d-4f transition. This crystal structure dependence would be explained if you accept the assumption of the down shift of the $4f^5 5d^1$ level in the hexagonal $BaCl_2$:Sm^{2+} because, if so, the $4f^5 5d^1$ level would be more populated; as a result, the stronger 5d-4f transitions would occur.

Consequently, both the unique and strong temperature dependence and crystal structure dependence of photoluminescence are comfortably explained with the assumption that the bottom of the $4f^5 5d^1$ level shifts down to below the $^5D_1$ level. It is worth noting here that an effective down shift of the $4f^5 5d^1$ level was also observed when applying a high pressure onto a Sm^{2+} doped orthorhombic crystal [72].

4.3.2 Crystal Phase Identification

FCZ glass-ceramics contain $BaCl_2$ nanocrystals in either the orthorhombic or hexagonal structure depending on the heat treatment conditions. In some cases, both the orthorhombic and hexagonal phases coexist (mixture of phases) within the glass matrix.

As we discussed in the previous section, at low temperatures, photoluminescence spectra show only the $^5\mathrm{D}_1$ to $^7\mathrm{F}_J$ transitions for the hexagonal $BaCl_2$:Sm^{2+}. In the case of the orthorhombic phase, we observe $^5\mathrm{D}_0 \rightarrow {}^7\mathrm{F}_J$ emissions, and transitions from the $^5\mathrm{D}_1$ level are completely absent, or very weak. This change in transitions is attributed to the lowered position of the lowest $4\mathrm{f}^5 5\mathrm{d}^1$ level in the hexagonal phase with respect to that of the orthorhombic phase (Figure 4.14). For this reason, the prominent difference appearing in PL spectra may be used to identify the crystal structure of the embedded barium chloride nanocrystals, or content ratio of the crystal phase in the case of a mixture that contains the both phases. We therefore define a following "figure of merit":

$$C_{\mathrm{ortho}} = \frac{A(640)}{A(640) + A(687)} \times 100 \quad [\%] \tag{4.3}$$

where A(640) and A(687) are the relative intensities of $^5\mathrm{D}_1 \rightarrow {}^7\mathrm{F}_1$ and $^5\mathrm{D}_0 \rightarrow {}^7\mathrm{F}_0$ emissions both at low temperature, respectively. This parameter gives 100 % when orthorhombic $BaCl_2$ nanocrystals dominate in the glass-ceramic. While, it is 0 % in the opposite case in which the glass-ceramic predominantly contains the hexagonal $BaCl_2$. In the case of a mixture, the value lies between 0 – 100 %. This approach could be used as a convenient indicator of the relative concentration of the two crytal strucutures. However, it is instructive to note here that, for more accurate estimations of the concentrations, the unknown oscillator strengths for the corresponding transitions must be considered.

4.3.3 Investigation of the Nanocrystal Size

Barium chloride nanocrystals grow in a fluorochlorozirconate glass matrix upon heat treatment. From our observations over a number of annealed samples under different conditions, the crystal size depends on the annealing conditions.

Figure 4.16 compares photoluminescence peaks corresponding to the $^5D_0 \rightarrow ^7F_0$ transition in three samples with different annealing histories and that in a Sm^{2+} doped single $BaCl_2$ crystal. The spectra were recorded at 100 K. The annealing conditions are as follows: (a) 238 °C - 5 min; (b) 225 °C - 16 hours and 280 °C - 5 min; and (c) 225 °C - 16 hours and 270 °C - 20 min. Data for the single crystal $BaCl_2:Sm^{2+}$ were extracted from the work by Lauer and Fong [53].

It can be seen that the spectral widths for our glass-ceramics are much broader than that for the single crystal. Those spectral broadenings of emissions from glass-ceramics should be due to the random variation of the crystal fields in the vicinity of the activator ions embedded in the host matrix. This inhomogeneous broadening is typically caused by lattice distortions seen close to the surface, which are minimum inside a $BaCl_2$ crystal but stronger closer to the surface. Moreover, this effect is even stronger in smaller nanocrystals, which has a higher surface-to-volume ratio. X-ray diffraction investigations have shown that the average size of those nanocrystals in Figure 4.16 are 9 nm, 46 nm, and 170 nm for samples (a), (b), and (c), respectively.

At temperatures higher than $\sim$ 100 K, the $^5D_0 \rightarrow ^7F_0$ transition peak is observed in a sample containing $BaCl_2$ nanocrystals of any of the structural phases. Our observations over more than 30 samples with different concentrations of reducing agent and with different annealing histories showed that the peak was seen at practically the same position (686.4±0.3 nm). Also, the atomic vibration, which may cause additional spectral broadening, is small [53] at 100 K. We have, therefore, chosen the $^5D_0 \rightarrow ^7F_0$ transition peak to investigate the dependence of spectral broadening

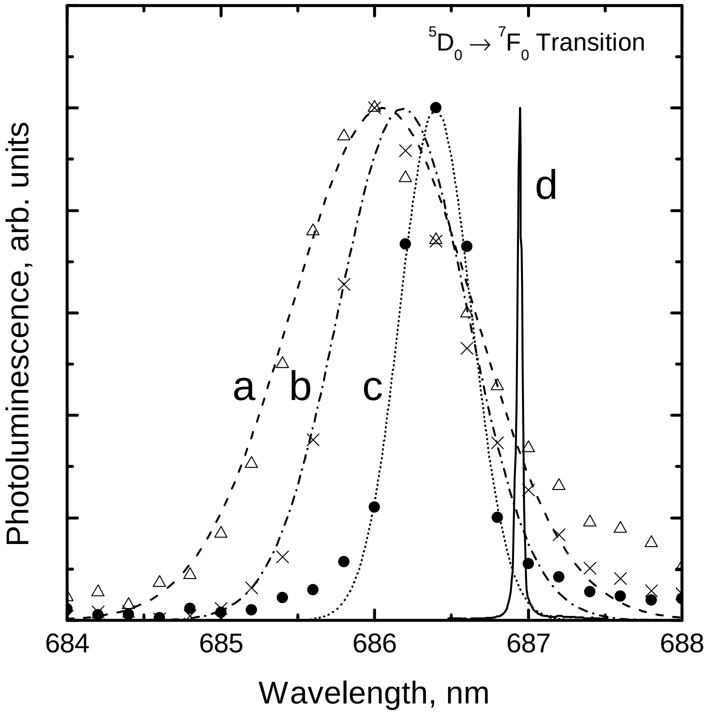

Figure 4.16: Photoluminescence spectra corresponding to the $^5D_1 \rightarrow ^7F_1$ transition for three FCZ:Sm^{2+} glass-ceramic samples with different $BaCl_2$ nanocrystal sizes: (a) 9 nm, (b) 46 nm, and (c) 170 nm , and (d) for the single crystal $BaCl_2$:Sm^{2+} , which was extracted from the work by Lauer and Fong [53]. The spectra were recorded at 100 K. The curves represent Gausssian fits to the data as explained in the text. (See also [67].)

on the nanocrystal size.

The photoluminescence peak corresponding to the $^5D_0 \rightarrow ^7F_0$ transition has been approximated by a Gaussian:

$$\Phi(\lambda) \propto \exp\left[-\left(\frac{\lambda-\lambda_o}{\Delta}\right)^2\right] \tag{4.4}$$

where λ is the wavelength, λ_o is wavelength of the peak centre, and Δ is spectral dispersion of the peak.

Figure 4.17 shows the dependence of the average nanocrystal size $< L >$ on the spectral width Δ. The nanocrystal size was obtained from XRD data using the

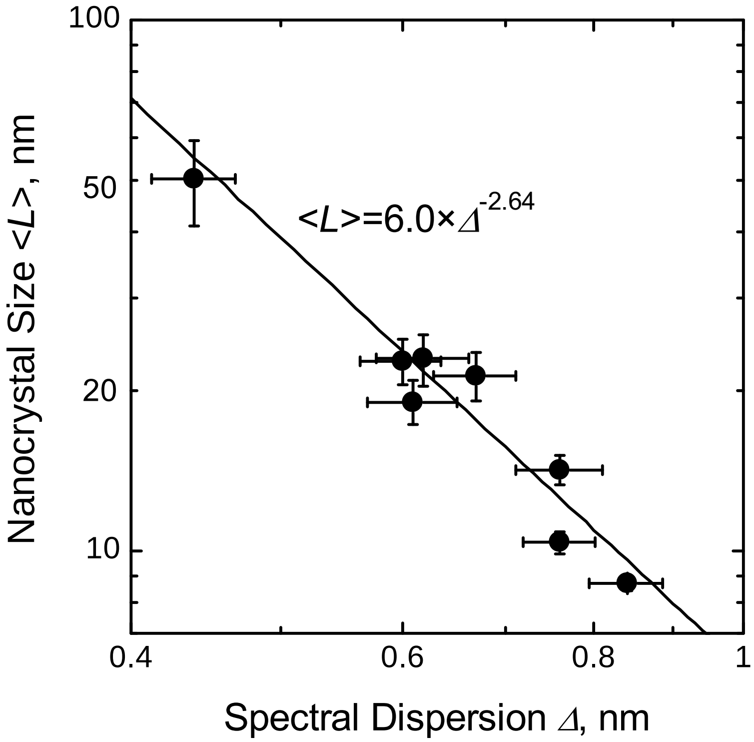

Figure 4.17: A correlation between the spectral broadening of the ${}^5D_0 \rightarrow {}^7F_0$ singlet (Δ) measured at 100 K and the average size of the $BaCl_2$ crystallites $< L >$, which was derived from XRD data. The singlet line was approximated by a Gaussian in accordance with Equation 4.4 and Δ was used as a measure of the spectral broadening of the line. The straight line is the least squares fit to the experimental data (log-log plot).

Sherrer formula (Equation 4.2) over a number of samples. The plots have unveiled a linear correlation on a log-log plot, which is fitted as:

$$< L >= 6.0 \times \Delta^{-2.64}. \tag{4.5}$$

It is instructive to mention that the data had been taken from a subset of our samples in which both XRD and PL experiments had been carried out. Equation 4.5 may be used as a convenient indicator of a nanocrystal size embedded in a glass matrix.

Figure 4.18 shows the observed correlation between nanocrystal sizes and concentrations of added reducing agent for our samples. The data were taken from those with different reducing agent concentrations (0.05 ∼ 1.0 %) annealed under

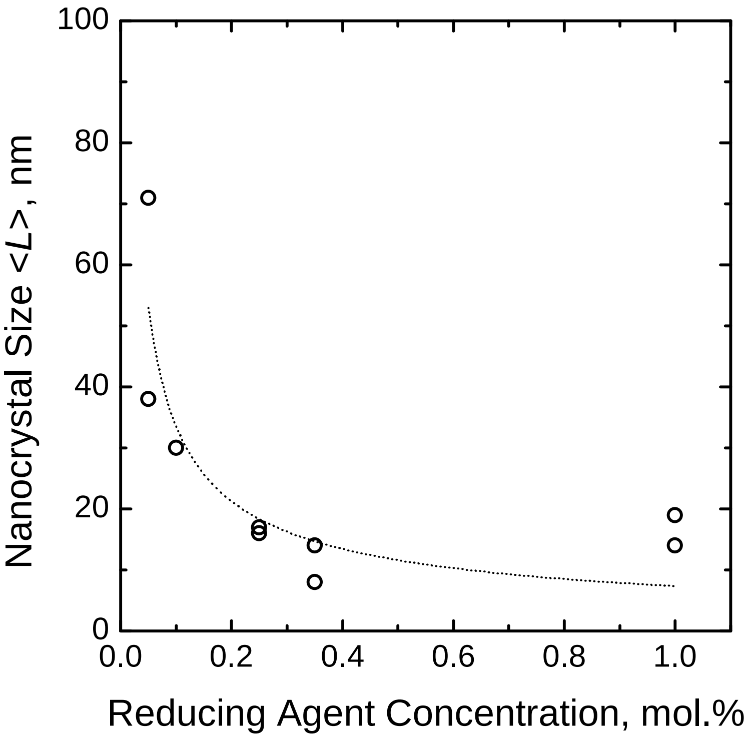

Figure 4.18: A correlation between the nanocrystal size and the fraction of added reducing agent. The samples were heat treated under the same conditions (270 °C, 30 min, H_2 + Ar). The crystal sizes were estimated using Equation 4.5.

the same conditions: 270 °C for 30 min in a mixture of hydrogen and argon gases. The average crystal size was calculated using Equation 4.5 which takes account of the spectral broadening in the photoluminescence.

As seen in Figure 4.18, although all the samples had been annealed under the same conditions, the size of nanocrystals tends to decrease as the concentration of reducing agent increases. As seen in as-prepared glasses (see Figure 4.1), more disruptions of the host matrix can be visually observed as more reducing agent is added. This fact suggests that it be possible for the disruptions to prevent the growth of $BaCl_2$ crystallites.

4.3.4 Occupation of Sm^{2+} Ions in $BaCl_2$

Sm^{2+} ions may substitute into barium sites of $BaCl_2$ nanocrystals in a FCZ glass-ceramic. The crystal structure may be either orthorhombic or hexagonal, depending upon the heat treatment conditions. On the one hand, orthorhombic $BaCl_2$ has a single crystallographic group symmetry site for barium ions (C_s). On the other hand, there are two different symmetry sites in the hexagonal phase (C_{3h} and D_{3h}). The symmetry differences result in different crystalline fields which affect the active centres differently. As a result, different energy levels or energy level splitting would be expected at each centre. Hence, the emission spectra of samples annealed under different conditions are of interest to study the effects of the local environment.

Figure 4.19 illustrates an example of photoluminescence spectra corresponding to the $^5D_0 \rightarrow ^7F_0$ and $^5D_0 \rightarrow ^7F_1$ optical transitions in FCZ:Sm^{2+} glass-ceramics predominantly containing (a) the orthorhombic and (b) hexagonal $BaCl_2$ crystallites. The sample in (a) contains 40 nm $BaCl_2$ crystallites, while the crystallites are 12 nm for the sample in (b). It is clearly seen that both types of sample show a single peak ($\sim$ 686 nm) corresponding to the $^5D_0 \rightarrow ^7F_0$ transition as well as a triplet corresponding to the $^5D_0 \rightarrow ^7F_1$ transition.

In samples containing predominantly the orthorhombic $BaCl_2$ nanocrystals, the peak positions of the triplet appeared to be consistent and centered at 698.1±0.2, 700.3±0.2, and 703.0±0.1 nm. The averaging was done over 10 samples annealed under different conditions. Also, the relative intensities of the peaks are in a good agreement to those found in the orthorhombic $BaCl_2$ single crystal [53]. The samples containing predominantly the hexagonal phase also show consistent peak positions for the triplet centering at 698.1±0.3, 700.3±0.2, and 703.7±0.6 nm in Figure 4.19. The averaging was done over 20 samples. However, unlike the orthorhombic phase, the relative intensities vary dramatically. Also, it seems as though the position of the right-most peak in the figure has shifted to 704 nm with respect to that in the

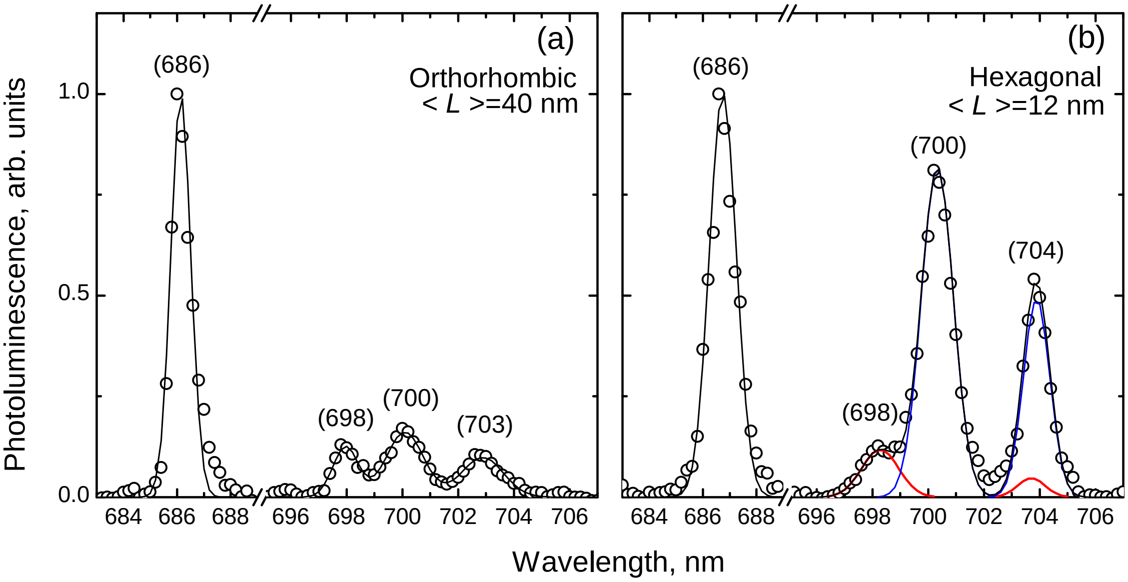

Figure 4.19: Photoluminescence spectra corresponding to the $^5D_0 \rightarrow ^7F_0$ and $^5D_0 \rightarrow ^7F_1$ optical transitions in FCZ:Sm^{2+} glass-ceramics containing predominantly (a) the orthorhombic and (b) the hexagonal BaCl$_2$ crystallites.

orthorhombic phase.

Relative intensities of photoluminescence peaks corresponding to the $^5D_0 \rightarrow ^7F_0$ and $^5D_0 \rightarrow ^7F_1$ transitions have been investigated for samples that were heat treated under different conditions. Figure 4.20 shows the peak ratios by samples containing predominantly (a) the orthorhombic and (b) hexagonal phases. The three-digit numbers in the figure indicate the peaks in terms of their rounded position in nm. In samples containing predominantly the orthorhombic phase, the relative intensities corresponding to the $^5D_0 \rightarrow ^7F_0$ and $^5D_0 \rightarrow ^7F_1$ transitions do not depend on the crystallite size. This explains that all of the Sm^{2+} ions in the nanocrystals experience the same crystal field since there is only a single group symmetry site (C$_s$) for Sm^{2+} in the orthorhombic BaCl$_2$.

In comparison to the samples containing predominantly the orthorhombic BaCl$_2$ nanocrystals, the relative intensities of the $^5D_0 \rightarrow ^7F_0$ and $^5D_0 \rightarrow ^7F_1$ peaks vary from

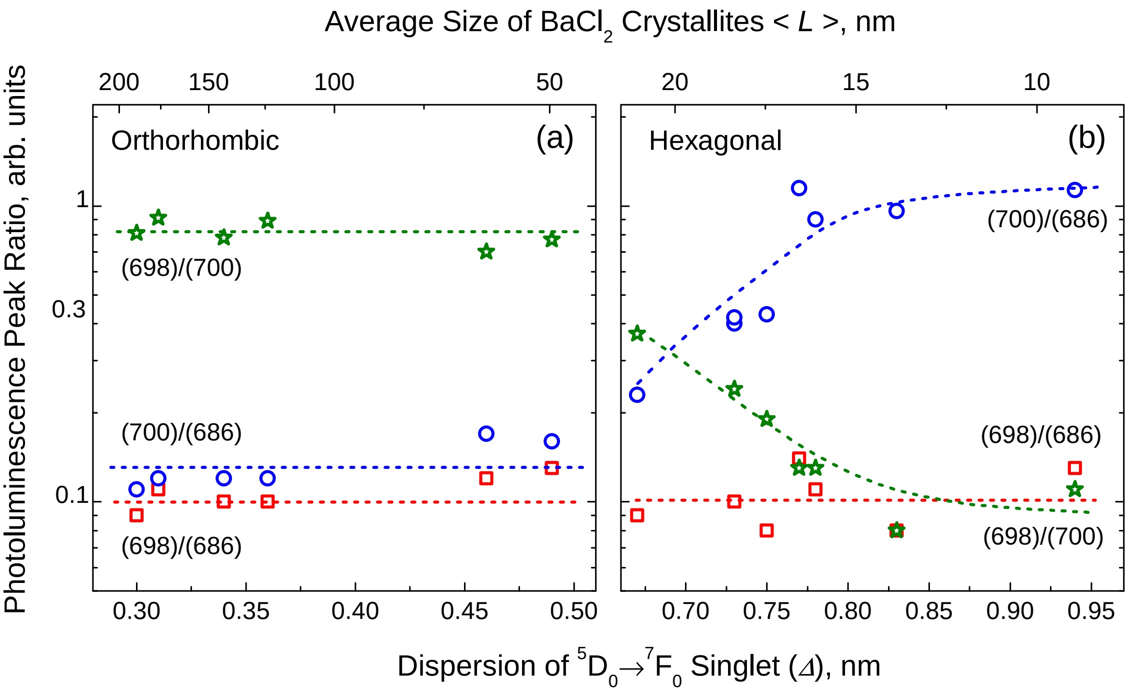

Figure 4.20: Peak ratios of photoluminescence intensities corresponding to the $^5D_0 \rightarrow {}^7F_0$ and $^5D_0 \rightarrow {}^7F_1$ optical transitions in FCZ:Sm^{2+} glass-ceramics as a function of the spectral dispersion of the $^5D_0 \rightarrow {}^7F_0$ peak. (a) corresponds to samples containing predominantly the orthorhombic BaCl$_2$ crystallites and (b) corresponds to that of hexagonal.

sample to sample for those containing the hexagonal phase. This spectrum variation can be explained if we assume that the triplet consists of two doublets (698$^{(c)}$ and 704$^{(c)}$; 700$^{(d)}$ and 704$^{(d)}$) originating from two different luminescent centres at C$_{3h}$ and D$_{3h}$, respectively. This assumption is supported by the following two facts:

1. Sm^{2+} ions may occupy the two different crystallographic sites in hexagonal BaCl$_2$ crystallites.

2. Our observations over a number of samples shows that contributions to the 704-nm peak from the Sm^{2+} ions at the two different optical centres remain constant, A(704$^{(c)}$)/A(698$^{(c)}$) = 0.4 and A(704$^{(d)}$)/A(700$^{(d)}$) = 0.6. This fact suggests that the triplet is actually two doublets whose right most peaks overlap at ∼ 704 nm, and they originate from two different crystallographic centres.

Further analysis would identify the origin of the two different doublets with the group symmetry sites in the hexagonal $BaCl_2$ nanocrystals. As seen in Figure 4.20, the peak intensity ratio between those at 686 nm and 698 nm ((698)/(686)) remains practically constant over a number of samples with different annealing histories (square plots). This suggests that the origins of the ${}^5D_0 \rightarrow {}^7F_0$ singlet and the doublet ($698^{(c)}$, $704^{(c)}$) be the same luminescent centre. The group theory analysis suggests that the ${}^5D_0 \rightarrow {}^7F_1$ transitions of Sm^{2+}, which was observed to be a doublet, is allowed for both the C_{3h} and D_{3h} sites; however, the singlet ${}^5D_0 \rightarrow {}^7F_1$ transition is only allowed at the C_{3h} site. For these reasons, we attribute the singlet at 686 nm and the doublet at 698 and 704 nm to the luminescence by samarium ions at the C_{3h} sites in the hexagonal $BaCl_2$ nanocrystals. In addition, we attribute the doublet at 700 nm and 704 nm to that at the D_{3h} sites.

There is a correlation of peak intensities with respect to the Δ, or the average nanocrystal size $< L >$. When $< L >$ is small, the doublet ($700^{(d)}$, $704^{(d)}$) is strong, while the doublet ($698^{(d)}$, $704^{(d)}$) is practically absent. However, as the nanocrystals grow larger, relative intensities of the doublet ($700^{(d)}$, $704^{(d)}$) decreases and that of the other doublet ($698^{(c)}$, $704^{(c)}$) increases. This fact suggests that Sm ions prefer to occupy the C_{3h} site in small-size hexagonal $BaCl_2$ crystals, while D_{3h} site becomes more likely occupied as the nanocrystals grow.

4.4 X-ray Luminescence

Divalent samarium doped fluorochlorozirconate (FCZ:Sm^{2+}) glass-ceramics have been produced for X-ray scintillator applications. It is, therefore, of primary importance to investigate X-ray induced luminescence (XL) of our samples. Earlier in this work we have shown that divalent samarium ions can be activated upon heat treatment and the only ions embedded in the resulting $BaCl_2$ nanocrystals showed efficient fluorescence (see Section 4.2.5). This section will discuss X-ray induced luminescence in terms of heat treatment conditions and the resulting nanocrystals.

As-prepared glass samples with different fractions of added reducing agent (005, 0.1, 0.25, 0.35, and 1 molar %) were annealed in either a nitrogen or a mixture of 5 % hydrogen and 95 % argon gas with a fixed temperature and time (270 °C for 30 min). X-ray luminescence spectra of the resulting glass-ceramics were recorded at room temperature and were integrated over the 200 − 1000 nm range. The integrated intensities of the samples were normalized to the thicknesses of samples and were plotted as a function of the quantity of reducing agent added in Figure 4.21. The squared plots correspond to annealing in a nitrogen atmosphere, while the circle plots represent samples annealed in a hydrogen + argon gas.

As seen in the graph, the annealed samples in a hydrogen containing atmosphere tend to show higher XL intensities than those annealed in nitrogen. One may argue that it is due to Sm^{3+} to Sm^{2+} reduction by the hydrogen gas. Another argument is that hydrogen atoms may stimulate the reconstruction of the host matrix surrounding $BaCl_2$ nanocrystals and thus may facilitate the transport of excess electrons and holes created by X-ray excitation towards luminescence centres. A similar effect in a ZBLAN glass was observed by Hasz et al. [73]. Further studies should be done in future work.

For both the annealing atmospheres, the graphs show the fluorescence intensities

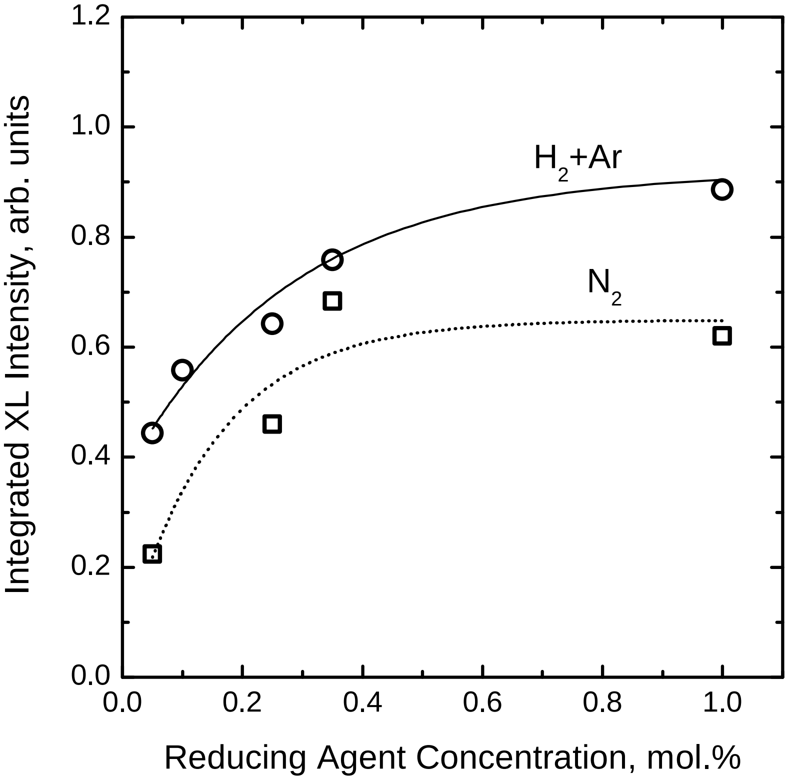

Figure 4.21: Thickness-normalized integrated X-ray fluorescent intensities versus concentration of reducing agent added. The samples were heat treated in either a nitrogen or a mixture gas of 5 % hydrogen and 95 % argon at 270°C for 30 min.

become stronger as the amount of reducing agent added increases until it saturates around 0.35 % of reducing agent concentration. This correlation is in good agreement with that of the reduced Sm^{3+} ion concentration (see Figure 4.4). The reduction process saturates around 0.35 % and higher. Therefore, this common correlation clearly explains the strong dependence of XL intensity on the amount of reduced divalent samarium ions. However, at the present time only a small fraction of Sm^{3+} was succesfully reduced to the divalent state. Thus, we expect much stronger X-ray scintillation from FCZ:Sm^{2+} glass-ceramics if we could successfully achieve efficient valency conversion.

It is well known that non-radiative transition (energy transition without an emis-

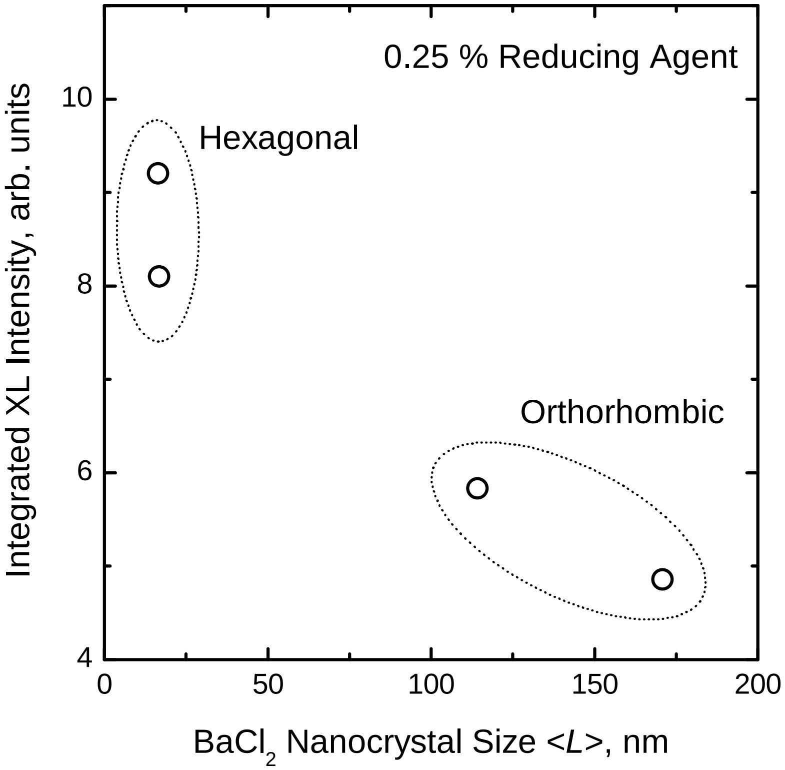

Figure 4.22: Integrated X-ray induced luminescence intensities versus the nanocrystal sizes embedded in the FCZ glass matrix. The samples contain 0.25 % of reducing agent.

sion of radiation) is efficient near the crystal surface. Since for a small crystallite the surface-to-volume ratio is large, weaker luminescence is expected than that of larger crystallite containing samples in general. FCZ glass-ceramic samples containing different sizes of $BaCl_2$ nanocrystals have been prepared by annealing under different conditions. Figure 4.22 illustrates integrated XL intensity as a function of the nanocrystal size. To our surprise, samples with smaller nanocrystals had stronger fluorescence. Further investigations unveiled that the two samples which showed stronger emission contain predominantly the hexagonal phase, while the orthorhombic $BaCl_2$ were predominately contained in the other two samples as indicated in the figure. This conflict would be explained by taking into account the down shift of the $4f^5 5d^1$ level, which was discussed in Section 4.3.1. This lowered 4f5d level would be more likely to be populated, thus the 5d-4f transitions would become more preferable. Moreover, photoluminescence investigation revealed that the optical transition of divalent samarium ion in the hexagonal $BaCl_2$ is dominated by a strong and broad band, which is due to the allowed 5d-4f transitions, rather than sharp peaks by the 4f-4f transitions.

Consequently, in order to obtain a strong X-ray induced luminescence, samples should be annealed in a hydrogen containing atmosphere, eg. H_2 + Ar, as well as the annealing condition should be such that $BaCl_2$ nanocrystals grow in the hexagonal crystal structure. Moreover, dramatic improvement of the fluorescence intensity would be expected to be achieved by improving the valency conversion efficiency.

Chapter 5

Summary and Conclusions

The objective of this project was the preparation and characterization of divalent samarium doped fluorochlorozirconate (FCZ:Sm^{2+}) glass-ceramics for high-resolution X-ray imaging scintillator applications. In order to obtain a high-resolution X-ray image, the scintillator matrix has to be transparent to the X-ray induced light emission (X-ray luminescence, XL) to avoid light scattering as it travels towards the surface. The FCZ as a host glass was expected to be a good choice for its well-known excellent transparency. In addition, it is strongly preferred for the scintillator to give an XL in the red region of the spectrum, in which today's Si-based imaging sensors are sensitive. Many materials containing Sm^{2+} ions as a photoactivator have shown a strong red emission. Moreover, the well-known sharp optical emission spectrum of Sm^{2+} corresponding to the 4f-4f transitions would be a useful probe for the local environment of this ion.

Doping FCZ glasses with Sm^{2+} is not so straightforward because SmF_2 or $SmCl_2$ is not commercially available. Therefore, we have attempted to convert Sm^{3+} in FCZ:1%Sm^{3+} glasses to the divalent state by adding a few molar fractions of a common reducing agent ($NaBH_4$) into the melt. The obtained glass samples showed an excellent transparency in the optical range of interest (> 600 nm). Moreover, absorption coefficients of the samples suggested the existance of samarium ions in the divalent state in the glass matrix. We have, therefore, developed a method to dope an FCZ glass with Sm^{2+} that involves the addition of a reducing agent into the melt. However, the estimated concentration at most was only 0.3 %, and the conversion process was effective up to approximately 0.35 % of reducing agent added.

Meanwhile, a reduction of Zr^{4+} to the lower valence state, seen as black spots, were found in the glasses. This may cause a loss of image quality if these samples were to be used for X-ray imaging applications.

In order to obtain glass-ceramics, the as-prepared glass samples were further annealed. Powder X-ray diffraction (XRD) studies have been carried out on the samples with different annealing histories in terms of the annealing temperature, time, and atmosphere. The XRD studies confirmed the existence of $BaCl_2$ nanocrystals in the glass matrix. Further data analyses have unveiled that the crystal structure and average crystal size depend upon the annealing conditions. The crystal structure was either the orthorhombic or hexagonal, while the average crystal size varied from 8 nm to 170 nm. It is instructive to mention here that $BaCl_2$ is highly hygroscopic; however, it was easily encapsulated by the FCZ glass matrix upon heat treatment.

As-prepared glass samples showed a broad optical absorption band by Sm^{2+} ions. Upon heat treatment, the resulting glass-ceramic samples showed additional sharp peaks from the Sm^{2+} ions, which are in a good agreement with the spectrum obtained from a $BaCl_2$:Sm^{2+} single crystal reported by Lauer and Fong [53]. This explains that the converted Sm^{2+} ions were embedded in the $BaCl_2$ nanocrystals as they grew.

When as-prepared samples were irradiated by UV light and X-rays at room temperature, only very weak luminescence from Sm^{3+} ions was observed. Further, we could not detect any XL nor PL from Sm^{2+} ions even though their presence was confirmed by optical absorption. However, annealed samples showed strong red light emissions mainly from Sm^{2+} ions, and the intensity was much higher ($\sim$ 8 times higher in the case of XL) than that of as-prepared samples. In addition, appropriately annealed glass-ceramic samples showed equivalent transparency to that of as-prepared glass samples. These results suggest that our glass-ceramics have considerable potential for scintillator applications in high-resolution X-ray imaging.

Photoluminescence (PL) spectra as a function of temperature were recorded for a number of glass-ceramic samples heat treated under different conditions: temperature, time, and atmosphere. The analysis unveiled a very strong dependence of the 4f-4f optical transitions of Sm^{2+} ions in $BaCl_2$ on the temperature when the crystal structure is the orthorhombic phase. Approximately above 100 K, the $^5D_0 \rightarrow ^7F_J$ (J = 0, 1, 2, ...) transitions are dominant, while the $^5D_1 \rightarrow ^7F_J$ (J = 1, 2, 3, ...) transitions were mainly observed below 100 K down to 12 K. In contrast, samples with the hexagonal $BaCl_2$ nanocrystals showed only the $^5D_0 \rightarrow ^7F_J$ transitions over the entire temperature range of measurement (12 – 200 K). The latter was comfortably explained under the assumption that the bottom of the $4f^5 5d^1$ level down shifted to lie below the $^5D_1$ level to act as a channel to feed the lower $^5D_0$ level even at low temperatures.

When samples contain both the orthorhombic and hexagonal $BaCl_2$ nanocrystals, we observed the simultaneous presence of the above two characteristics. At low temperatures (e.g. 12 K), relative strengths of the transitions $^5D_0 \rightarrow ^7F_J$ and $^5D_1 \rightarrow ^7F_J$ differ sample to sample. Based on this fact, we have established a 'figure of merit' to identify the relative concentration of the two phases by simply comparing peak intensities of the $^5D_1 \rightarrow ^7F_1$ and $^5D_0 \rightarrow ^7F_0$ transitions, which represent concentrations of the orthorhombic and hexagonal $BaCl_2$ nanocrystals, respectively (though the oscillator strengths must be taken into account for more accurate calculations, which are unknown at present).

A spectral broadening of a sharp PL peak corresponding to the $^5D_0 \rightarrow ^7F_0$ transition recorded at 100 K can be used to estimate the average size of nanocrystals embedded in the glass matrix. Both the PL at 100 K and XRD at room temperature were carried out for a number of samples with different annealing histories. By comparing the PL spectral widths corresponding to $^5D_0 \rightarrow ^7F_0$ (by assuming the peaks have a Gaussian shape) and the estimated nanocrystal sizes by the XRD technique, we have established a useful correlation to estimate the nanocrystal size.

The singlet peak corresponding to the $^5D_0 \rightarrow ^7F_0$ transition and three-line split manifold of the $^5D_0 \rightarrow ^7F_1$ transition peaks were extensively studied together for a number of glass-ceramic samples heat treated under different conditions. While all the samples containing the orthorhombic $BaCl_2$ nanocrystals showed consistent relative peak ratios, the relative peak ratios vary sample to sample for those containing the hexagonal $BaCl_2$ nanocrystals. Further analysis unveiled that the triplet consists of two partially overlapped doublets. Moreover, the singlet peak and one of the doublets at 698 nm and 704 nm originate from the Sm^{2+} ion embedded at a C_{3h} site of the hexagonal $BaCl_2$ nanocrystal; meanwhile, the other doublet at 700 nm and 704 nm are from the Sm^{2+} ion at a D_{3h} site. In addition, upon nucleation of the $BaCl_2$ nanocrystals, the Sm^{2+} ions were more likely to populate the D_{3h} sites; whereas, as the crystals grow, the C_{3h} sites become more populated.

X-ray induced luminescence (XL) was carried out on our FCZ:Sm^{2+} glass-ceramic samples and suggested three interesting conclusions. First, the glass-ceramic samples were annealed under the same temperature and time but different atmospheres (H_2 + Ar and N_2); as a result, the samples annealed in a H_2 + Ar gas showed higher XL intensities (integrated over the 200 – 1000 nm range) compared to that annealed in a N_2 gas. Second, XL intensities from glass-ceramic samples as a function of the fraction of added reducing agent showed a good correlation with that of the Sm^{2+} ion concentrations, in which the saturation was observed when the reducing agent concentration was higher than 0.35 %. This fact explains that the XL intensity is strongly dependent on the concentration of Sm^{2+} ions embedded in the sample. Since our current samples contain only a few percentage of Sm^{3+} ions were reduced to Sm^{2+} (0.003 %), it suggests that a more efficient valency conversion, or a higher concentration of Sm^{2+} ions will enable us to obtain a much more efficient FCZ:Sm^{2+} scintillator. Third, samples containing the hexagonal $BaCl_2$ nanocrystals showed higer intensities than those with the orthorhombic $BaCl_2$ despite the fact that the former had smaller nanocrystal size than that for the latter — non-radiative transitions are expected to be higher in smaller crystals. This conflict could be explained with the assumption, which was made from the photoluminescence characterization, that the lowest 4f5d level of Sm^{2+} ions embedded in the hexagonal $BaCl_2$ nanocrystals down shifts with respect to that in the orthorhombic phase so the 4f5d level becomes more likely to be populated and, as a result, the allowed 5d-4f transitions, which gives a strong red emission, become more probable.

The following points are suggested as possible future experiments on the subject:

1. Annealing conditions should be optimized in order to obtain the hexagonal $BaCl_2$ nanocrystals in the glass matrix with a reasonably large size while maintaining the optical transparency; the crystal size should be less than 50 nm in diameter.
2. We should use higher concentrations of Sm^{2+} ions in FCZ:Sm^{2+} glass-ceramics for more efficient scintillators.
3. A quantitative measurement of an X-ray image quality such as the modulation transfer function should be evaluated with our FCZ:Sm^{2+} glass-ceramic scintillator screen.

REFERENCES

[1] J. A. Rowlands and J. Yorkston, “Flat panel detectors for digital radiography,” in *Handbook of Medical Imaging: Physics and Psychophysics*, J. Beutel, H. L. Kundel, and R. L. Van Metter, Eds. U.S.A: SPIE - The International Society of Optical Engineering, 2000, pp. 223–328.

[2] T. A. Delchar, *Physics in medical diagnosis.* London: Chapman & Hall, 1997.

[3] B. J. Fogal, “Electronic transport properties of stabilized amorphous selenium x-ray photoconductors,” Master’s thesis, University of Saskatchewan, 2005.

[4] A. R. Cowen, “Digital x-ray imaging,” *Measurement Science and Technology*, vol. 2, pp. 691–707, 1991.

[5] X. Cao and H. K. Huang, “Current status and future advances of digital radiography and PACS,” *IEEE Engineering in Medicine and Biology*, vol. 19, no. 5, pp. 80–88, 2000.

[6] J. Rowlands and S. Kasap, “Amorphous semiconductors usher in digital x-ray imaging.” *Physics Today*, vol. 50, no. 11, pp. 24–30, 1997.

[7] S. O. Kasap and J. A. Rowlands, “X-ray photoconductors and stabilized a-Se for direct conversion digital flat-panel x-ray image-detectors,” *Journal of Materials Science: Materials in Electronics*, vol. 11, no. 3, pp. 179–198, 2000.

[8] ——, “Direct-conversion flat-panel x-ray image sensors for digital radiography,” *Proceedings of the IEEE*, vol. 90, no. 4, pp. 591–604, 2002.

[9] G. S. Belev, “Electrical properties of amorphous selenium based photoconductive devices for application in x-ray image detectors,” Ph.D. dissertation, University of Saskatchewan, 2007.

[10] N. Kotera, S. Eguchi, J. Miyahara, S. Matsumoto, and H. Kato, “Method and apparatus for recording and reproducing a radiation image,” U.S. Patent 4 236 078, 1980.

[11] M. Sonoda, M. Takano, J. Miyahara, and H. Kato, “Computed radiography utilizing scanning laser stimulated luminescence,” *Radiology*, vol. 148, no. 3, pp. 833–838, 1983.

[12] J. A. Rowlands, “The physics of computed radiography,” *Physics in Medicine and Biology*, vol. 47, no. 23, pp. R123–R166, 2002.

[13] H. von Seggern, "Photostimulable x-ray storage phosphors: a review of present understanding," *Brazilian Journal of Physics*, vol. 29, no. 2, pp. 254–268, 1999.

[14] A. R. Lakshmanan, "Radiation induced defects and photostimulated luminescence process in BaFBr:Eu^{2+}," *Physica Status Solidi (a)*, vol. 153, pp. 3–27, 1996.

[15] "Production of the mammogram," *Journal of the International Comission on Radiation Units and Measurements*, vol. 9, no. 2, pp. 15–20, 2009.

[16] K. A. Fetterly and N. J. Hangiandreou, "Image quality evaluation of a desktop computed radiography system," *Medical Physics*, vol. 27, pp. 2669–2679, 2000.

[17] M. J. Yaffe and J. A. Rowlands, "X-ray detectors for digital radiography," *Physics in Medicine and Biology*, vol. 42, pp. 1–39, 1997.

[18] H. Li, E. Epelbaum, M. Batentschuk, and A. Winnacker, "Tape casting of storage phosphor BaFBr:Eu^{2+} for x-ray imaging," *Materials Science and Engineering B*, vol. 96, no. 3, pp. 313–319, 2002.

[19] S. Tao, K. S. Karim, P. Servati, C. H. Lee, and A. Nathan, "Large area digital x-ray imaging," *Sensor Update*, vol. 12, no. 1, pp. 3–49, 2003.

[20] M. Overdick, "Detectors for x-ray imaging and computed tomography," in *Advance in Healthcare Technology - Shaping the Future of Medical Care*, G. Spekowius and T. Wendler, Eds. The Netherlands: Springer, 2006, pp. 49–64.

[21] H. Kato, "Photostimulable phosphor radiography design considerations," in *Specification, Acceptance Testing and Quality Control of Diagnostic X-ray Imaging Systems (AAPM Monograph no 20)*, J. A. Seibert, G. T. Barnes, and R. G. Gould, Eds. Woodbury: AIP, 1994, pp. 731–770.

[22] I. Fujieda, G. Cho, J. Drewery, T. Gee, T. Jing, S. N. Kaplan, V. Perez-Mendez, D. Wildermuth, and R. A. Street, "X-ray and charged particle detection with CsI(Tl) layer coupled to a-Si:H photodiode layers," *IEEE Transactions on Nuclear Science*, vol. 38, no. 2, pp. 255–262, 1991.

[23] A. Edgar, "Optical properties of glasses," in *Optical Properties of Condensed Matter and Applications*, J. Singh, Ed. England: John Wiley & Sons Ltd, 2006.

[24] N. M. Winch, "Light scattering in glass ceramic x-ray imaging plates," Master's thesis, Victoria University of Wellington, 2008.

[25] A. Edgar, J. M. Spaeth, S. Schweizer, S. Assmann, P. J. Newman, and D. R. MacFarlane, "Photostimulated luminescence in a rare earth-doped fluorobromozirconate glass ceramic," *Applied Physics Letters*, vol. 75, no. 16, pp. 2386–2388, 1999.

[26] S. Schweizer, L. W. Hobbs, M. Secu, J.-M. Spaeth, A. Edgar, and G. V. A. Williams, “Photostimulated luminescence in Eu-doped fluorochlorozirconate glass ceramics,” *Applied Physics Letters*, vol. 83, no. 3, pp. 449–451, 2003.

[27] M. Secu, R. Kalchgruber, S. Schweizer, J.-M. Spaeth, and A. Edgar, “Photostimulated luminescence in BaX_2: Eu^2 (X= Br, Cl) x-ray storage phosphors,” *Radiation Effects and Defects in Solids*, vol. 157, no. 6, pp. 957–962, 2002.

[28] N. Iwase, H. Kano, S. Tadaki, M. Hasegawa, and N. Koshino, “Method of forming an x-ray image using photostimulable phosphor,” U.S. Patent 5,543,080, 1996.

[29] A. Edgar, M. Secu, G. V. M. Willams, S. Schweizer, and J. M. Spaeth, “Structural phase changes in barium bromide nano-crystals in a fluorobromozirconate glass-ceramic x-ray storage phosphor,” *Journal of Physics: Condensed Matter*, vol. 13, no. 28, pp. 6259–6269, 2001.

[30] B. Ahrens, J. Selling, C. Eisenschmidt, A. Engel, and S. Schweizer, “Sm-activated barium halide nanocrystals in fluorozirconate glasses,” *Journal of Physics: Condensed Matter*, vol. 20, no. 29, p. 295227, 2008.

[31] B. Ahrens, C. Eisenschmidt, J. A. Johnson, P. T. Miclea, and S. Schweizer, “Structural and optical investigations of Nd-doped fluorozirconate-based glass ceramics for enhanced upconverted fluorescence,” *Applied Physics Letters*, vol. 92, p. 061905, 2008.

[32] M. Secu, S. Schweizer, J. M. Spaeth, A. Edgar, G. V. M. Williams, and U. Rieser, “Photostimulated luminescence from a fluorobromozirconate glass-ceramic and the effect of crystallite size and phase,” *Journal of Physics: Condensed Matter*, vol. 15, no. 7, pp. 1097–1108, 2003.

[33] A. Edgar, G. V. M. Williams, M. Secu, S. Schweizer, and J. M. Spaeth, “Optical properties of a high-efficiency glass ceramic x-ray storage phosphor,” *Radiation Measurements*, vol. 38, no. 4-6, pp. 413–416, 2004.

[34] S. Schweizer, L. W. Hobbs, M. Secu, J.-M. Spaeth, A. Edgar, G. V. M. Williams, and J. Hamlin, “Photostimulated luminescence from fluorochlorozirconate glass ceramics and the effect of crystallite size,” *Journal of Applied Physics*, vol. 97, p. 083522, 2005.

[35] G. Chen, J. Johnson, R. Weber, R. Nishikawa, S. Schweizer, P. Newman, and D. MacFarlane, “Fluorozirconate-based nanophase glass ceramics for high-resolution medical x-ray imaging,” *Journal of Non-Crystalline Solids*, vol. 352, no. 6-7, pp. 610–614, 2006.

[36] A. Edgar, G. V. M. Williams, S. Schweizer, and J. M. Spaeth, “Spatial resolution of a glass-ceramic x-ray storage phosphor,” *Current applied physics*, vol. 6, no. 3, pp. 399–402, 2006.

[37] J. Touš, K. Blažek, L. Pina, and B. Sopko, "High-resolution x-ray imaging CCD camera based on a thin scintillator screen," *Radiation Measurements*, vol. 42, no. 4-5, pp. 925–928, 2007.

[38] V. V. Nagarkar, S. T. Tipnis, S. R. Miller, A. Lempicki, C. Brecher, P. Szupryczynski, and H. Lingertat, "A new x-ray scintillator for digital radiography," *IEEE Transactions on Nuclear Science*, vol. 50, no. 3, pp. 297–300, 2003.

[39] G. Chen, J. Johnson, S. Schweizer, J. Woodford, P. Newman, and D. MacFarlane, "Transparent $BaCl_2$:Eu^{2+} glass-ceramic scintillator," in *Medical Imaging 2006: Physics of Medical Imaging*, M. J. Flynn and J. Hsieh, Eds., vol. 6142. SPIE, March 2 2006, p. 61422X.

[40] P. A. Tick, "Are low-loss glass ceramic optical waveguides possible?" *Optics Letters*, vol. 23, no. 24, pp. 1904–1905, 1998.

[41] D. Tonchev, G. Belev, S. Panigrahi, C. Varoy, A. Edgar, H. von Seggern, and S. O. Kasap, "Rare-earth doped fluorochlorozirconate (FCZ) glasses and glass-ceramics: Selected thermal properties and x-ray luminescence in samarium doped FCZ," in *Nanostructured Materials for Advanced Technological Applications*, J. P. Reithmaier, P. Petkov, W. Kulisch, and C. Popov, Eds. The Netherlands: Springer, 2009.

[42] J. A. Johnson, J. K. R. Weber, A. I. Kolesnikov, and S. Schweizer, "Crystallization in heat-treated fluorochlorozirconate glasses," *Journal of Physics: Condensed Matter*, vol. 21, no. 37, p. 375103, 2009.

[43] Hamamatsu Photonics, "Photomultiplier tube (R7600U)," Accessed: March 31 2010. [Online]. Available: http://jp.hamamatsu.com/resources/products/etd/eng/html/pmt_003.html

[44] ——, "Silicon Photodiode (S1226)," Accessed: March 31 2010. [Online]. Available: http://jp.hamamatsu.com/products/sensor-ssd/pd041/pd042/pd044/S1226-5BQ/index_en.html

[45] ——, "CCD area image sensor(S9979)," Accessed: March 31 2010. [Online]. Available: http://jp.hamamatsu.com/products/sensor-ssd/pd101/pd102/pd103/S9979/index_en.html

[46] J. A. Johnson, S. Schweizer, B. Henke, G. Chen, J. Woodford, P. J. Newman, and D. R. MacFarlane, "Eu-activated fluorochlorozirconate glass-ceramic scintillators," *Journal of Applied Physics*, vol. 100, p. 034701, 2006.

[47] A. Edgar, S. Schweizer, S. Assmann, J. M. Spaeth, P. J. Newman, and D. R. MacFarlane, "Photoluminescence and crystallization in europium-doped fluorobromozirconate glass-ceramics," *Journal of Non-Crystalline Solids*, vol. 284, no. 1-3, pp. 237–242, 2001.

[48] G. Soundararajan, "Optical characterization of rare earth doped glasses," Master's thesis, University of Saskatchewan, 2009.

[49] B. Henke, B. Ahrens, P. T. Miclea, C. Eisenschmidt, J. A. Johnson, and S. Schweizer, "Erbium- and chlorine-doped fluorozirconate-based glasses for upconverted fluorescence," *Journal of Non-Crystalline Solids*, vol. 355, pp. 1916–1918, 2009.

[50] B. Henke, B. Ahrens, J. A. Johnson, P. T. Miclea, and S. Schweizer, "Upconverted fluorescence in Er-doped ZBLAN glasses for high efficiency solar cells," in *Procedings of SPIE*, L. Tsakalakos, Ed., vol. 7411, 2009, p. 74110E.

[51] A. Dybko, "Fundamentals of optoelectronics," in *Optical Chemical Sensors*, F. Baldini, A. N. Chester, J. Homola, and S. Martellucci, Eds. The Netherlands: Springer, 2006, pp. 47–58.

[52] L. Struder, G. Kanbach, N. Meidinger, F. Schopper, R. Hartmann, P. Holl, H. Soltau, R. Richter, and G. Lutz, "The development of avalanche amplifying pn CCDs: A status report," in *High Time Resolution Astrophysics*, D. Phelan, O. Ryan, and A. Shearer, Eds. The Netherlands: Springer, 2008, pp. 281–289.

[53] H. V. Lauer Jr. and F. K. Fong, "Role of the $4f^55d$ band in the radiationless $^5D_1 \rightarrow {}^5D_0$ coupling in $BaCl_2$:Sm^{2+} and $BaBr_2$:Sm^{2+}," *The Journal of Chemical Physics*, vol. 65, no. 8, pp. 3108–3117, 1976.

[54] R. W. G. Wyckoff, *Crystal structures.* New York: Interscience Publisher, 1963.

[55] T. Hayakawa and M. Nogami, "Electronic 4f-5d structure and persistent spectral hole burning of divalent Sm ions in sol-gel derived Al_2O_3-SiO_2 glasses," *Photonics Based on Wavelength Integration Manipulation IPAP Books 2*, pp. 193–198, 2005.

[56] J. Qiu, "γ-ray induced reduction of Sm^{3+} to Sm^{2+} in sodium aluminoborate glasses," *Journal of Materials Science Letters*, vol. 20, no. 8, pp. 691–693, 2001.

[57] J. Qiu, K. Miura, T. Suzuki, T. Mitsuyu, and K. Hirao, "Permanent photoreduction of Sm^{3+} to Sm^{2+} inside a sodium aluminoborate glass by an infrared femtosecond pulsed laser," *Applied Physics Letters*, vol. 74, no. 1, pp. 10–12, 1999.

[58] M. Nogami, N. Hayakawa, N. Sugoka, and Y. Abe, "Formation of Sm^{2+} Ions in sol-gel-derived glasses of the system Na_2O-Al_2O_3-SiO_2," *Journal of the American Ceramic Society*, vol. 79, no. 5, pp. 1257–1261, 1996.

[59] M. Nogami and K. Suzuki, "Fast spectral hole burning in Sm^{2+}-doped Al_2O_3–SiO_2 glasses," *Advanced Materials*, vol. 14, no. 12, pp. 923–926, 2002.

[60] D. R. MacFarlane, P. J. Newman, J. D. Cashion, and A. Edgar, "In situ generation of Eu^{2+} in glass-forming melts," *Journal of Non-Crystalline Solids*, vol. 256-257, pp. 53–58, 1999.

[61] I. D. Aggarwal and G. Lu, *Fluoride Glass Fiber Optics.* Boston: Academic Press, 1991.

[62] S. Kasap, H. Ruda, and Y. Boucher, *Cambridge illustrated handbook of optoelectronics and photonics.* Cambridge: Cambridge University Press, 2009.

[63] SIEMENS, “Simulation of x-ray spectra,” March 30 2010. [Online]. Available: https://w9.siemens.com/cms/oemproducts/Home/X-rayToolbox/spektrum/Pages/radIn.aspx

[64] J. M. Boone and A. Seibert, “An accurate method for computer-generating tungsten anode x-ray spectra from 30 to 140 kv,” *Medical Physics*, vol. 24, no. 11, pp. 1661–1670, 1997.

[65] J. M. Boone, T. R. Fewell, and R. J. Jennings, “Molybdenum, rhodium, and tungsten anode spectral models using interpolating polynomials with application to mammography,” *Medical Physics*, vol. 24, no. 12, pp. 1863–1874, 1997.

[66] J. M. Boone, “Spectral modeling and compilation of quantum fluence in radiography and mammography,” *Proceedings of the SPIE*, vol. 3336, pp. 592–601, 1998.

[67] A. Edgar, C. R. Varoy, C. Koughia, D. Tonchev, G. Belev, G. Okada, S. O. Kasap, H. von Seggern, and M. Ryan, “Optical properties of divalent samarium-doped fluorochlorozirconate glasses and glass ceramics,” *Optical Materials*, vol. 31, no. 10, pp. 1459–1466, 2009.

[68] B. Phebus, B. Getman, S. Kiley, D. Rauser, M. Plesha, and R. H. Terrill, “Preparation and analysis of Eu^{3+}- and Eu^{2+}-doped ZBLAN and ZBLALi fluorozirconate glasses,” *Solid State Ionics*, vol. 176, no. 35-36, pp. 2631–2638, 2005.

[69] E. Biémont, H. P. Garnir, U. Litzen, K. Nielsen, P. Quinet, S. Svanberg, G. M. Wahlgren, and Z. G. Zhang, “Radiative lifetime and oscillator strength determinations in Sm III,” *Astronomy and Astrophysics - Les Ulis*, vol. 399, no. 1, pp. 343–349, 2003.

[70] H. P. Klug and L. E. Alexander, *X-ray diffraction procedures for polycrystalline and amorphous materials.* New York: Wiley, 1954.

[71] Z. He, Y. S. Wang, S. Li, and X. Xu, “Dynamic studies on the time-resolved fluorescence of Sm^{2+} in $BaCl_2$,” *Journal of Luminescence*, vol. 97, no. 2, pp. 102–106, 2002.

[72] Y. Shen and K. L. Bray, “Effect of pressure and temperature on 4f-4f luminescence properties of Sm^2 ions in MFCl crystals (M= Ba, Sr, and Ca),” *Physical review B*, vol. 58, no. 18, pp. 11 944–11 958, 1998.

[73] W. C. Hasz, S. N. Crichton, and C. T. Moynihan, “Viscosity temperature dependence of ZrF_4-based melts,” *Materials Science Forum*, vol. 32-33, pp. 589–594, 1988.